

Infrared emission of young HII regions: A Herschel/Hi-GAL study[★]

R. Cesaroni¹, M. Pestalozzi², M. T. Beltrán¹, M. G. Hoare³, S. Molinari², L. Olmi^{1,4}, M. D. Smith⁵,
G. S. Stringfellow⁶, L. Testi^{7,1}, and M. A. Thompson⁸

¹ INAF, Osservatorio Astrofisico di Arcetri, Largo E. Fermi 5, I-50125 Firenze, Italy e-mail: cesa@arcetri.astro.it

² INAF, Istituto di Astrofisica e Planetologia Spaziale, Via Fosso del Cavaliere 100, I-00133, Roma, Italy e-mail: sergio.molinari@iaps.inaf.it

³ School of Physics and Astrophysics, University of Leeds, Leeds LS2 9JT, UK

⁴ University of Puerto Rico, Rio Piedras Campus, Physics Dept., Box 23343, UPR station, San Juan, Puerto Rico, USA

⁵ Centre for Astrophysics and Planetary Science, University of Kent, Canterbury CT2 7NH, UK

⁶ Center for Astrophysics and Space Astronomy, University of Colorado, UCB 389, Boulder, CO 80309, USA

⁷ European Southern Observatory, Karl-Schwarzschild-Str. 2, 85748, Garching, Germany

⁸ Centre for Astrophysics Research, University of Hertfordshire, College Lane, Hatfield, AL10 9AB, UK

Received date; accepted date

ABSTRACT

Context. Investigating the relationship between radio and infrared emission of HII regions may help shed light on the nature of the ionizing stars and the formation mechanism of early-type stars in general.

Aims. We have taken advantage of recent unbiased surveys of the Galactic plane such as Herschel/Hi-GAL and VLA/CORNISH to study a bona fide sample of young HII regions located in the Galactic longitude range 10° – 65° by comparing the mid- and far-IR continuum emission to the radio free-free emission at 5 GHz.

Methods. We have identified the Hi-GAL counterparts of 230 CORNISH HII regions and reconstructed the spectral energy distributions of 204 of these by complementing the Hi-GAL fluxes with ancillary data at longer and shorter wavelengths. Using literature data, we obtained a kinematical distance estimate for 200 HII regions with Hi-GAL counterparts and determined their luminosities by integrating the emission of the corresponding spectral energy distributions. We have also estimated the mass of the associated molecular clumps from the (sub)millimeter flux densities.

Results. Our main finding is that for $\sim 1/3$ of the HII regions the Lyman continuum luminosity appears to be greater than the value expected for a zero-age main-sequence star with the same bolometric luminosity. This result indicates that a considerable fraction of young, embedded early-type stars presents a “Lyman excess” possibly due to UV photons emitted from shocked material infalling onto the star itself and/or a circumstellar disk. Finally, by comparing the bolometric and Lyman continuum luminosities with the mass of the associated clump, we derive a star formation efficiency of 5%.

Conclusions. The results obtained suggest that accretion may still be present during the early stages of the evolution of HII regions, with important effects on the production of ionizing photons and thus on the circumstellar environment. More reliable numerical models describing the accretion process onto massive stars are required to shed light on the origin of the observed Lyman excess.

Key words. Stars: early-type – Stars: formation – HII regions

Send offprint requests to: R. Cesaroni, e-mail: cesa@arcetri.astro.it

[★] *Herschel* is an ESA space observatory with science instruments provided by European-led Principal Investigator consortia and with important participation from NASA. PACS has been developed by a consortium of institutes led by MPE (Germany) and including UVIE (Austria); KUL, CSL, IMEC (Belgium); CEA, OAMP (France); MPIA (Germany); IAPS, OAP/OAT, OAA/CAISMI, LENS, SISSA (Italy); IAC (Spain). This development has been supported by the funding agencies BMVIT (Austria), ESA-PRODEX (Belgium), CEA/CNES (France), DLR (Germany), ASI (Italy), and CICYT/MCYT (Spain). SPIRE has been developed by a consortium of institutes led by Cardiff Univ. (UK) and including Univ. Lethbridge (Canada); NAOC (China); CEA, LAM (France); IAPS, Univ. Padua (Italy); IAC (Spain); Stockholm Observatory (Sweden); Imperial College London, RAL, UCL-MSSL, UKATC, Univ. Sussex (UK); Caltech, JPL, NHSC, Univ. Colorado (USA). This development has been supported by national funding agencies: CSA (Canada); NAOC (China); CEA, CNES,

1. Introduction

High-mass stars are characterized by luminosities in excess of $\sim 10^3 L_{\odot}$ and powerful Lyman continuum emission. The latter is bound to create an ionized region around the star, which is detected through its free-free emission. Such an HII region expands and eventually disperses, although the details of this process and the corresponding time scale are still matters of debate as they also depend on the density distribution and velocity field of the dense gas enshrouding the newly born star. The early evolution of an HII region is closely related to the formation process of an OB-type star, and is hence of great interest for studies of massive star formation. As a matter of fact, HII regions are conventionally classified as hypercompact, ultracompact (UC), compact, and extended, in order of increasing size and, presumably, age. The last class is clearly associated with more evolved

CNRS (France); ASI (Italy); MCINN (Spain); Stockholm Observatory (Sweden); STFC (UK); and NASA (USA).

objects and possibly multiple OB stars, while sources belonging to the first class are very small and faint, especially below 5 GHz owing to their spectra rising with frequency. This explains why they are difficult to detect and resolve, even with sensitive radio interferometers (see Kurtz 2005 for a review on hypercompact HII regions). Consequently, much attention has been devoted to UC and compact HII regions.

One of the problems in the study of HII regions is stellar multiplicity. The ideal template of a single star ionizing a spherical HII region is inadequate to describe the real world where massive stars form in rich stellar clusters. A viable way to shed light on this issue is to compare the radio luminosity to the bolometric luminosity of these objects. The former is sensitive only to the most massive star(s), whereas all cluster members contribute to the latter. However, a problem with measuring the bolometric luminosity is that the major contribution comes from reprocessed radiation from dust emitted at far-IR wavelengths, heavily absorbed by the Earth’s atmosphere and thus impossible to observe from the ground. Moreover, the comparison between radio and far-IR emission was hindered by the dramatic difference in angular resolution between surveys conducted in the two wavelength regimes. While radio interferometers have been able to attain subarcsecond resolutions for many decades, until recently the best data available for a large number of HII regions at $\sim 100 \mu\text{m}$ were those of the IRAS mission with an angular resolution of only $\sim 2'$. As a consequence, the luminosity measurements based mostly on IRAS data were to be taken as upper limits, as unrelated objects falling in the large beam could contribute to the estimate.

This situation has now dramatically changed and pioneering studies such as that by Wood & Churchwell 1989 can be significantly improved on. On the one hand, the ESA Herschel Space Observatory (Pilbratt et al. 2010) provides us with a tool to improve the angular resolution in the far-IR by a factor of ~ 10 with respect to IRAS. On the other hand, the completion of the CORNISH survey (Hoare et al. 2012; Purcell et al. 2013) of a large portion of the Galactic plane at 5 GHz with $\sim 1''.5$ resolution has made it possible to obtain an unbiased census of UC and compact HII regions. These radio maps are perfectly complementary to the far-IR images obtained in the context of the Hi-GAL project (Molinari et al. 2010), which covers a stripe 2° wide in latitude and 360° in longitude, following the warp of the Galactic plane, at five far-IR continuum bands. We thus decided to take advantage of the Hi-GAL and CORNISH databases to perform a systematic study of the radio and IR emission of young HII regions located in the Galactic longitude range 10° – 65° .

The present article is organized as follows. In Sects. 2 and 3.1 we describe the sample of HII regions selected from the CORNISH catalogue and illustrate the method adopted to identify the corresponding Hi-GAL counterparts. In Sects. 3.2 to 3.4 source parameters such as the distance, luminosity, and mass are estimated, while in Sect. 4 we discuss the main results obtained. Finally, in Sect. 5 the conclusions are drawn.

2. The sample

Since the main scope of our study is to investigate the IR and radio properties of young massive stars, we have selected the sources classified as “ultracompact” and “compact” HII regions in the CORNISH catalogue. This a classification was obtained after visual inspection also using the Spitzer IRAC and MIPS GAL images (more details on the method are given in Purcell et al. 2013 and will not be repeated here). Since the dis-

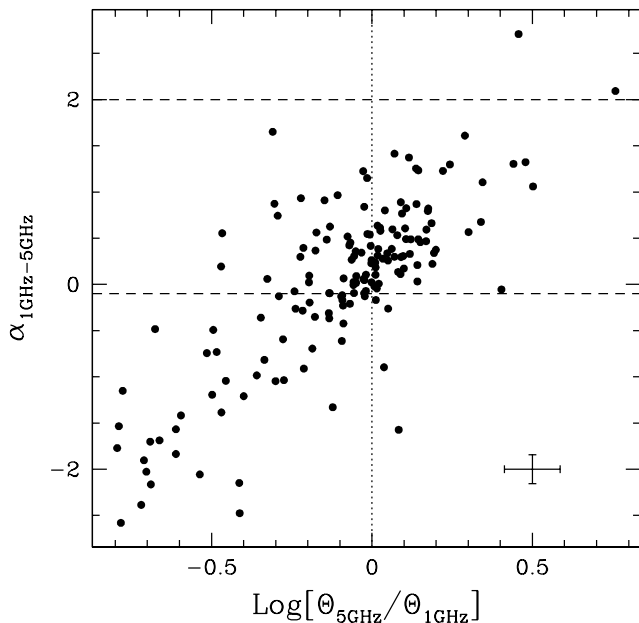


Fig. 1. Spectral index between 1.4 GHz and 5 GHz of our sample of HII regions versus the ratio between the corresponding angular sizes. The horizontal dashed lines bracket the range of spectral indices expected for free-free continuum emission, while the dotted vertical line corresponds to equal angular sizes at the two frequencies. The cross in the bottom right indicates the typical error bars assuming an uncertainty of 10% at both frequencies, for both the flux density and the size.

inction between these two types was based on the angular size and as such does not necessarily mirror an intrinsic physical and evolutionary difference, for the sake of simplicity in the following we will refer to all of our sources simply as “HII regions”.

Our sample consists of 281 bona fide HII regions. In order to further characterize them, we searched for possible counterparts at 1.4 GHz in the MAGPIS survey by White et al. (2005), whose angular resolution is $\sim 6''$. Although this resolution is ~ 4 times worse than the resolution of the CORNISH survey ($\sim 1''.5$), a comparison between the two surveys is feasible. For this purpose we selected the closest MAGPIS source within a conservative circle with $20''$ radius, taking into account that 99% of the HII regions in the CORNISH catalog have sizes below this value. We find 170 targets detected at both frequencies. In Fig. 1, we plot the spectral index (defined as $\alpha = \text{Log}(S_{5\text{GHz}}/S_{1.4\text{GHz}})/\text{Log}(5/1.4)$) as a function of the ratio between the angular diameters, Θ , at the two frequencies. Although most HII regions have a spectral index between -0.1 and $+2$, as expected for free-free emission, $\sim 1/4$ of the objects have $\alpha < -0.1$, which appears inconsistent with thermal emission. However, one sees that basically all of these points have a size ratio below unity and it is therefore very likely that the steep negative spectral index is the result of part of the flux at the highest frequency being filtered out by the interferometer. We conclude that the comparison between the 5 GHz and 1.4 GHz continuum confirms the nature of our HII region sample.

3. Analysis

3.1. IR and (sub)mm counterparts of the HII regions

Our first goal is to identify the IR counterparts of the HII regions in the Hi-GAL images at five different bands (70, 160, 250, 350, and $500 \mu\text{m}$). The angular resolution of Herschel ($\geq 9''$) does not

permit us to resolve some of the CORNISH HII regions that lie too close to each other. We thus decided to consider as distinct objects only those targets whose separation from any other target is greater than the Herschel half-power beam width (HPBW) at $160\ \mu\text{m}$ (i.e., $>11''$). The HII regions below this limit were artificially merged into a single target whose flux density is the sum of the individual flux densities and whose size is the largest of the sizes. In this way, we reduced the sample to 244 objects. For each of these, we searched for compact IR emission in the five Hi-GAL images, inside a circle of $15''$ radius, centered on the HII region itself. To identify the IR source(s) and measure their flux densities, we used the CuTex algorithm described in Molinari et al. (2011). This may result in multiple counterparts and we decided to choose the closest of these that is detected in the largest number of Hi-GAL bands. In the few cases where the emission was saturated, the flagged pixels were assigned the maximum flux of the closest pixels to the saturated region. Consequently, the corresponding luminosity is to be taken as a lower limit. However, one must keep in mind that saturation usually occurs at $250\ \mu\text{m}$ or $350\ \mu\text{m}$, while the peak of the continuum emission lies at $70\ \mu\text{m}$ (see Sect. 3.1), which implies that saturation should not affect our luminosity estimates significantly.

With the previous method we were able to identify 230 Hi-GAL counterparts out of 244 targets. In practice, in order to obtain a reliable estimate of the luminosity, from our analysis we excluded all sources that were detected in less than three Hi-GAL bands. This reduces the usable targets to 217. Finally, we rejected all counterparts whose separation from the CORNISH HII region was $>11''$ (the Herschel HPBW at $160\ \mu\text{m}$ – see above). The final number of targets with a Hi-GAL counterpart is 204. The corresponding Hi-GAL images are shown in Figs. A.2–A.5 where we split the sources into four groups depending on their Lyman continuum properties (as discussed in Sect. 4.1), and in Fig. A.6 where we show the four sources without distance estimates (see Sect. 3.2). The selection process is summarized in Table 1.

Since HII regions are known to be prominent mid-IR emitters, we also included the MSX (Price et al. 1999) $21\ \mu\text{m}$ and WISE (Wright et al. 2010) $22\ \mu\text{m}$ fluxes from the corresponding point-source catalogues, which will provide us with better sampled spectral energy distributions (SEDs) and thus more reliable luminosity estimates. We note that the MSX and WISE fluxes were obtained by summing the fluxes of all the point sources falling inside the full width at half power of the Hi-GAL $250\ \mu\text{m}$ source. We decided not to consider the MIPS GAL $24\ \mu\text{m}$ fluxes because in most of our objects these happen to be heavily saturated. For the sake of completeness, we also included the ATLASGAL¹ (Schuller et al. 2009; Contreras et al. 2013) $870\ \mu\text{m}$ and BGPS v2 (Ginsburg et al. 2013) $1.1\ \text{mm}$ fluxes. The resulting SEDs from $21\ \mu\text{m}$ to $1.1\ \text{mm}$ are shown in Fig. A.1. In Table A.1 we give the names and positions of the CORNISH HII regions, the corresponding integrated flux density at $5\ \text{GHz}$ ($S_{5\text{GHz}}$) from the CORNISH catalogue, the coordinates of the Hi-GAL counterpart, and the values of the flux densities from $21\ \mu\text{m}$ to $1.1\ \text{mm}$.

While a limited number of the SEDs may look questionable, possibly owing to faint emission and/or confusion with nearby sources, most of them appear very reasonable. In the following the SEDs will be used to obtain an estimate of both the source luminosity and mass of the associated molecular clump.

3.2. Distance estimates

A crucial parameter for our purposes is the source distance. A kinematical distance estimate can be obtained if a velocity measurement is available. Since the Hi-GAL data convey information only on the continuum emission, we investigated the literature to search for molecular or recombination line observations of the 204 usable targets. In particular, we refer to the following articles: Urquhart et al. (2013b; hereafter URQ13), Anderson et al. (2009, 2012), Beuther et al. (2002), Shirley et al. (2013), Bronfman et al. (1996), Jones et al. (2012), Kolpak et al. (2003), Pandian et al. (2008), Sewilo et al. (2004), Watson et al. (2003), Wien et al. (2012), and the RMS database² (Lumsden et al. 2013). We were able to assign an LSR velocity to all but four (G011.9786-00.0973, G026.0083+00.1369, G026.8304-00.2067, and G065.2462+00.3505) of the 204 sources.

The kinematic distance was computed for our final sample of 200 objects using the Galaxy rotation curve by Brand & Blitz (1993), which resulted in 17 cases without kinematic distance ambiguity (KDA), 172 with KDA, and 11 with velocity inconsistent with the assumed rotation curve. In the last case we assumed the distance to the tangent point. Only for source G10.62–0.38 did we replace our estimate with $4.2\ \text{kpc}$ (Urquhart, pers. comm.). To solve the KDA we searched the literature for studies where different methods were employed to discriminate the near from the far distance, and we eventually used the following references: URQ13, Anderson & Bania (2009, Anderson et al. (2012), Jones & Dickey (2012), Kolpak et al. (2003), Pandian et al. (2008), Sewilo et al. (2004), and Watson et al. (2003). In this way, we assigned the near distance to 50 targets and the far to 107, while four targets were close to the tangent point. We note that the larger number of sources at the far distance is not surprising as the area of the Galactic plane sampled by CORNISH beyond the tangent point is >3.4 times that inside the tangent point³. For the remaining 11 targets we were unable to solve the KDA and we decided to adopt the far distance. This is a conservative approach that will be justified in Sect. 4.1; in all cases, an incorrect choice for these 11 objects is bound to have negligible effects on the results obtained in the present study. The distance estimates are given in Table A.2.

3.3. Luminosity estimates

The simplest way to obtain an estimate of the luminosity of our sources is to integrate the corresponding continuum spectra by linearly interpolating between the fluxes of the SEDs in Fig. A.1. We prefer this approach to fitting a modified blackbody because the SED of HII regions is known to be made of at least two components, a relatively cold one peaking in the far-IR and a hot one peaking at shorter wavelengths. Therefore, a single fit from $21\ \mu\text{m}$ to $1.1\ \text{mm}$ is unlikely to give reliable results. More complex models such as the one developed by Robitaille et al. (2007) can provide us with satisfactory fits, but the results may significantly depend on the source geometry and orientation, which are difficult to establish. For example, the correction to the luminosity due to the flash-light effect may be important in these models, but it is unclear whether such an effect is indeed at work in our sources.

² http://rms.leeds.ac.uk/cgi-bin/public/RMS_DATABASE.cgi

³ This estimate assumes that the maximum distance at which an HII region can be detected by CORNISH is $>14\ \text{kpc}$, a reasonable assumption for optically thin HII regions associated with stars earlier than B0.5.

¹ The ATLASGAL project is a collaboration between the Max-Planck-Gesellschaft, the European Southern Observatory (ESO), and the Universidad de Chile.

Table 1. Steps of the source selection process.

CORNISH H _{II} s	H _{II} s separation <11''5	with Hi-GAL counterparts	Hi-GAL counterparts with ≥3 fluxes	CORNISH-HiGAL <11''5	with distance estimate
281	→ 244	→ 230	→ 217	→ 204	→ 200

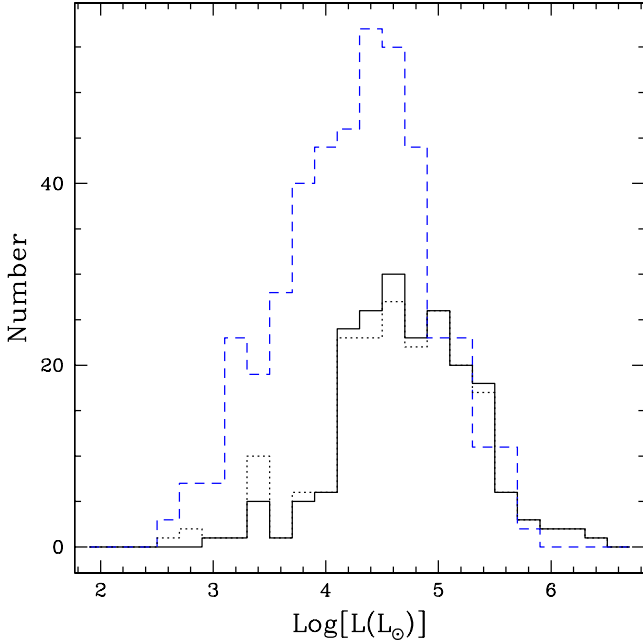


Fig. 2. Distribution of the luminosities of CORNISH HII regions. The solid and dotted histograms are obtained by choosing, respectively, the far and near distances for the 11 targets for which the KDA could not be solved. For the sake of comparison, the distribution of the HII regions from the RMS survey taken from Fig. 1 in Mottram et al. (2011) is also shown (blue dashed histogram).

We obtained the value of the luminosity (listed in Table A.2) for all of the 200 sources with a distance estimate. In Fig. 2 the distribution of these luminosities is shown. The dotted histogram shows how the distribution would change if we chose the near distance for the 11 sources for which the KDA could not be solved (our choice is the far distance, see above). Clearly the near/far ambiguity has little impact on the global sample. One can conclude that most of our objects are characterized by luminosities above $10^4 L_{\odot}$, with a handful of sources as weak as $\geq 10^3 L_{\odot}$. This finding is in good agreement with the nature of our sample consisting of stars earlier than B3. In the same figure we also plot the luminosity distribution obtained by Mottram et al. (2011; see their Fig. 1) for the RMS sample. This distribution appears to be consistent with our sources at high luminosities, while the RMS HII regions outnumber our CORNISH sample at lower luminosities. This is likely due to the CORNISH survey being less sensitive than the radio data acquired for the RMS sample, part of which has been observed at 8.6 GHz, and is thus more complete.

3.4. Mass estimates

It is also interesting to estimate the mass of the parental clump where the HII region is embedded. For this purpose, we use the flux density at $500 \mu\text{m}$ or, if this is not detected, at the longest available wavelength. In practice, the $500 \mu\text{m}$ flux was used in 92% (188 out of 204) of the cases. Following URQ13, whose

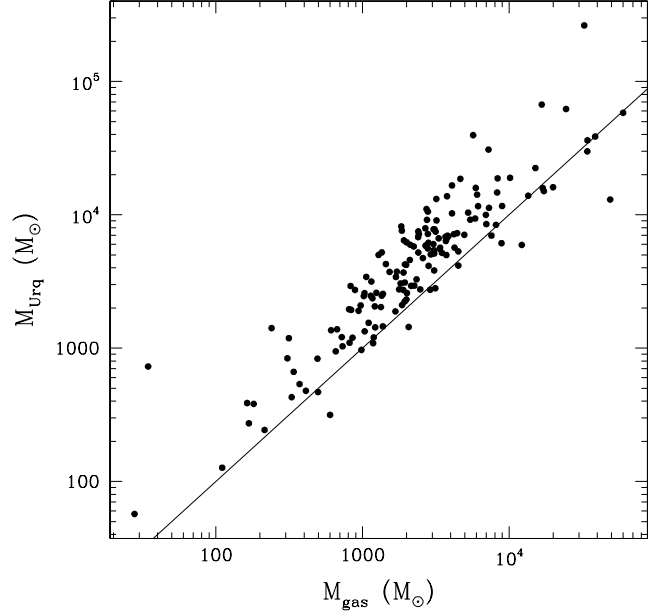


Fig. 3. Comparison between our estimate and that of URQ13 of the clump masses associated with CORNISH HII regions. The straight line corresponds to $M_{\text{Urq}} = M_{\text{gas}}$.

sample is very similar to ours, we assumed the same temperature of 20 K for all of the objects. We prefer this choice rather than deriving a temperature estimate from the SED for two reasons: we believe that the temperature obtained from the ammonia data (see URQ13) is more reliable than a value estimated from a model-dependent fit to the SED, and because the variation of temperature across the sample of URQ13 is quite limited, with most values in the range 15–30 K, which implies a maximum uncertainty of $\sim 50\%$ on our mass estimates. The dust absorption coefficient at $500 \mu\text{m}$ ($5 \text{ cm}^2 \text{ g}^{-1}$) was taken from Col. 6 of Table 1 in Ossenkopf & Henning (1994). The dust absorption coefficient was assumed to vary as $\nu^{1.9}$, obtained by fitting the values quoted in the same table. The derived masses are given in Table A.2.

Figure 3 shows a comparison between our mass estimates and those by URQ13, for the 158 sources in common between the two studies. We note that, for the sake of consistency, URQ13's masses were scaled to our distances when necessary. While the two masses appear quite consistent, the estimate of URQ13 is systematically greater (on average by a factor 1.7) than ours. This is due to the way the sub-mm flux density has been computed: in our case, the CuTex algorithm basically performs a Gaussian fit to the image, whereas URQ13 integrated the flux inside a suitable polygon. It is clear that the latter method is bound to measure more flux than the former as it also takes into account extended emission lying above the wings of the Gaussian fit. While any choice has its shortcomings, in our approach we have arbitrarily decided to consider the compact emission because we believe it to be more tightly related to the embedded HII region.

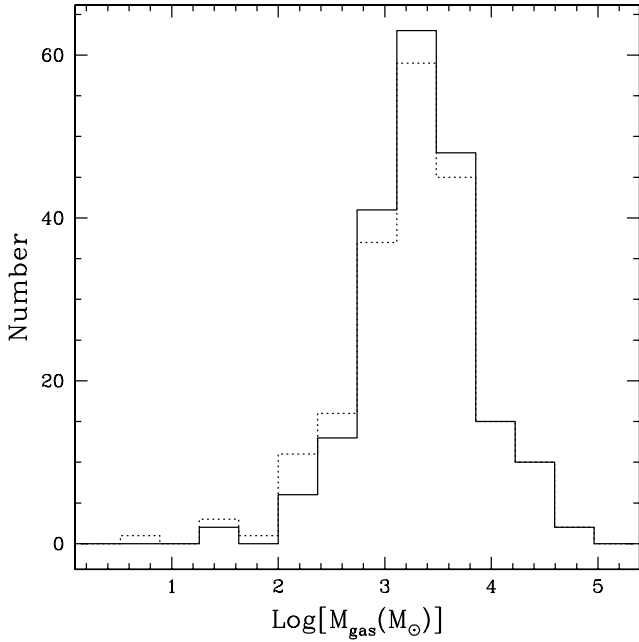


Fig. 4. Distribution of the clump mass associated with CORNISH HII regions. The solid and dotted histograms are obtained by choosing, respectively, the far and near distances for the 11 targets for which the KDA could not be solved.

The distribution of the clump masses, shown in Fig. 4, demonstrates that the vast majority of the clumps are above several $100 M_{\odot}$, as expected for high-mass star forming regions. It is thus very likely that our measurements refer to rich stellar clusters, tightly associated with the early-type stars ionizing the CORNISH HII regions.

4. Discussion

4.1. Lyman continuum excess

The large luminosities and masses of the objects under study are strongly suggestive of the presence of multiple stars. In order to establish the contribution of low-mass stars and investigate the properties of the early-type stars, we have estimated their Lyman continuum emission, N_{Ly} , assuming the free-free emission to be optically thin. We used the expression

$$N_{\text{Ly}}(\text{sec}^{-1}) = 9.9 \times 10^{43} S_{5\text{GHz}}(\text{mJy}) d^2(\text{kpc}), \quad (1)$$

where $S_{5\text{GHz}}$ is the integrated flux density at 5 GHz, d is the source distance, and the electron temperature has been taken equal to 8000 K (a mean value for Galactic HII regions; see, e.g., Quiroza et al. 2006). In Fig. 5 we compare N_{Ly} to the bolometric luminosity, L , of the 200 HII regions for which a distance estimate was possible. When considering this plot, one should keep in mind that the Lyman continuum fluxes might be underestimated for three reasons: (i) the free-free emission could be optically thick; (ii) part of the ionizing photons could be absorbed by dust inside the HII region or leaking out of it; or (iii) the radio emission could be partly resolved out by the interferometer. The last problem indeed seems to occur for a limited number of cases, as discussed in Sect. 2, while the other two are difficult to quantify. Therefore, a conservative approach is to consider the values of N_{Ly} as lower limits.

For the sake of comparison, in the figure we also plot the expected relationship between N_{Ly} and L for a single zero-age

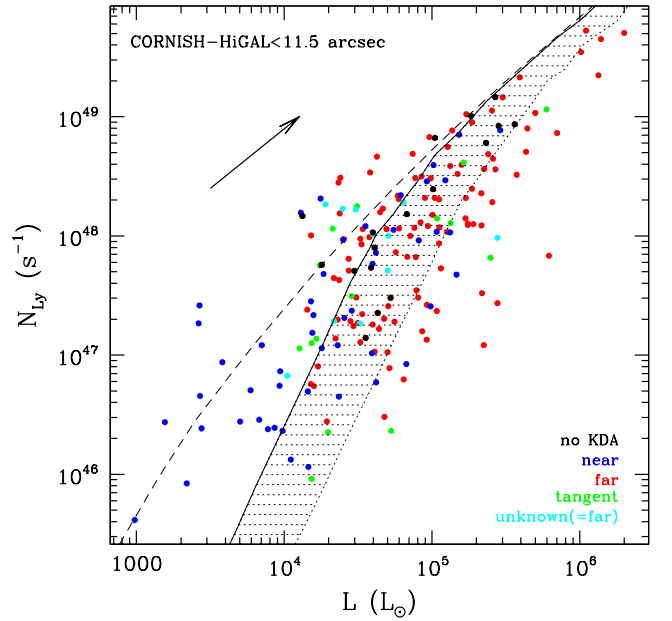


Fig. 5. Lyman continuum of the selected sample of CORNISH HII regions versus the corresponding bolometric luminosity obtained from the Hi-GAL data. The color of the symbols indicates the choice of the kinematic distance: blue for near, red for far, green for tangent point, cyan for unknown (in this case the far distance was assumed), and black for no KDA. The arrow indicates how much a point would move if its distance is increased by a factor of 2. The solid curve corresponds to the $N_{\text{Ly}}-L$ relationship for a ZAMS star, while the hatched area is where 90% of the simulated stellar clusters should lie. We note the large number of sources in the forbidden region above the solid curve. The dashed curve is the N_{Ly} that a star would emit if it were a perfect blackbody.

main-sequence (ZAMS) star (solid curve) as well as the Lyman continuum emission of a blackbody with the same radius and effective temperature as the ZAMS star (dashed curve). The properties of ZAMS stars have been obtained from Panagia (1973), Thompson (1984), Smith et al. (2002), and Martins et al. (2005). The solid curve is to be seen as an upper limit to the number of Lyman continuum photons per unit time that can be emitted by a ZAMS star of a given luminosity. As previously mentioned, it is very likely that the regions we studied are associated with stellar clusters rather than single early-type stars. In this case, the expected N_{Ly} must be less than that of a single star with the same luminosity and the hatched area in Fig. 5 is where 90% of the clusters should fall. This has been obtained by simulating a large number of clusters, up to a maximum stellar mass of $120 M_{\odot}$, adopting the IMF of Kroupa et al. (2009), as explained in Sánchez-Monge et al. (2013).

Although many sources (44.5%) lie in the cluster area, a significant fraction falls below (22%) and above it (33.5%). To some extent, a deficit in N_{Ly} is not surprising because of the various effects that may lead to its underestimation (see above). In addition, the sources that most suffer from such a deficit have been assigned the far kinematic distance; if this is replaced by the near distance, the corresponding points below the hatched region move toward the bottom left, parallel to the arrow in the figure, thus approaching the hatched area. A more physical explanation might be that the stars ionizing the HII regions are larger and cooler than on the ZAMS, possibly because of residual accretion onto the stellar surface (see Hosokawa & Omukai 2009), which implies a significant decrease of the Lyman continuum photon rate. Finally, it is also possible that we are dealing with

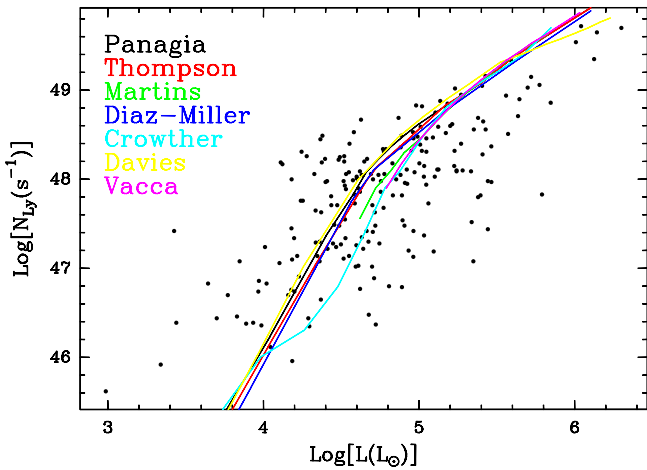


Fig. 6. Same as Fig. 5, where the relationships between N_{Ly} and L for a single ZAMS star obtained by various authors (Panagia 1973; Thompson 1984; Martins et al. 2005; Diaz-Miller et al. 1998; Davies et al. 2011; Vacca et al. 1996; Crowther 2005) are plotted. Clearly, in all cases the number of sources lying in the forbidden region above these curves is large.

clusters overabundant in low-mass stars, which would cause a smaller N_{Ly}/L ratio than for a normal cluster.

To find an explanation for the 67 objects falling above the cluster region, is instead non-trivial (see the discussion by Sánchez-Monge et al. 2013). In the following we will refer to the region above the solid curve in Fig. 5 as the “forbidden” region. We note that we have adopted the far distance for the sources for which the KDA could not be solved; this is a conservative choice, because assuming the near distance for these objects would increase the number of points falling in the forbidden region from 67 to 72. For the other points, mistaking the near with the far distance may indeed move some of them away from the forbidden region, but even assuming the far distance for *all* of the sources, only 17 out of 67 points would move to the right of the solid line in the figure. Moreover, one cannot appeal to an overestimate of the Lyman continuum flux, as previously explained. We have also verified the reliability of the $N_{\text{Ly}}-L$ relationship that we adopted. For this purpose, we plot in Fig. 6 the same relationship based on the results of various studies available in the literature. As one can see, none of the $N_{\text{Ly}}-L$ curves is consistent with all the points in the plot and some of them make the problem even worse.

Since it appears unlikely that we have overestimated the Lyman continuum flux, one may wonder whether we have underestimated the bolometric luminosity. An increase in L by a factor of 8 or less, would move all the points to the right out of the forbidden region. To test this possibility, we have recomputed the bolometric luminosity using the flux densities of the IRAS Point Source Catalogue counterparts of our sources. These counterparts have been selected by choosing the closest IRAS point source (if any) within 60'' from the HII region. Given the large IRAS HPBW at 100 μm (2'), the corresponding luminosity estimate is to be considered a conservative upper limit. However, ten sources still lie in the forbidden region, as demonstrated by Fig. 7. It is also worth noting that the number of points below the cluster region has dramatically increased with respect to Fig. 5, consistent with the idea that IRAS-based luminosities are by far too large. For these reasons, we consider Fig. 5 more reliable and will discuss this in the following.

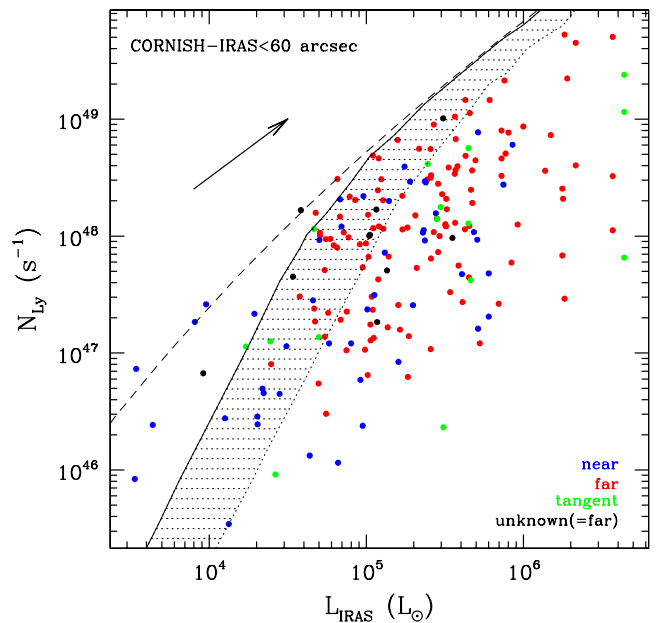


Fig. 7. Analogous to Fig. 5, where the bolometric luminosity computed from the Hi-GAL data has been replaced by that estimated from the IRAS fluxes.

Of course, we cannot rule out the possibility that a few objects in the forbidden zone are affected by an inappropriate estimate of L . In particular, some of the sources above the blackbody curve appear too extreme not to be misplaced. In Fig. 8 we compare the full width at half power (FWHP) at 70 μm of these sources with that of the other objects in the forbidden region lying below the blackbody curve. Clearly, the former are more extended than the latter and this could make it more difficult to estimate their integrated flux with CuTex (see Sect. 3.1), which was conceived to identify compact sources. Consequently, it is plausible that the luminosity might have been underestimated for some of these sources.

In conclusion, we believe that Fig. 5 proves that the CORNISH sample of HII regions contains a number of objects that really produce many more Lyman continuum photons than those emitted by a ZAMS star with the same bolometric luminosity. In the following, we will refer to this phenomenon as “Lyman excess”.

In Figs. 9 and 10, we compare the distributions in Galactic longitude and Galactocentric distance of the HII regions with Lyman excess to those of sources without Lyman excess. No significant difference can be seen between the two types in Fig. 9, while Fig. 10 seems to suggest that Lyman-excess sources are perhaps more concentrated in the 5 kpc ring than the others, although the difference is only marginally significant.

4.2. Nature of the Lyman-excess sources

The existence of HII regions with an excess of Lyman continuum emission was noted by Sánchez-Monge et al. (2013) and confirmed by Lumsden et al. (2013) and URQ13. These results, however, were obtained from low-resolution radio images and/or luminosity estimates based on IRAS data, whose limitations have already been discussed. Even when the 70 μm MIPS GAL fluxes were available, the angular resolution was still a factor of ~ 2 lower than in the Herschel images. The availability of the Hi-GAL and CORNISH unbiased surveys permits a more complete

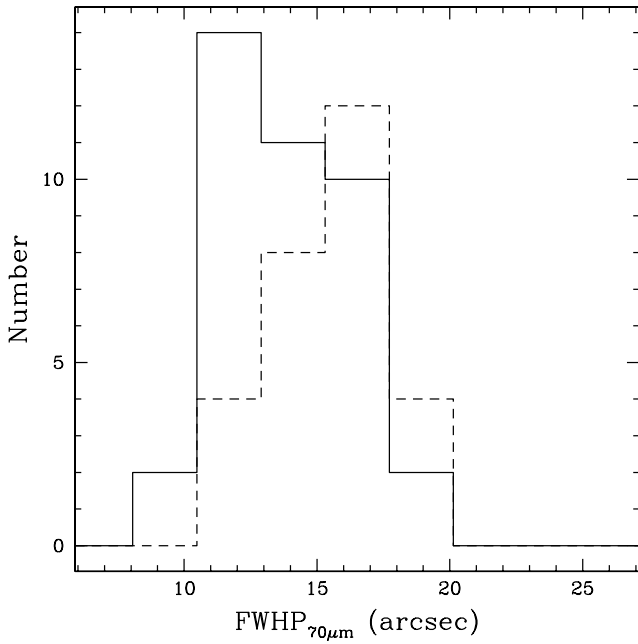


Fig. 8. Distributions of the angular size (FWHP) at $70 \mu\text{m}$ for sources in the forbidden region of Fig. 5, lying above (dashed histogram) and below (solid) the blackbody curve.

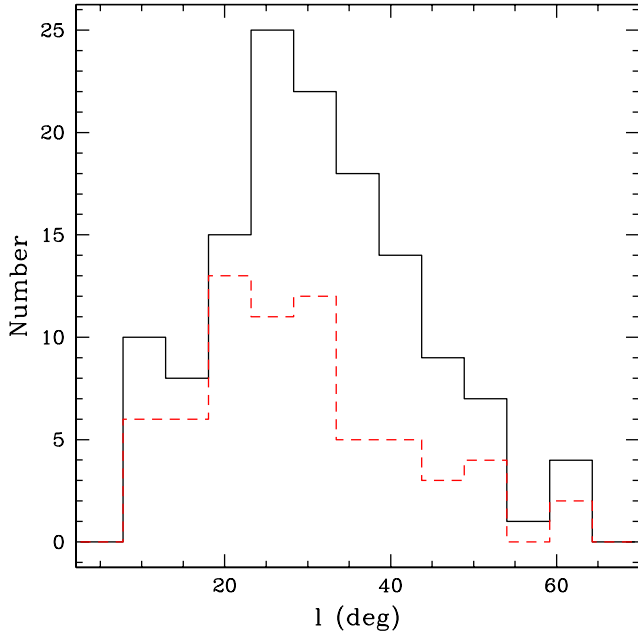


Fig. 9. Distributions of the Galactic longitude for sources with Lyman excess (dashed histogram, numbers on right axis) and without (solid histogram, numbers on left axis).

and systematic reconstruction of the SED of the HII regions at far-IR wavelengths, which is crucial for an accurate estimate of the luminosity.

An important step towards a better understanding of the Lyman excess is to discover the nature of the sources with this peculiarity. In Fig. 11 we compare the distribution of L/M_{gas} of the Lyman-excess sources with that of the others. This comparison suggests that the Lyman-excess sources are less luminous than the rest of the sample for the same mass of the associated clumps. The Kolmogorov-Smirnov (hereafter K-S) statistical test gives a null probability (7.4×10^{-5}) that the two sub-

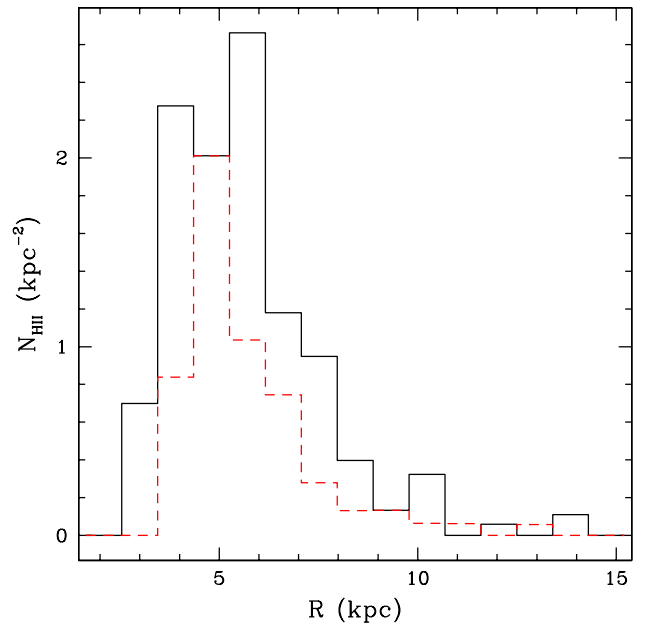


Fig. 10. Number of HII regions per unit surface as a function of Galactocentric distance for sources with Lyman excess (dashed histogram, numbers on right axis) and without (solid histogram, numbers on left axis).

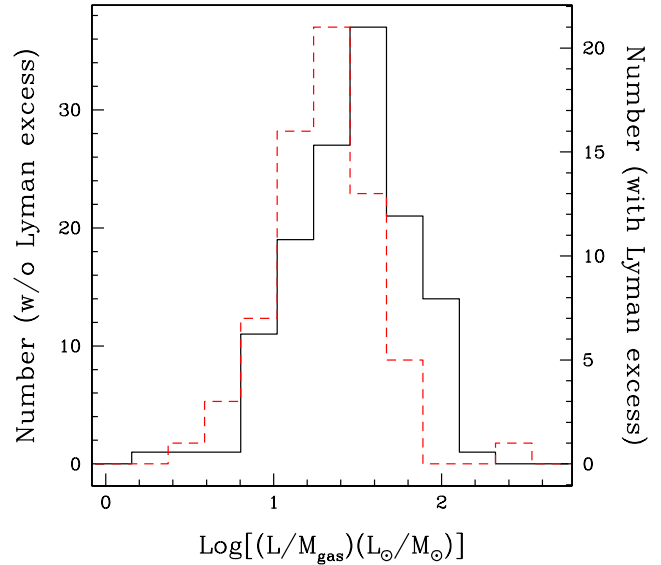


Fig. 11. Distributions of the luminosity-to-mass ratio for sources with Lyman excess (dashed histogram, numbers on right axis) and without (solid histogram, numbers on left axis).

samples in the figure have the same distribution, confirming the existence of a substantial difference between them. A possible interpretation is that the Lyman-excess sources are on average more deeply embedded and younger. Alternatively, the clumps might contain less massive stars, which – for the same star formation efficiency – would produce less luminosity. However, the second explanation seems inconsistent with the fact that the Lyman-excess sources are also those with the largest N_{Ly}/L ratio, as shown in Fig. 12, where according to the K-S test the probability that the two distributions are equivalent is basically zero (1.1×10^{-8}).

The possibility that these peculiar objects could be in an early, embedded evolutionary phase is also supported by other

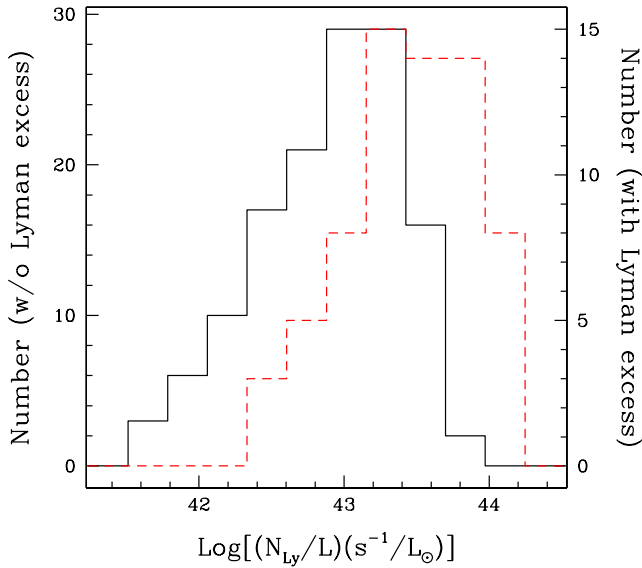


Fig. 12. Distributions of the ratio between Lyman continuum flux and bolometric luminosity for sources with Lyman excess (dashed histogram, numbers on right axis) and without (solid histogram, numbers on left axis).

findings. In Fig. 13 we plot the $[250-70]$ color⁴ versus a quantity representing the amount of Lyman excess. The latter is defined by the expression

$$\Delta_{\text{ex}} = \Delta(\text{Log} N_{\text{Ly}}) \frac{|\Delta(\text{Log} L)|}{\sqrt{[\Delta(\text{Log} N_{\text{Ly}})]^2 + [\Delta(\text{Log} L)]^2}}, \quad (2)$$

where $\Delta(\text{Log} N_{\text{Ly}})$ and $\Delta(\text{Log} L)$ are, respectively, the separations measured along the $\text{Log} N_{\text{Ly}}$ and $\text{Log} L$ axes between a given point in Fig. 5 and the solid curve delimiting the forbidden region. In practice this expression gives the approximate distance of the point from that curve, assumed negative to the right of the curve.

The line in Fig. 13 is obtained after rebinning the points on a number of intervals and shows some increase with increasing Lyman excess. This means that the Lyman-excess sources may have lower color temperatures than the rest of the sample, consistent with the hypothesis that these sources are younger and more deeply embedded inside cold dusty envelopes. This result is confirmed by the distributions of the color indices of the two samples, with and without Lyman excess (see Fig. 14), which have a probability of 2.9×10^{-4} of being intrinsically identical according to the K-S statistical test. Clearly, the sources with Lyman excess are on average “colder”, in terms of $[250-70]$, than those without, in agreement with the finding by Sánchez-Monge et al. (2013) that most of the sources with Lyman excess belong to their “type 2” class, consisting of embedded young massive stars still undergoing accretion.

Based on all of the above, we can speculate that the HII regions with Lyman excess could be ionized by young, mostly B-type stars still undergoing accretion. As discussed by Lumsden et al. (2013), our knowledge of early-type stars is based on visible stars, namely main-sequence stars that have dispersed their parental cocoons, but their properties might significantly differ from those of the young high-mass stars that we are considering in our study. Moreover, one cannot exclude that a signifi-

⁴ Defined as the ratio between the $250 \mu\text{m}$ and $70 \mu\text{m}$ flux densities: $[250 - 70] = \text{Log}(S_{250\mu\text{m}}/S_{70\mu\text{m}})$

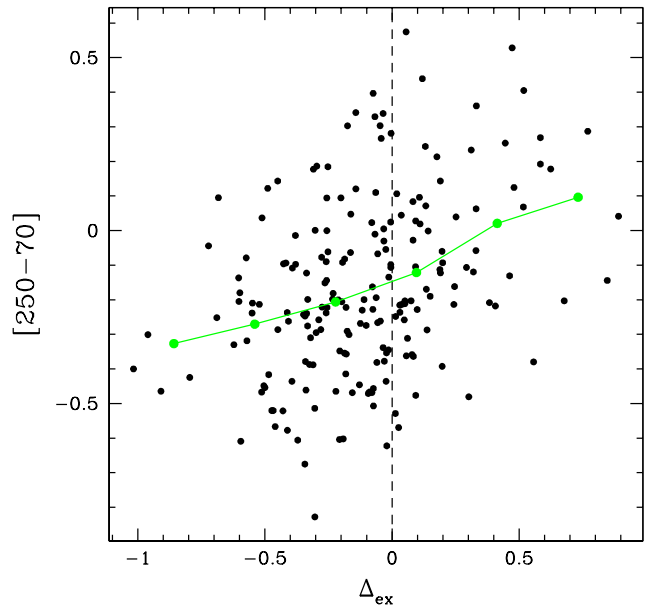


Fig. 13. Plot of the color index between $250 \mu\text{m}$ and $70 \mu\text{m}$ versus the parameter Δ_{ex} measuring the Lyman excess, defined in Eq. (2). The vertical dashed line marks the separation between sources with Lyman excess (i.e., with $\Delta_{\text{ex}} > 0$) and those without. The solid line connects points obtained after rebinning the data.

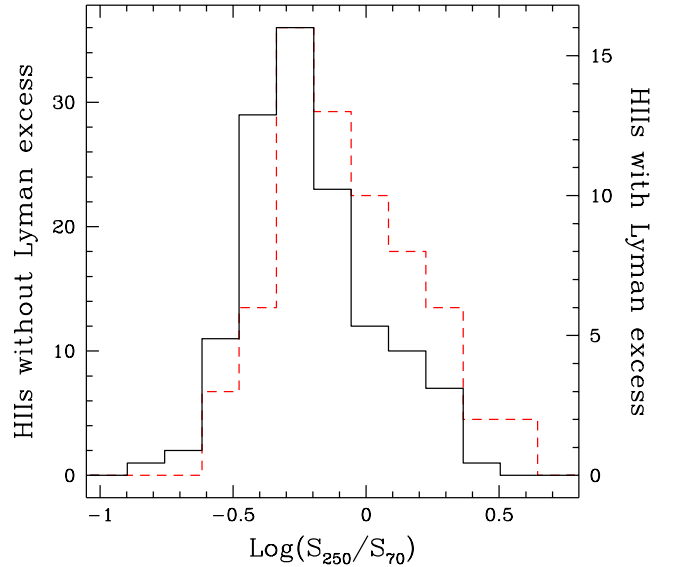


Fig. 14. Distribution of the color index between $250 \mu\text{m}$ and $70 \mu\text{m}$ for the sources with Lyman excess (dashed histogram, labels on right axis) and without (solid histogram, labels on left axis). We note how the latter is skewed towards lower color indices with respect to the former.

cant fraction of the Lyman continuum luminosity could originate from the accretion shock onto a circumstellar disk. Indeed, the model calculations by Hosokawa & Omukai (2009) appear to predict Lyman continuum fluxes comparable to or even greater than those of the star itself (Hosokawa, pers. comm.), possibly sufficient to explain the observed excess.

Also the model by Smith (2014) provides us with a possible explanation of the Lyman excess. In this model the protostar predominantly accumulates low entropy material via cold accretion, but then accretes onto hot spots covering a small fraction of the protostellar surface. The cold accretion assures that the young

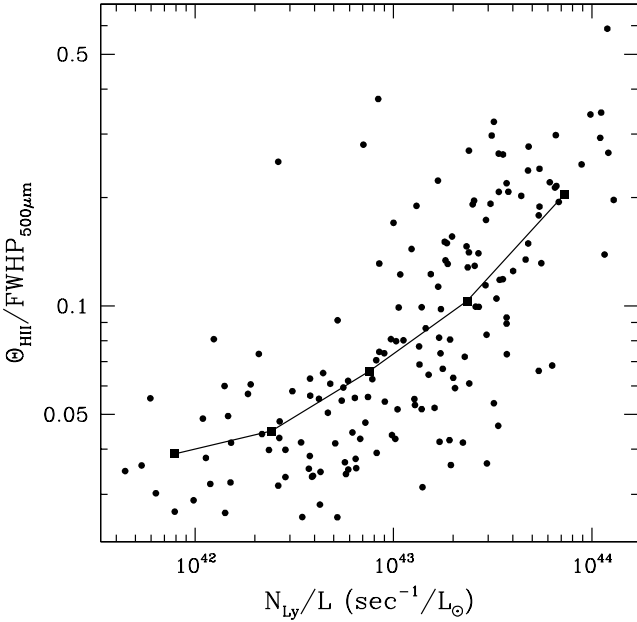


Fig. 15. Ratio between the HII region size (from the CORNISH catalogue) and the FWHP at $500 \mu\text{m}$ of the Hi-GAL counterpart, versus the ratio between the Lyman continuum photon rate and the bolometric luminosity. The solid curve was obtained by rebinning the data points.

star is relatively compact, which generates high free-fall speeds, while the free-fall onto the limited area significantly raises the temperature and hence the Lyman flux. In fact, a comparison between Figs. 15 and 16 of Smith (2014) and our Fig. 5 demonstrates the ability of the model to explain most of the Lyman-excess sources.

More detailed numerical calculations are needed in order to come to a firm conclusion on this issue, since a substantial improvement is necessary to predict the exact amount of Lyman continuum photons emitted in the accretion process.

4.3. Star formation efficiency

Our objects are bona fide young HII regions (see Sect. 2), and it is thus reasonable to assume that all sources are in a similar evolutionary phase, with the caveat that those with Lyman-excess might be slightly younger than the others (see Sect. 4.2). That our sample of HII regions spans a small range of ages can be verified by studying the size of the HII region as a function of stellar mass, which should depend on the mass of the star ionizing it. In this case one should find a correlation between HII region size and stellar mass. If, instead, the HII regions are in different evolutionary stages, no correlation should be found because the size of the HII region would depend not only on the stellar mass but also on the phase of expansion. In Fig. 15, we plot the ratio between the angular size of the HII region (Θ_{HII} , provided by the CORNISH catalogue; see Purcell et al. 2013) and the FWHP at $500 \mu\text{m}$ of the Hi-GAL counterpart as a function of the ratio N_{Ly}/L . We prefer to use ratios to get rid of any error related to the distance estimates. The ratio N_{Ly}/L increases with stellar mass, while $\Theta_{\text{HII}}/\text{FWHP}_{500\mu\text{m}}$ basically depends only on Θ_{HII} because the clump radius is only weakly dependent on the clump mass. Figure 15 shows a correlation between the two quantities (Spearman correlation coefficient 0.72), although with some spread, and confirms that all the regions are roughly coeval.

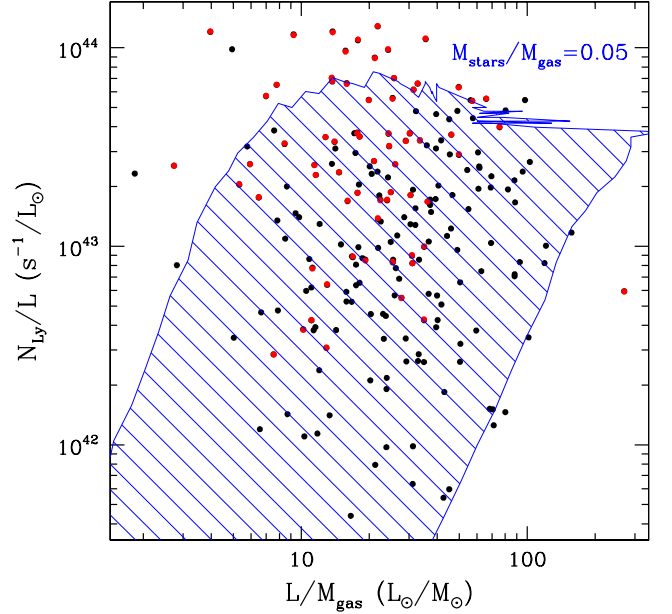


Fig. 16. Ratio between the Lyman continuum photon rate and the bolometric luminosity, versus the ratio between the luminosity and the clump mass for the CORNISH HII regions. The red points indicate sources with Lyman excess. The hatched area contains 90% of the simulated clusters assuming a star formation efficiency of 5%.

If our sample is indeed homogeneous, the observed distributions of mass, luminosity, and Lyman continuum emission should mirror the variation of the stellar cluster characteristics rather than a large spread in age. This can be verified by studying the ratios L/M_{gas} and N_{Ly}/L . Both should increase with time during the process of high-mass star formation because stars gain mass to the detriment of the surrounding envelope and thus increase their luminosities and Lyman continuum fluxes. Consequently, if our sources spanned a large age interval, one should observe a correlation between N_{Ly}/L and L/M_{gas} .

In Fig. 16 we plot these two ratios against each other for all of the 204 objects of our sample. We note that we have also included the four sources without V_{LSR} information because the L/M_{gas} and N_{Ly}/L do not depend on the distance. This feature makes the plot totally unaffected by the error on the distance. One does not see any significant correlation, consistent with the homogeneity of the sample. This allows us to obtain an estimate of the star formation efficiency. Using the same cluster simulations as in Sect. 4.1, we show in Fig. 16 the area over which 90% of the clusters should distribute, under the assumption that only 5% of the clump mass is converted into stars. The match between this region and the data points is very satisfactory, with the only exception being a handful of sources with the highest values of N_{Ly}/L . In the light of Sect. 4.1, this anomaly is not surprising, since these objects are the HII regions with the most prominent Lyman excess.

We note that a star formation efficiency of $\sim 5\%$ is in reasonable agreement with the value of 10% found by URQ13 for the same type of objects. These authors compared the clump mass with the luminosity and Lyman continuum emission, instead of their ratios (as we did in Fig. 16). Using the same approach (see Fig. 17), we confirm the existence of a correlation between L and M_{gas} , and N_{Ly} and M_{gas} . Following URQ13, we verified that such correlations were not due to the fact that all these quantities (L , N_{Ly} , and M_{gas}) scale like d^2 . For this purpose we performed a partial Spearman correlation test (see also Urquhart et al. 2013a

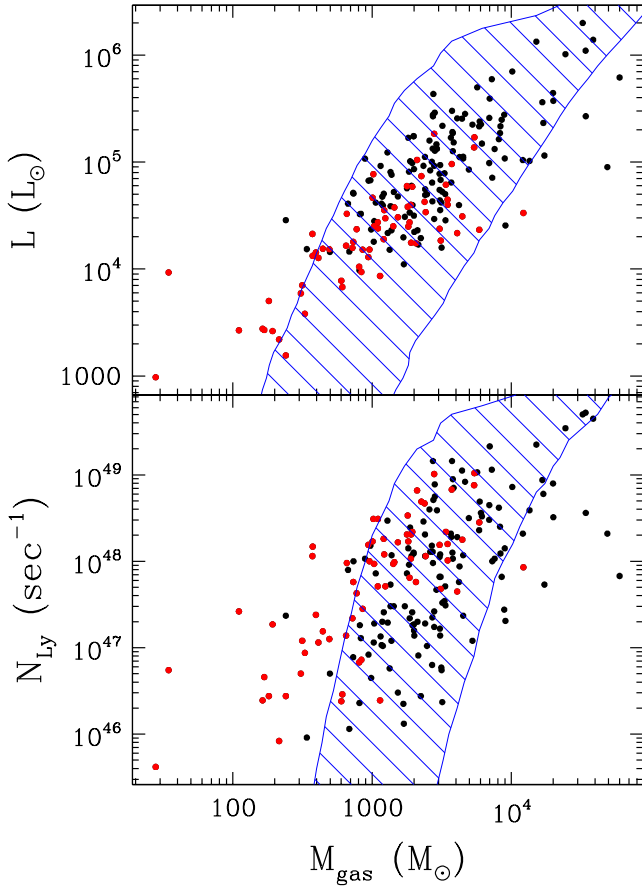


Fig. 17. Top: Bolometric luminosity versus clump mass for the CORNISH HII regions with estimated distance. The red points indicate sources with Lyman excess. The hatched area corresponds to 90% of the simulated clusters assuming a star formation efficiency of 5%. **Bottom:** Same as top panel for the Lyman continuum photon rate.

and references therein), which gives correlation coefficients of 0.72 for L , M_{gas} , and d , and 0.54 for N_{Ly} , M_{gas} , and d . For 197 degrees of freedom, these values correspond to a null probability that the correlations L vs M_{gas} and N_{Ly} vs M_{gas} are *not* significant. Comparison with cluster simulations (shaded blue region in Fig. 16) confirm a star formation efficiency of 5%, independent of mass and luminosity of the cluster. This is interpreted by URQ13 as evidence that more massive clumps form more massive stars.

4.4. Clump stability

We have also investigated whether the clumps associated with the selected HII regions are in virial equilibrium. To compute the virial mass, M_{vir} , one needs an estimate of the velocity dispersion in the molecular clumps, namely of the FWHM of a molecular line. This information is obviously missing in our continuum data, but we were able to recover it from the literature. Many of our targets have also been studied by URQ13, who estimated the corresponding M_{vir} using both new line observations and data from the literature. For the sake of comparison with our clump mass estimates, we scaled URQ13 virial masses to the distances and radii that we adopted. Moreover, we took the ammonia line widths from Wien et al. (2012) and Urquhart et al. (2011) to calculate M_{vir} for some of the sources not in URQ13. For the

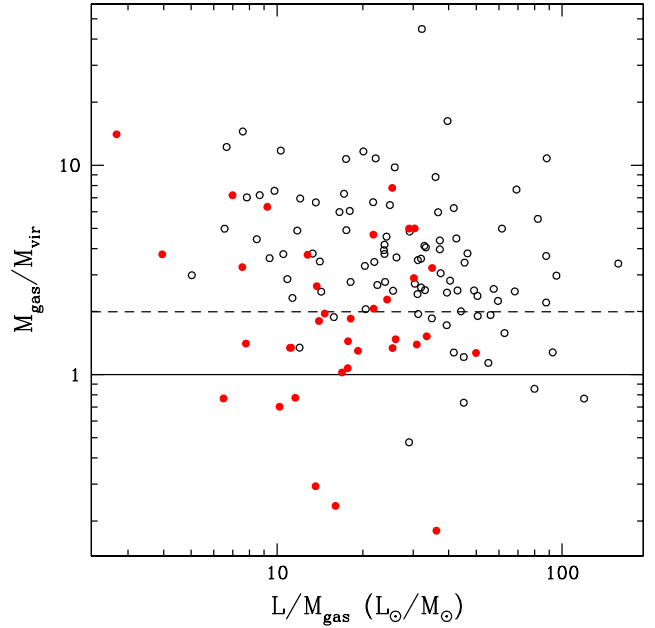


Fig. 18. Virial ratio as a function of the luminosity-to-mass ratio for all the sources for which a measurement of the line FWHM in a high density tracer is available. The solid points denote the sources with Lyman excess. The continuous line marks the equilibrium condition $M_{\text{gas}}/M_{\text{vir}}=1$ if only gravitation and turbulent motions are considered, while the dashed line corresponds to virial equilibrium when equipartition between kinetic and magnetic energy is assumed (see URQ13).

sake of consistency with these authors, we used their Eqs. (3) and (5) with the same assumptions.

In Fig. 18, we plot the virial ratio as a function of the ratio L/M_{gas} . If the clump stability changed during the evolution, one should find a correlation between the two quantities, as L/M_{gas} is expected to increase during star formation. No such trend is visible in the figure, and this is consistent with the previous conclusion that our sample spans a relatively narrow range of ages. The plot confirms the findings of URQ13, namely that almost all of the sources are supervirial. This is in agreement also with other studies (e.g., Fontani et al. 2002; Kauffmann et al. 2013) and supports the idea that clumps above $\sim 10^3 M_{\odot}$ in high-mass star forming regions are unstable against gravitational collapse.

In the same figure, we also make a distinction between sources with Lyman excess (red solid points) and those without (black empty points). Interestingly, the distribution of the former appears skewed to the bottom left of the plot. This is confirmed by the mean values of the logarithms of the two ratios, which are $\langle \text{Log}(M_{\text{gas}}/M_{\text{vir}}) \rangle = 0.26$ for the Lyman-excess sources and 0.55 for the others, and $\langle \text{Log}(L/M_{\text{gas}}) \rangle = 1.2$ for the Lyman-excess sources and 1.4 for the others. According to the K-S test, the probability that sources with and without Lyman-excess have the same distribution is 3×10^{-4} for $\text{Log}(L/M_{\text{gas}})$ and 5×10^{-5} for $\text{Log}(M_{\text{gas}}/M_{\text{vir}})$, which supports the existence of a real difference between the two samples. These findings hint at slightly different evolutionary phases for the two types of objects, with the Lyman-excess sources being embedded in clumps closer to virial equilibrium and thus at the beginning of the collapse phase. In particular, it is worth noting that only 42% of the Lyman-excess sources have $M_{\text{gas}}/M_{\text{vir}} > 2$ (the critical value for clumps in virial equilibrium assuming equipartition between kinetic and magnetic energy; see URQ13), as opposed to 83% of the other xxx sources.

5. Summary and conclusions

We have identified the Herschel/Hi-GAL IR counterparts of the young HII regions detected in the CORNISH survey, with the aim of studying the properties of the associated early-type stars and possibly of drawing some conclusion on the star formation process. Out of 281 HII regions, we were able to reconstruct the SED for 204 objects. We determined the bolometric and Lyman continuum luminosity for 200 of these because it was not possible to obtain a kinematic distance estimate for four HII regions in the sample. We also estimated the masses of the associated molecular clumps from the (sub)millimeter flux densities.

We find that 67 objects present a “Lyman excess”, as the Lyman continuum emission exceeds the maximum value expected for the same bolometric luminosity. No definitive explanation can be identified for this effect. We propose that infall onto the star and/or an associated accretion disk might cause the shocked material to emit additional UV photons that add up to the normal Lyman continuum of the OB star. While some models appear to support this interpretation, significant progress in the numerical calculations is still needed to prove our hypothesis and demonstrate that HII regions are undergoing accretion during a considerable fraction of their lives.

We construct a distance-independent plot of the ratio between the Lyman continuum and bolometric luminosity versus the ratio between the bolometric luminosity and corresponding clump mass, and use cluster simulations to fit the observed distribution in this plot. The result is that a good match is found if only 5% of the clump mass is converted into stars, consistent with previous estimates of the star formation efficiency in similar objects.

Finally, we find that the majority of clumps associated with all HII regions of our sample are supervirial and hence unstable against gravitational collapse. However, those associated with Lyman-excess sources are on average closer to equilibrium, hinting at these objects being in a slightly earlier evolutionary phase.

Acknowledgements. GSS acknowledges support received through grants awarded by NASA. Herschel Hi-GAL data processing, maps production and source catalogue generation have been possible thanks to Contracts I/038/080/0 and I/0 29/12/0 from ASI, Agenzia Spaziale Italiana. This paper made use of information from the Red MSX Source survey database at http://rms.leeds.ac.uk/cgi-bin/public/RMS_DATABASE.cgi which was constructed with support from the Science and Technology Facilities Council of the UK. This publication also makes use of data products from the Wide-field Infrared Survey Explorer, which is a joint project of the University of California, Los Angeles, and the Jet Propulsion Laboratory/California Institute of Technology, funded by the National Aeronautics and Space Administration. This research made use of data products from the Midcourse Space Experiment. Processing of the data was funded by the Ballistic Missile Defense Organization with additional support from NASA Office of Space Science. This research has also made use of the NASA/IPAC Infrared Science Archive, which is operated by the Jet Propulsion Laboratory, California Institute of Technology, under contract with the National Aeronautics and Space Administration.

References

- Anderson, L.D. & Bania, T.M. 2009, *ApJ*, 690, 706
 Anderson, L.D., Bania, T.M., Balser, D.S., & Rood, R.T. 2012, *ApJ*, 754, 62
 Beuther, H., Schilke, P., Menten, K.M., et al. 2002, *ApJ*, 566, 945
 Brand, J. & Blitz, L. 1993, *A&A*, 275, 67
 Bronfman, L., Casassus, S., May, J., Nyman, L.-Å. 1996, *A&AS*, 115, 81
 Contreras, Y., Schuller, F., Urquhart, J. S., et al. 2013, *A&A*, 549, A45
 Crowther, P.A. 2005, in *Massive Star Birth: a Crossroads of Astrophysics*, IAU Symposium 227, ed. R. Cesaroni, M. Felli, E. Churchwell, M. Walmsley (Cambridge University Press), 389
 Davies, B., Hoare, M.G., Lumsden, S.L., et al. 2011, *MNRAS*, 416, 972
 Diaz-Miller, R.I., Franco, J., & Shore, S.N. 1998, *ApJ*, 501, 192
 Fontani, F., Cesaroni, R., Caselli, P., & Olmi, L. 2002, *A&A*, 389, 603
 Ginsburg, A., Glenn, J., Rosolowsky, E., et al. 2013, *ApJS*, 208, 14

- Hoare, M.G., Purcell, C.R., Churchwell, E.B., et al. 2012, *PASP*, 124, 939
 Hosokawa, T. & Omukai, K. 2009, *ApJ*, 691, 823
 Jones, C. & Dickey, J.M. 2012, *ApJ*, 753, 62
 Kauffmann, J., Pillai, T., & Goldsmith, P.F. 2013, *ApJ*, 779, 185
 Kolpak, M.A., Jackson, J.M., Bania, T.M., Clemens, D.P., & Dickey, J.M. 2003, *ApJ*, 582, 756
 Kroupa, P., Tout, C.A., Gilmore, G. 1993, *MNRAS*, 262, 545
 Kurtz, S. 2005, in *Massive Star Birth: a Crossroads of Astrophysics*, IAU Symposium 227, ed. R. Cesaroni, M. Felli, E. Churchwell, M. Walmsley (Cambridge University Press), 111
 Lumsden, S.L., Hoare, M.G., Urquhart, J.S., et al. 2013, *ApJS*, 208, 11
 Martins, F., Schaerer, D., & Hillier, D.J. 2005, *A&A*, 436, 1049
 Molinari, S., Swinyard, B., Bally, J., et al. 2010, *PASP*, 122, 314
 Molinari, S., Schisano, E., Faustini, F., et al. 2011, *A&A*, 530, A133
 Mottram, L., Hoare, M.G., Davies, B., et al. 2011, *ApJ*, 730, L33
 Ossenkopf, V. & Henning, Th. 1994, *A&A*, 291, 943
 Panagia, N. 1973, *AJ*, 78, 929
 Pandian, J.D., Momjian, E., & Goldsmith, P.F. 2008, *A&A*, 486, 191
 Pilbratt, G.L., Riedinger, J.R., Passvogel, T., et al. 2010, *A&A*, 518, L1
 Price, S.D., Egan, M.P., & Shipman, R.F. 1999, *Astrophysics with Infrared Surveys: A prelude to SIRTF*, 177, 394
 Purcell, C.R., Hoare, M.G., Cotton, W.D., et al. 2013, *ApJS*, 205, 1
 Quireza, C., Rood, R.T., Bania, T.M., Balser, D.S., & Maciel, W.J. 2006, *ApJ*, 653, 1226
 Robitaille, T.P., Whitney, B.A., Indebetouw, R., & Wood, K. 2007, *ApJS*, 169, 328
 Sánchez-Monge, Á., Beltrán, M.T., Cesaroni, R., et al. 2013, *A&A*, 550, A21
 Shirley, Y.L., Ellsworth-Bowers, T.P., Svoboda, B., et al. 2013, *ApJS*, 209, 2
 Schuller, F., Menten, K.M., Contreras, Y., et al. 2009, *A&A*, 504, 415
 Sewilo, M., Watson, C., Araya, E., et al. 2004, *ApJS*, 154, 553
 Smith, M.D. 2014, *MNRAS*, 438, 1051
 Smith, L.J., Norris, R.P.F., Crowther, P.A. 2002, *MNRAS*, 337, 1309
 Thompson, R.I. 1984, *ApJ*, 283, 165
 Urquhart, J.S., Morgan, L.K., Figura, C.C., et al. 2011, *MNRAS*, 418, 1689
 Urquhart, J.S., Moore, T.J.T., Schuller, F., et al. 2013a, *MNRAS*, 431, 1752
 Urquhart, J.S., Thompson, M.A., Moore, T.J.T., et al. 2013b, *MNRAS*, 435, 400 (URQ13)
 Vacca, W.D., Garmany, C.D., & Shull, M. 1996, *ApJ*, 460, 914
 Watson, C., Araya, E., Sewilo, M., et al. 2003, *ApJ*, 587, 714
 White, R.L., Becker, R.H., & Helfand, D.J. 2005, *AJ*, 130, 586
 Wienen, M., Wyrowski, F., Schuller, F., et al. 2012, *A&A*, 544, A146
 Wood, D.O.S. & Churchwell, E. 1989, *ApJ*, 340, 265
 Wright, E.L., Eisenhardt, P.R.M., Mainzer, A.K., et al. 2010, *AJ*, 140, 1868

Appendix A: ON-LINE MATERIAL

Table A.1. continued

#	CORNISH name	α_{CORNISH} (deg)	δ_{CORNISH} (deg)	$S_{5\text{GHz}}$ (mJy)	$\alpha_{\text{Hi-GAL}}$ (deg)	$\delta_{\text{Hi-GAL}}$ (deg)	$S_{21\mu\text{m}}$ (Jy)	$S_{22\mu\text{m}}$ (Jy)	$S_{70\mu\text{m}}$ (Jy)	$S_{160\mu\text{m}}$ (Jy)	$S_{250\mu\text{m}}$ (Jy)	$S_{350\mu\text{m}}$ (Jy)	$S_{500\mu\text{m}}$ (Jy)	$S_{870\mu\text{m}}$ (Jy)	$S_{1100\mu\text{m}}$ (Jy)
181	G045.4545+00.0591	288.5888	11.1532	1081.0	288.5880	11.1542	497.60	3387.00	1738.00	808.60	471.30	174.90	59.89	—	14.29
182	G045.4656+00.0452	288.6070	11.1570	62.3	288.6066	11.1575	—	37.92	1468.00	1223.00	898.10	232.00	67.14	—	6.91
183	G045.4790+00.1294	288.5362	11.2066	504.2	288.5381	11.2076	172.70	—	240.70	219.10	263.60	—	—	—	9.46
184	G045.5431-00.0073	288.6906	11.2014	49.2	288.6906	11.2014	7.95	9.67	190.20	132.70	77.02	23.62	8.23	—	0.67
185	G048.6099+00.0270	290.1277	13.9284	131.2	290.1299	13.9239	31.11	—	1551.00	865.40	545.30	142.00	40.28	—	—
186	G048.9296-00.2793	290.5624	14.0669	185.4	290.5632	14.0676	34.85	—	294.90	235.20	—	56.37	68.47	—	—
187	G048.9901-00.2988	290.6088	14.1110	7.5	290.6094	14.1117	107.50	—	737.50	847.30	918.10	236.70	105.80	—	17.17
188	G049.2679-00.3374	290.7791	14.3377	102.6	290.7781	14.3369	4.94	9.91	432.60	804.40	869.70	310.90	112.80	—	11.08
189	G049.4891-00.3763	290.9227	14.5143	217.3	— ^a	— ^a	1658.00	—	1934.00	3583.00	1747.00	792.60	289.00	—	—
190	G049.4905-00.3688	290.9164	14.5193	3821.7	— ^a	— ^a	2687.90	—	8145.00	4770.00	1720.00	730.90	245.30	—	103.60
191	G050.2834-00.3904	291.3269	15.2078	156.8	291.3246	15.2071	60.79	94.40	1236.00	596.80	372.10	81.00	20.73	—	1.83
192	G050.3152+00.6762	290.3646	15.7392	154.6	290.3647	15.7389	38.42	54.81	581.40	394.50	257.10	60.28	18.63	—	—
193	G051.6785+00.7193	290.9951	16.9615	22.5	290.9949	16.9614	14.00	17.01	695.30	585.40	459.60	141.00	44.33	—	—
194	G052.7533+00.3340	291.8842	17.7241	386.0	291.8831	17.7228	18.78	26.63	97.21	213.40	129.50	38.40	14.10	—	1.04
195	G053.1865+00.2085	292.2180	18.0455	96.1	292.2177	18.0448	11.01	13.30	132.30	121.40	99.79	35.94	14.79	—	1.53
196	G053.9589+00.0320	292.7717	18.6380	46.0	292.7719	18.6380	31.88	36.66	248.40	215.60	168.10	51.48	16.97	—	1.34
197	G058.7739+00.6457	294.7027	23.1445	4.8	294.7031	23.1441	29.80	45.90	430.80	345.00	228.30	59.93	18.01	—	—
198	G059.6027+00.9118	294.8943	23.9970	68.8	294.8935	23.9968	8.34	10.04	589.30	493.90	369.20	89.41	27.51	—	—
199	G060.8838-00.1295	296.5866	24.5876	292.1	296.5833	24.5911	—	3269.00	1500.00	931.50	839.80	281.70	84.48	—	—
200	G060.8842-00.1286	296.5839	24.5915	18.7	296.5833	24.5912	286.60	45.02	1625.00	1122.00	976.50	315.20	113.20	—	18.59
201	G061.2875-00.3327	297.0004	24.8384	159.4	296.9973	24.8376	8.09	13.29	62.30	67.42	25.98	8.49	4.14	—	1.13
202	G061.4763+00.0892	296.7044	25.2122	785.6	296.7038	25.2138	589.50	—	4404.00	2758.00	1091.00	492.10	170.60	—	—
203	G061.7207+00.8630	296.0985	25.8121	101.3	296.0984	25.8119	19.44	23.72	253.30	141.30	90.73	24.83	7.87	—	—
204	G065.2462+00.3505	298.6068	28.5898	4.6	298.6053	28.5895	—	0.40	3.90	17.60	11.97	5.87	2.54	—	—

^a the peak coordinates could not be determined because some of the Hi-GAL images are saturated

Table A.2. Distances, Lyman continuum photon rates, bolometric luminosities, and clump masses of the 200 HII regions of our sample for which a distance estimate was possible. The sequential number identifying each source is the same as in Table A.1.

#	d (kpc)	$\text{Log}N_{\text{Ly}}$ $\text{Log}(s^{-1})$	$\text{Log}L$ $\text{Log}(L_{\odot})$	$\text{Log}M_{\text{gas}}$ $\text{Log}(M_{\odot})$
1	12.6 ^a	47.71	4.70	3.53
2	4.0	46.46	3.83	2.79
3	10.9	47.83	5.79	4.78
4	4.9	48.78	5.37	4.23
5	13.7	48.56	5.35	3.78
6	3.0	46.66	3.43	2.22
7	2.7	45.62	2.99	1.45
8	14.3	48.32	5.23	3.57
9	16.9	48.94	5.56	4.22
10	12.8 ^a	48.22	4.48	3.18
11	4.2	46.86	3.97	2.92
12	12.5	49.16	5.48	3.57
14	11.8	47.94	5.05	3.63
15	13.3	48.56	5.43	4.53
16	13.8	47.93	4.52	4.09
17	4.2	47.08	4.36	3.14
18	2.0	45.92	3.34	2.33
19	4.7	48.31	4.25	3.28
20	2.1	47.42	3.43	2.04
21	4.5	48.46	4.97	3.37
22	14.7 ^a	48.01	4.60	3.54
23	2.8	46.44	3.19	2.38
24	13.0	47.48	4.49	3.23
25	12.3	47.34	4.53	3.27
26	12.2 ^a	48.26	4.28	3.08
27	16.9	49.16	5.43	3.44
28	10.4	46.76	4.18	3.13
29	10.4 ^a	47.26	4.51	2.91
30	14.0	47.14	4.35	3.30
31	13.7 ^a	47.29	4.34	3.11
32	4.3	48.19	4.11	2.97
33	3.1	48.08	4.55	3.09
34	11.9	48.06	4.53	3.38
35	12.0	48.69	5.38	3.77
36	12.5 ^a	48.23	4.40	3.26
37	13.4 ^a	48.28	4.81	3.57
38	14.0	48.00	4.85	3.86
39	4.6	46.38	3.89	2.78
40	12.5	48.31	5.05	3.38
41	11.3	46.91	4.23	3.33
42	4.7	48.05	4.74	3.48
43	13.7	48.88	5.14	3.73
44	13.0	48.11	4.92	3.42
45	12.5	49.65	6.14	4.59
46	11.8	48.23	4.67	3.00
47	4.4	46.70	3.77	2.49
48	14.0	48.67	4.63	3.38
49	9.2	47.48	4.91	3.13
50	12.6	48.90	5.65	4.30
51	4.0	46.94	3.58	2.52
52	17.4	47.48	4.72	3.16
53	11.6	47.13	4.96	3.06
54	13.1	47.28	4.45	3.02
55	10.2	47.41	4.70	3.08
56	10.2	48.07	5.05	3.65
57	4.1	47.19	4.19	2.65
58	16.1	47.71	4.47	3.10
59	13.7	49.02	5.23	3.73
60	5.0	46.39	3.93	3.06

Table A.2. continued

#	d (kpc)	$\text{Log}N_{\text{Ly}}$ $\text{Log}(s^{-1})$	$\text{Log}L$ $\text{Log}(L_{\odot})$	$\text{Log}M_{\text{gas}}$ $\text{Log}(M_{\odot})$
61	5.0	47.34	4.20	2.86
62	6.2	46.74	3.97	1.54
63	5.3	46.36	3.99	2.91
64	6.7	47.96	4.91	3.27
65	10.7	47.65	4.34	3.61
66	12.5	47.82	4.83	3.49
67	5.1	48.47	5.09	3.11
68	7.8	46.35	4.30	3.22
69	6.1	47.31	4.41	3.96
70	6.1	47.68	4.27	3.49
71	6.5	47.76	4.60	3.62
72	6.0	47.86	4.62	3.03
73	6.5	46.92	4.83	2.97
74	3.3	47.27	3.42	2.29
75	14.1 ^a	48.00	4.70	2.87
76	4.1	48.03	5.03	2.95
77	16.9	48.92	5.45	3.67
78	13.9	48.52	5.17	3.79
79	5.8	48.85	5.18	3.59
80	9.4	47.26	4.60	3.29
81	5.7	47.02	4.59	3.08
83	12.9	47.28	4.75	3.38
84	12.9	46.89	4.71	2.86
85	9.8	48.60	5.20	3.41
86	13.2	48.08	4.97	3.49
87	7.6	48.06	4.33	2.57
89	13.0	47.52	5.34	3.51
90	12.6	48.83	4.98	3.57
91	9.5	47.73	5.06	4.24
92	9.8	48.19	4.38	3.48
93	11.9	46.80	4.81	3.43
94	4.8	47.45	4.18	2.93
95	6.0	48.03	5.12	3.88
96	8.3	47.63	4.37	2.89
97	11.6	48.86	5.85	4.01
98	6.0	47.08	3.85	2.50
99	16.4	48.03	4.60	3.28
100	8.5	48.18	5.00	3.43
101	8.4	48.20	4.65	3.54
102	9.6	47.98	4.52	2.82
103	8.5	49.35	6.13	4.18
104	7.9	46.44	4.29	3.35
105	10.1	47.99	4.58	3.16
106	11.3	48.03	5.10	3.58
107	11.3	48.95	5.27	3.58
108	11.6	48.09	5.34	3.92
109	8.4	48.32	4.95	4.69
110	6.6	47.06	4.26	3.01
111	11.8	48.65	5.41	3.84
112	11.7	47.54	4.89	3.52
113	12.1	47.30	4.36	3.33
114	13.2	47.30	4.68	3.07
115	11.8	48.53	4.58	3.26
116	2.8	46.39	3.44	2.21
117	12.9	49.05	5.41	3.65
118	7.3	48.15	5.03	3.95
119	5.7	47.41	4.99	3.29
120	6.4	48.59	5.01	4.13

Table A.2. continued

#	d (kpc)	$\text{Log}N_{\text{Ly}}$ $\text{Log}(s^{-1})$	$\text{Log}L$ $\text{Log}(L_{\odot})$	$\text{Log}M_{\text{gas}}$ $\text{Log}(M_{\odot})$
121	6.4	46.77	4.62	3.50
122	7.2	47.14	4.22	2.81
123	6.4	48.34	4.79	3.53
124	12.6	48.69	4.87	3.35
125	10.9	48.06	4.78	3.28
126	12.8	46.74	4.20	3.50
127	11.6	47.24	4.47	3.45
128	13.1	49.72	6.04	4.53
129	19.0	49.01	5.26	3.45
130	9.2	48.50	4.93	3.69
131	9.3	47.81	4.44	3.27
132	10.9	48.10	5.24	3.30
133	10.9	48.09	5.24	3.30
134	7.1	48.62	5.21	3.91
135	11.6	47.11	4.52	2.92
136	11.5	48.75	5.11	3.45
137	10.1	47.02	4.70	3.39
138	3.9	46.12	4.04	3.23
139	16.5	47.73	4.59	3.13
140	10.4	47.08	5.35	3.72
141	10.4	47.86	4.76	3.25
142	9.5 ^a	46.83	4.02	2.91
143	8.5	48.36	5.33	3.77
144	10.4	48.48	4.99	3.84
145	10.2	48.28	5.41	3.61
146	4.0	46.70	4.16	2.70
147	9.8	48.59	5.12	3.47
148	10.2	47.22	4.64	3.49
149	12.1	47.71	4.44	3.04
150	9.2	48.45	4.37	3.77
151	12.1	47.82	4.89	3.48
152	9.9	48.31	4.78	3.25
153	9.2	49.33	5.59	3.85
154	16.6	47.76	4.25	2.87
155	4.9	46.44	3.70	2.26
156	17.1	47.35	4.63	3.43
157	9.7	47.27	4.50	3.30
158	14.7	48.82	5.02	3.32
159	15.7	48.18	4.83	2.99
160	8.8	48.00	4.18	2.98
161	8.9	48.34	4.77	3.29
162	12.0	47.20	4.93	3.30
163	11.7	48.49	4.89	3.01
164	8.5	47.03	4.61	3.07
165	5.3	47.37	4.46	2.38
166	12.1	49.03	5.70	3.76
167	11.4	49.54	6.01	4.39
168	12.2	49.70	6.30	4.51
169	12.2	48.51	5.57	4.30
170	11.5	48.32	5.02	4.08
171	8.0	48.06	4.69	3.38
172	11.9	48.40	5.27	3.92
173	4.8	46.65	4.37	2.99
174	9.0	47.44	5.44	3.95
175	4.2	47.97	4.40	3.01
176	14.0	47.90	4.61	2.83
177	7.5	46.48	4.68	3.18
178	18.2	47.14	4.55	3.49
179	5.0	47.67	5.17	3.46
180	5.1	48.89	5.46	3.45

Table A.2. continued

#	d (kpc)	$\text{Log}N_{\text{Ly}}$ $\text{Log}(s^{-1})$	$\text{Log}L$ $\text{Log}(L_{\odot})$	$\text{Log}M_{\text{gas}}$ $\text{Log}(M_{\odot})$
181	6.9	48.71	5.64	3.44
182	6.6	47.42	4.97	3.45
183	6.0	48.25	4.49	3.65
184	7.0	47.38	4.16	2.60
185	9.8	48.10	5.28	3.58
186	5.6	47.76	4.24	3.32
187	5.6	46.37	4.72	3.50
188	5.6	47.49	4.46	3.53
189	5.5	47.82	5.40	3.93
190	5.5	49.06	5.78	3.86
191	9.5	48.15	5.23	3.26
192	8.8	48.07	4.88	3.14
193	10.2	47.37	5.03	3.65
194	9.0	48.49	4.38	3.04
195	9.9	47.97	4.40	3.15
196	5.0	47.06	4.10	2.61
197	4.4	45.96	4.19	2.53
198	4.3	47.10	4.18	2.69
199	5.8 ^a	47.98	5.44	3.44
200	2.5	46.06	4.16	2.84
201	9.6	48.17	4.12	2.57
202	4.1	48.11	5.13	3.43
203	15.7	48.39	5.01	3.27

^a KDA not solved: far kinematic distance adopted (see Sect. 3.2)

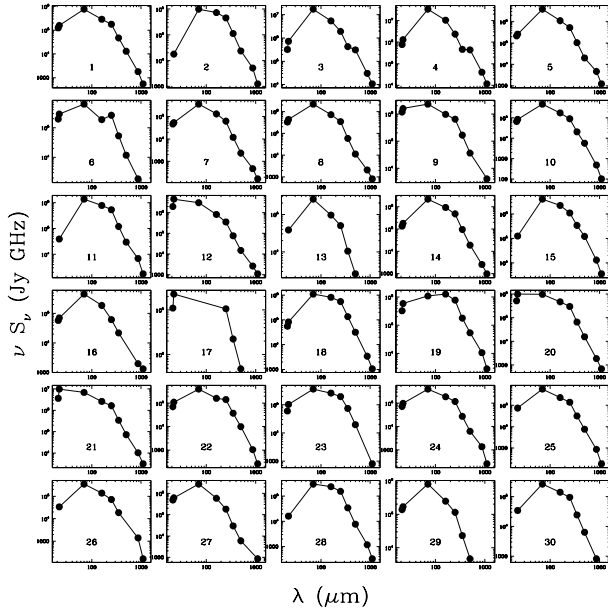


Fig. A.1. Spectral energy distributions of the CORNISH HII regions with Hi-GAL counterparts of at least three bands. In addition to Hi-GAL, the MSX 21 μm , WISE 22 μm , ATLASGAL 870 μm , and BGPS 1.1 mm flux densities have also been used. The number in each box identifies the source according to the numbering in Table A.1.

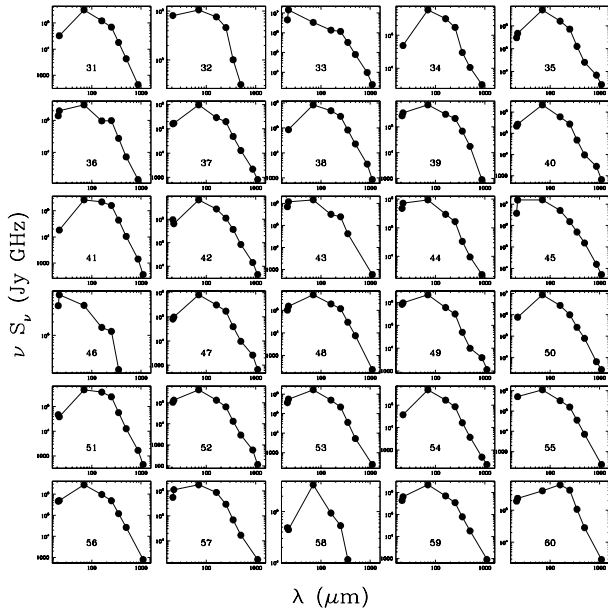


Fig. A.1. continued

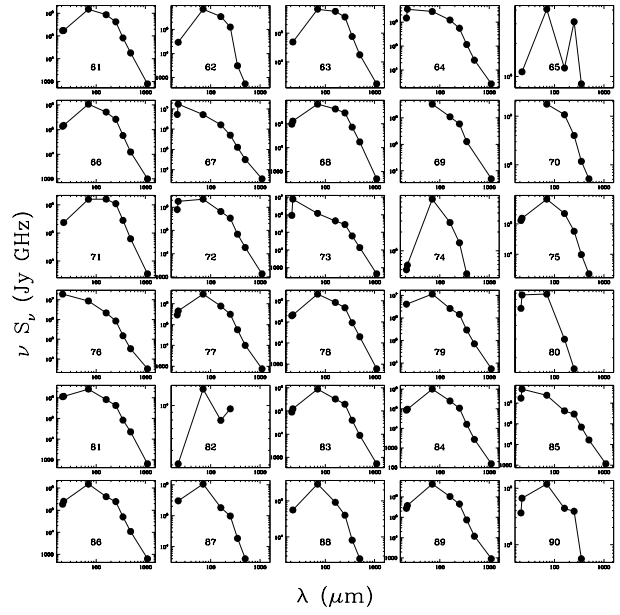


Fig. A.1. continued

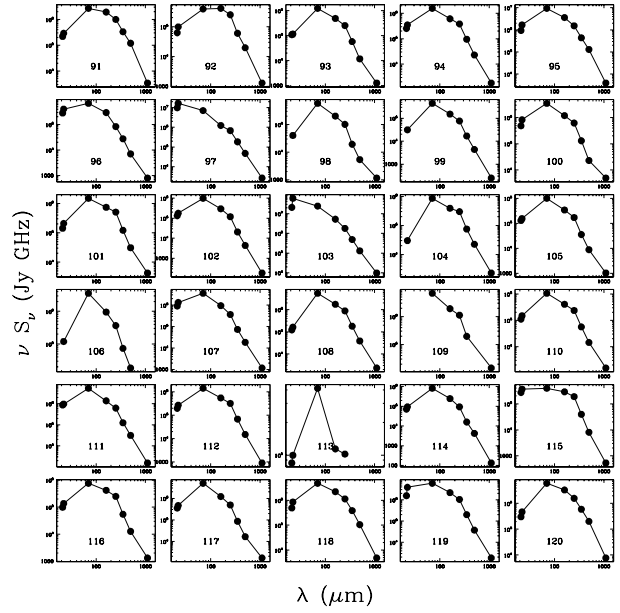


Fig. A.1. continued

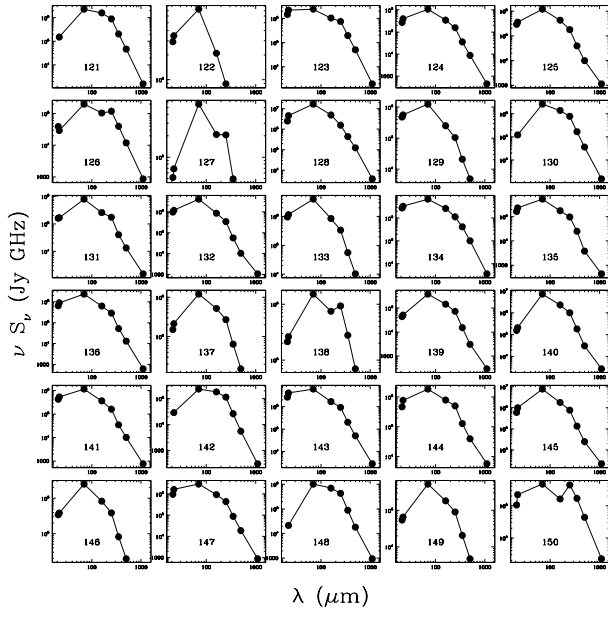


Fig. A.1. continued

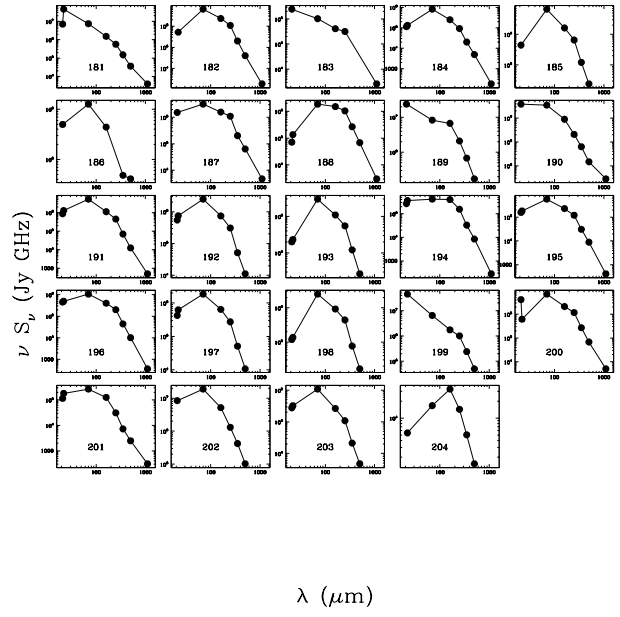


Fig. A.1. continued

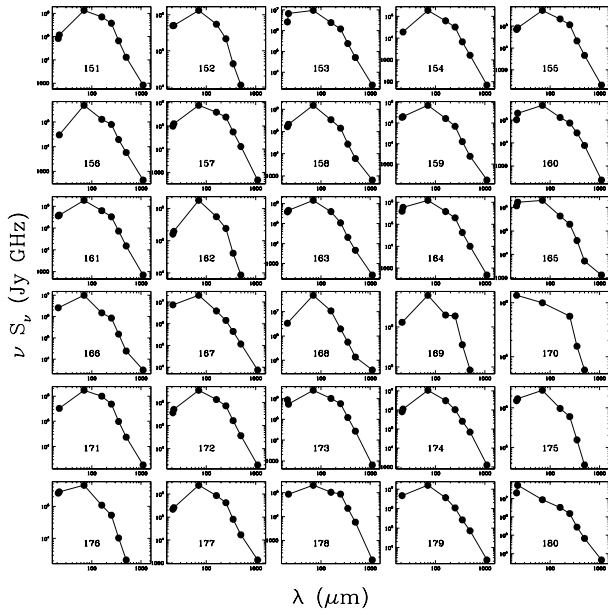


Fig. A.1. continued

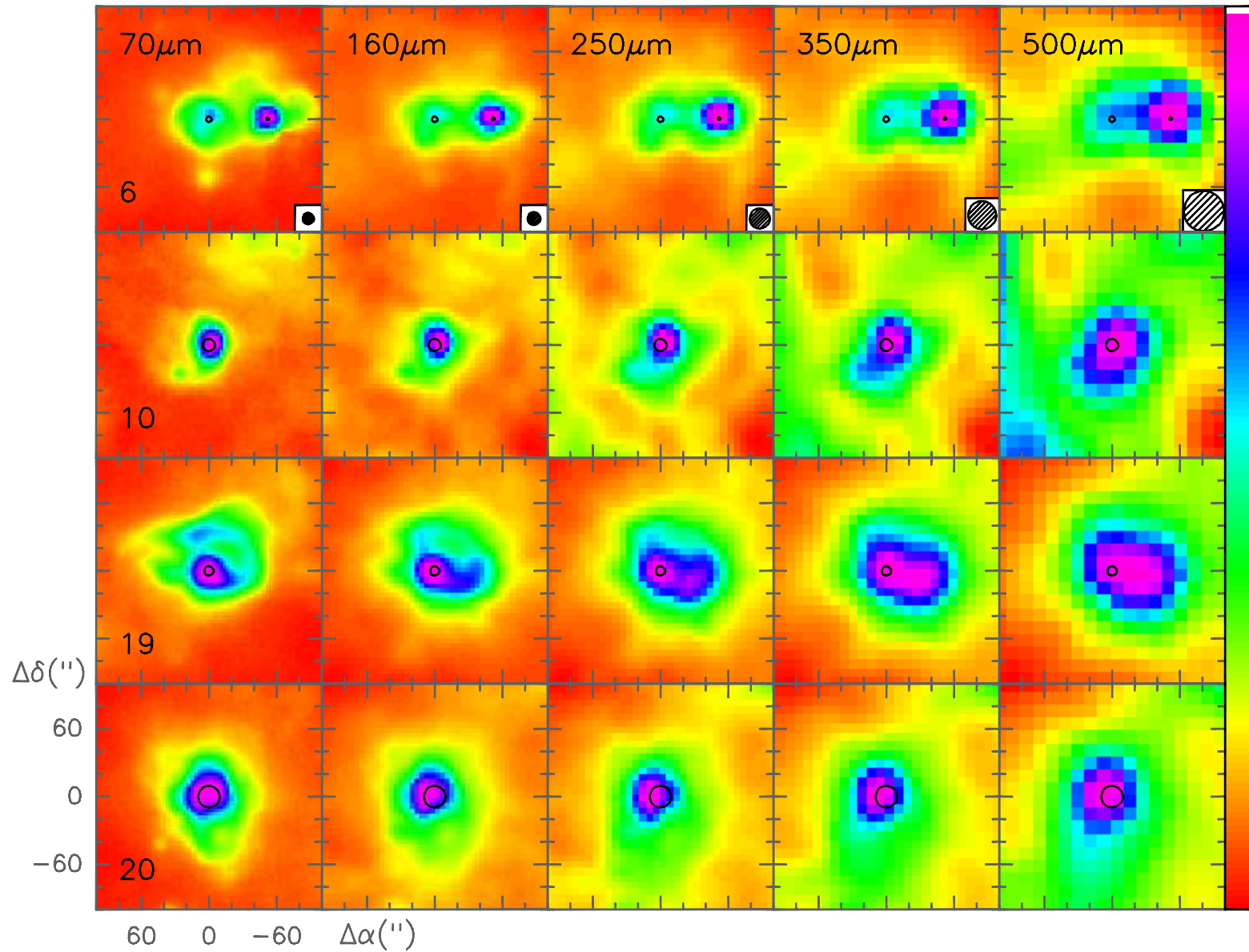


Fig. A.2. Hi-GAL images of the sources lying above the blackbody curve in Fig. 5. The sources are identified by the numbers in Col. 1 of Table A.1. The black circles represent the CORNISH HII regions in the field of view, with diameter equal to the angular size given in Col. 8 of Table 3 in Purcell et al. (2013). The HPBW at each wavelength is shown in the bottom right of the top panels.

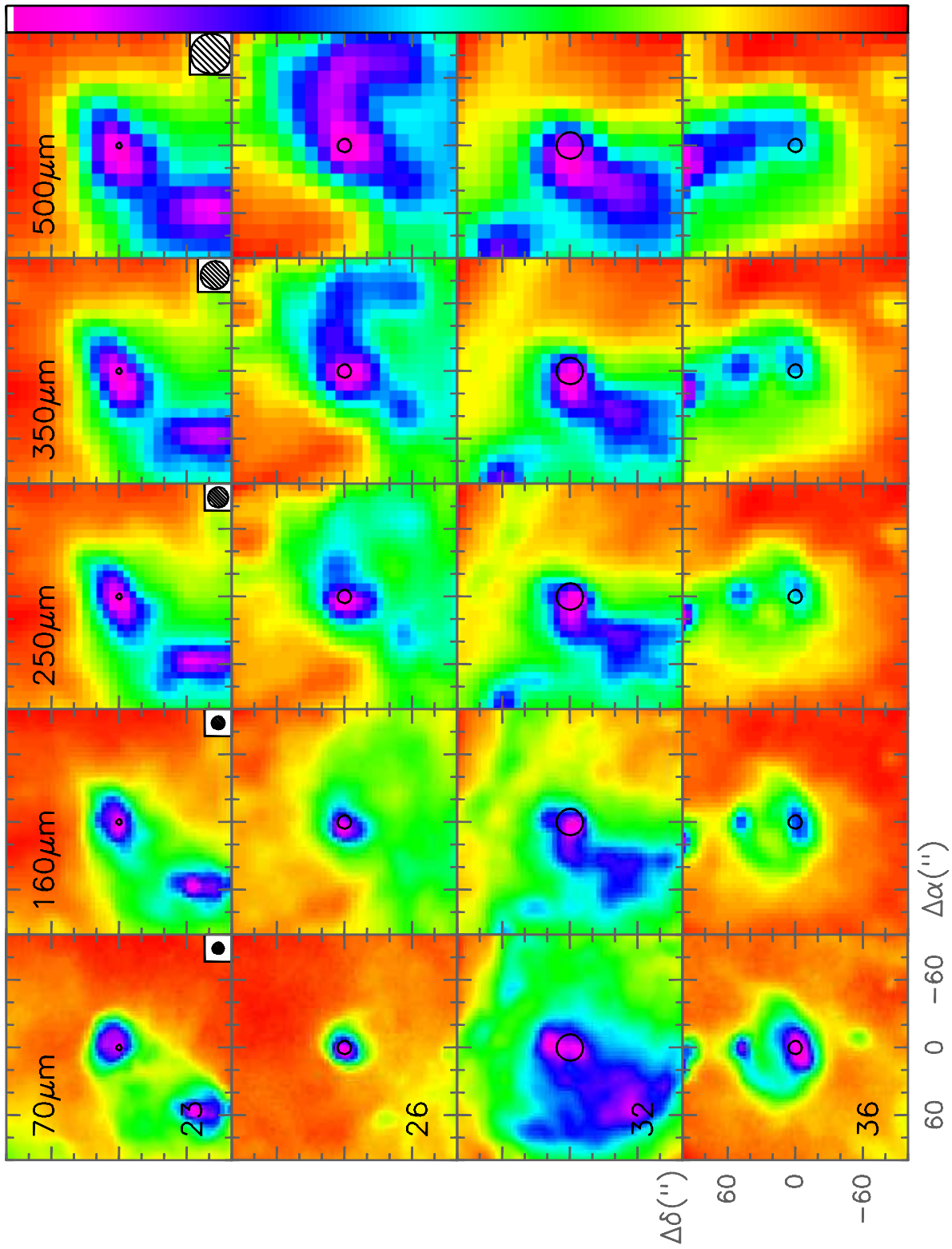


Fig. A.2. continued

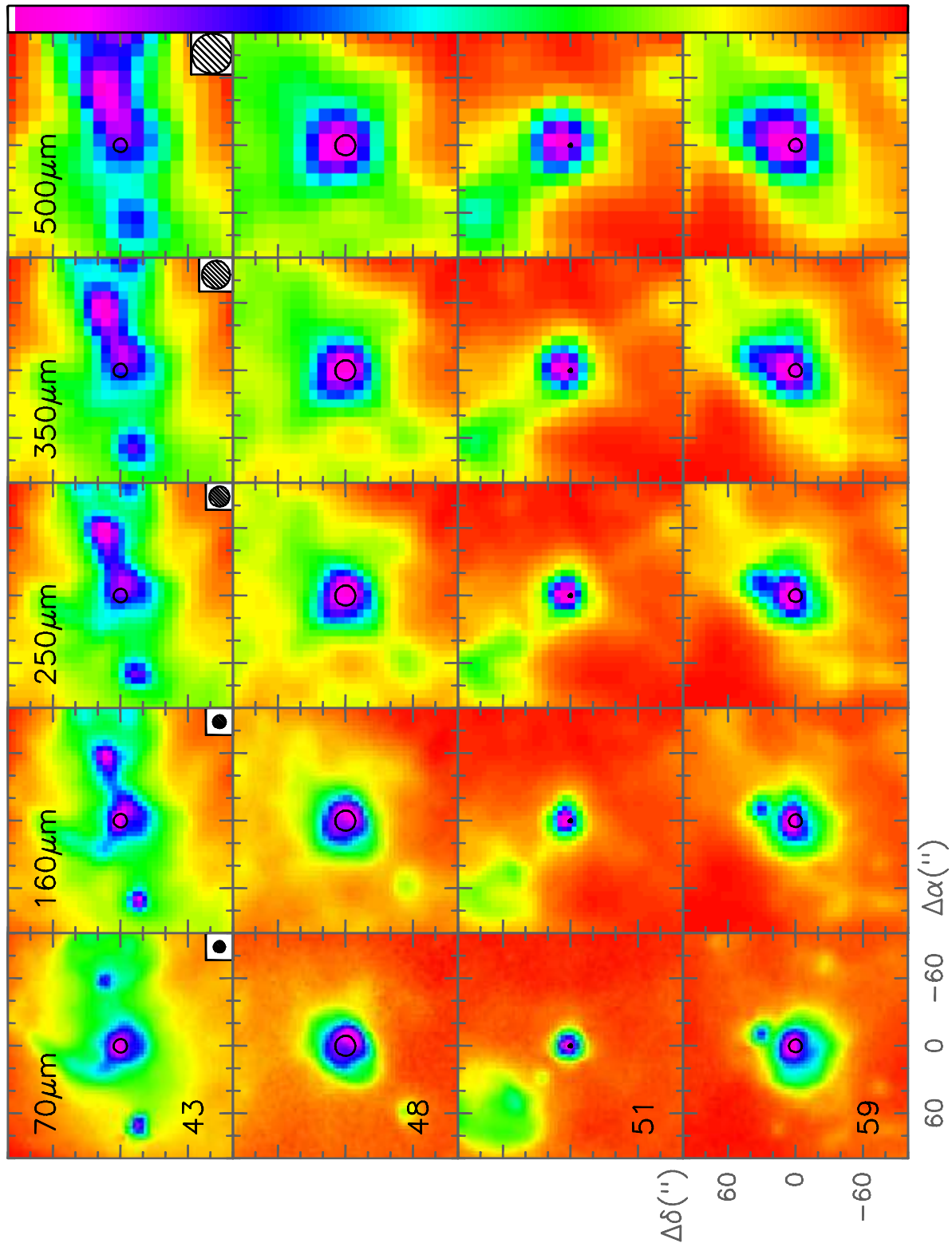


Fig. A.2. continued

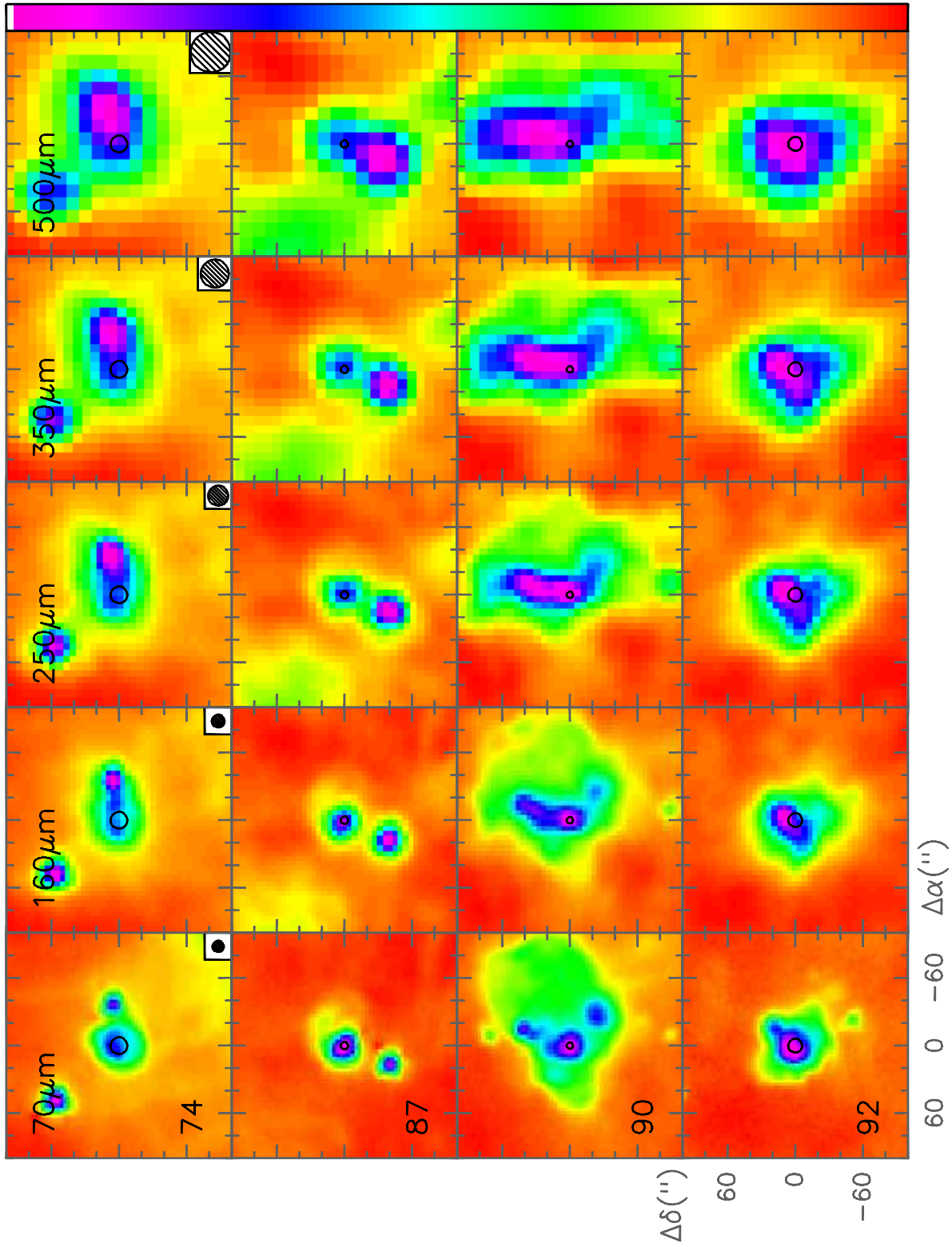


Fig. A.2. continued

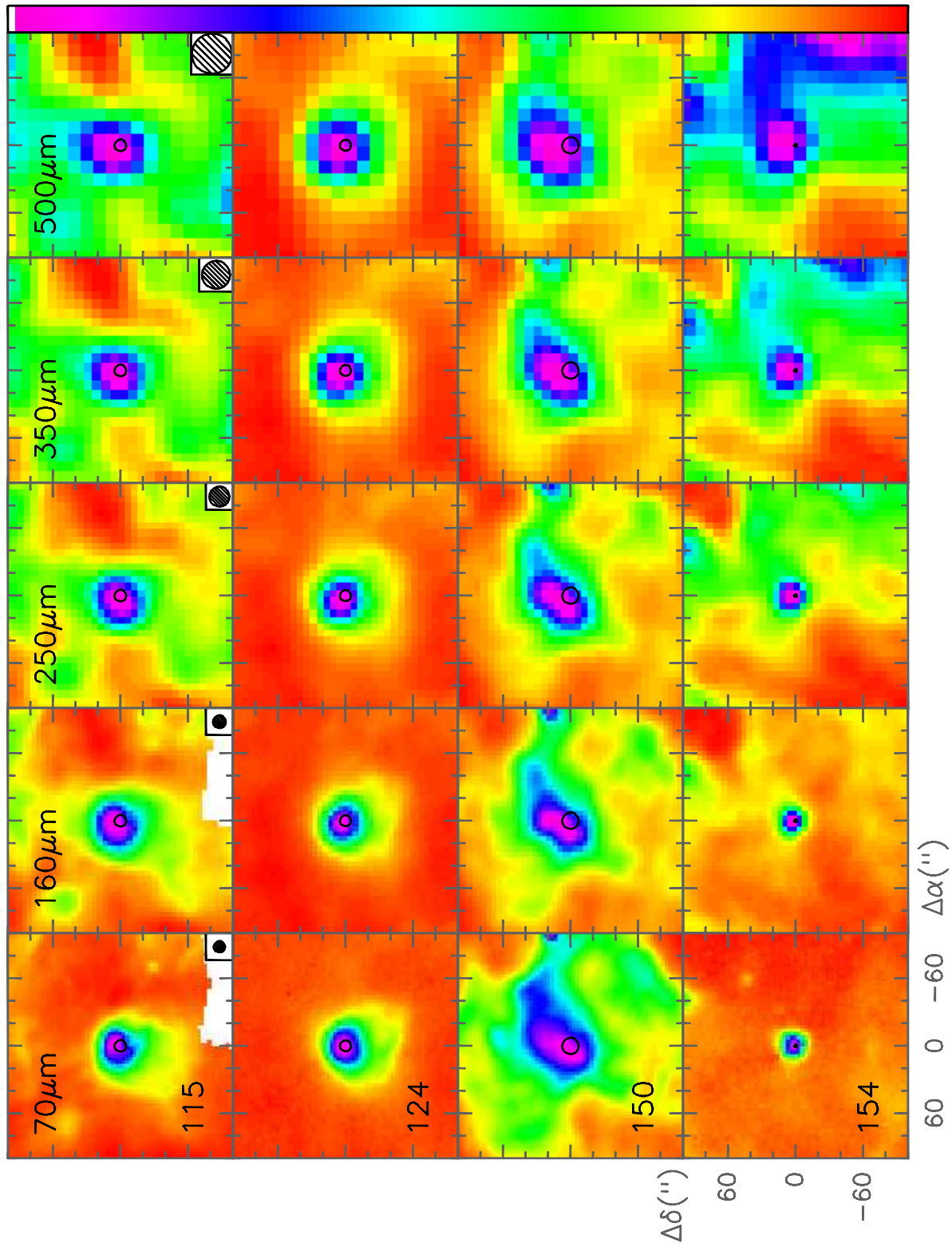


Fig. A.2. continued

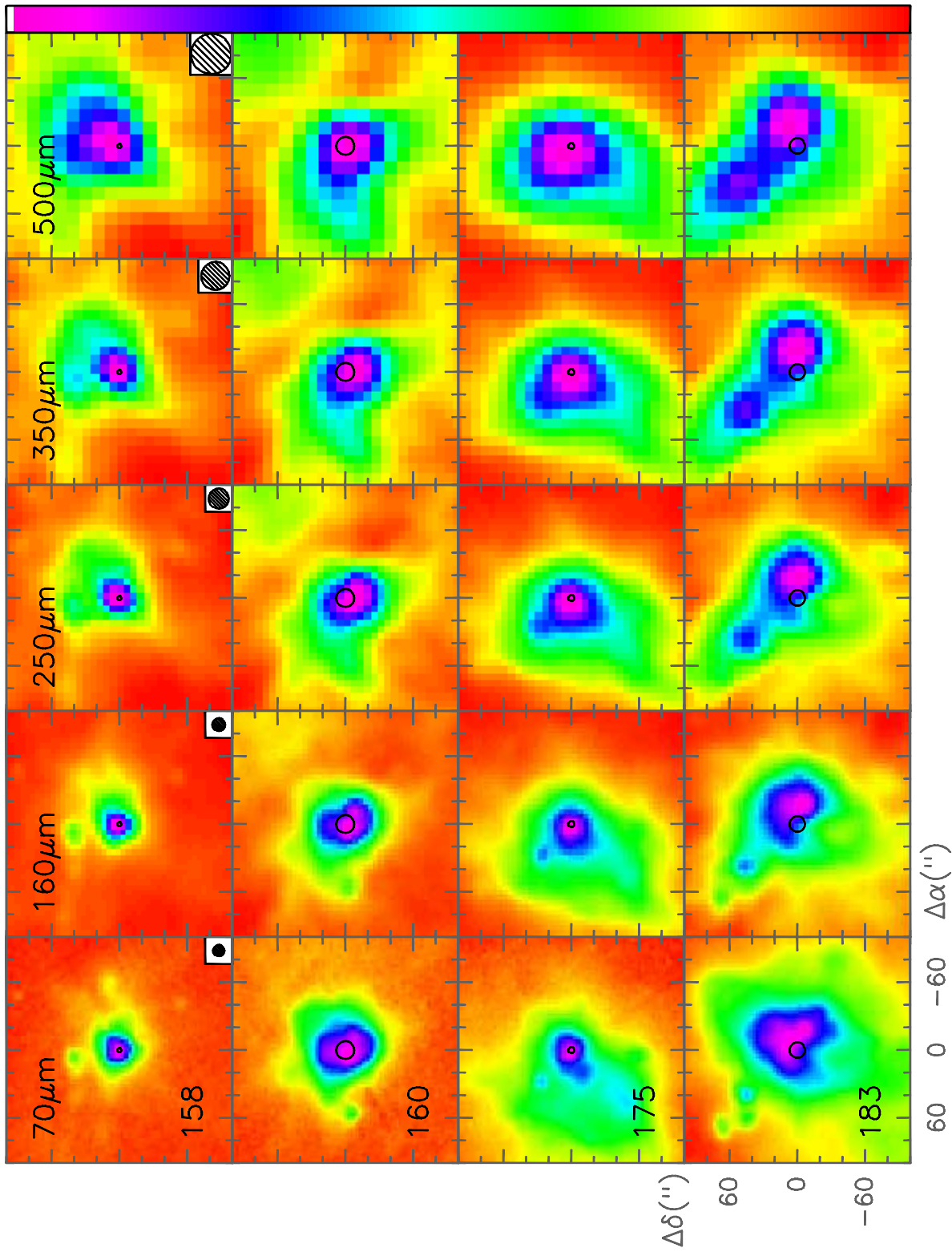


Fig. A.2. continued

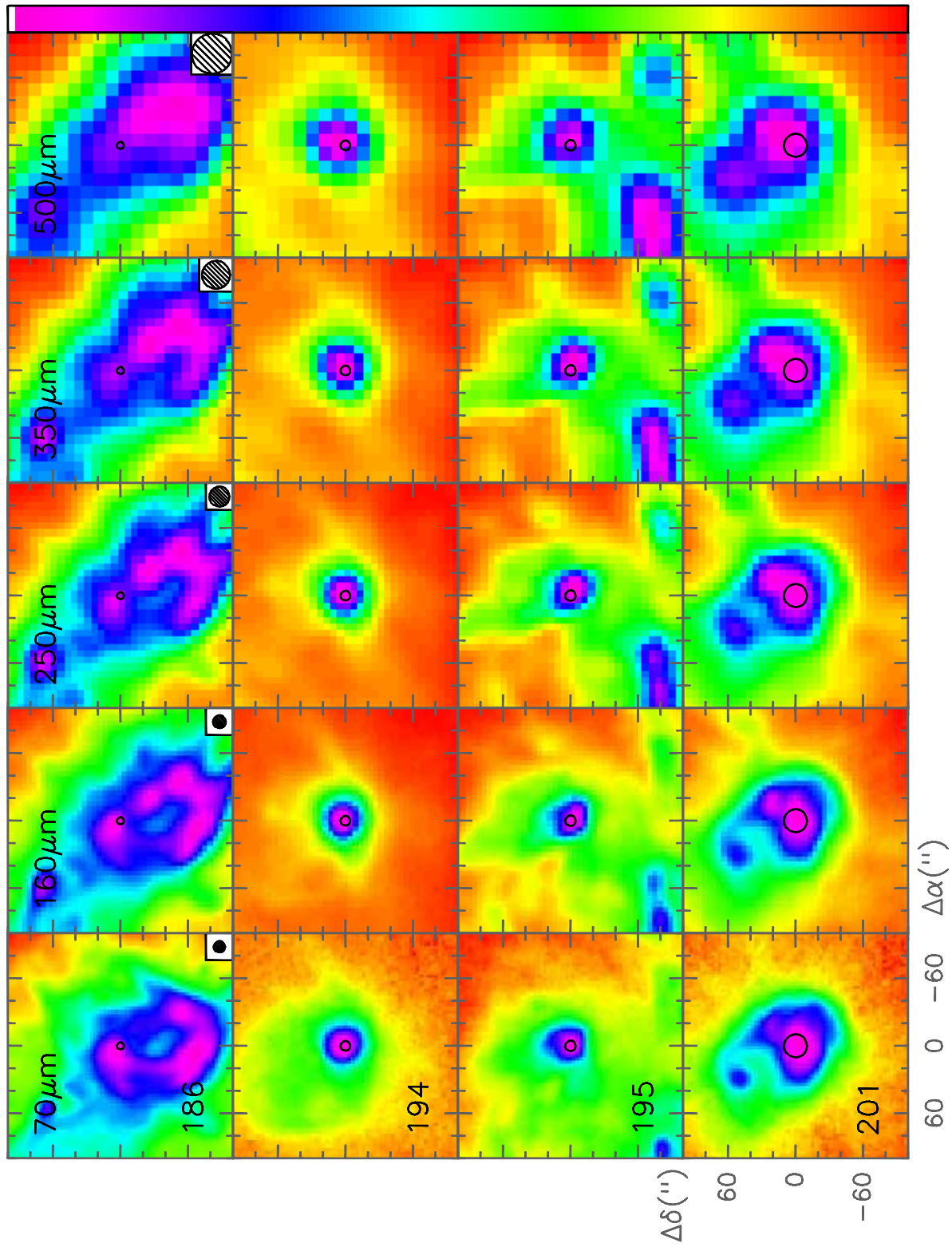


Fig. A.2. continued

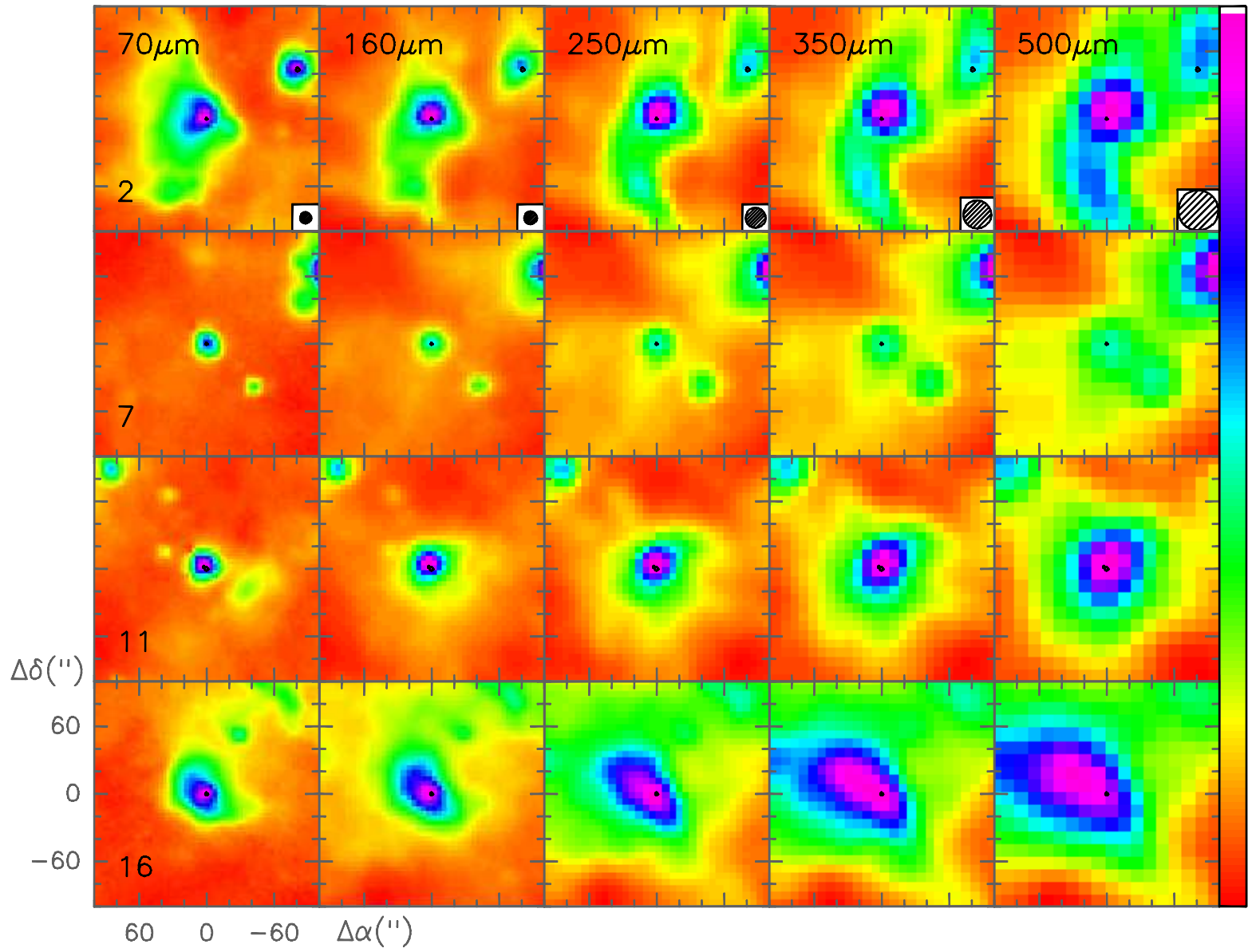


Fig. A.3. Same as Fig. A.2 for the sources lying between the blackbody curve (dashed line) and the single ZAMS star curve (solid line) in Fig. 5.

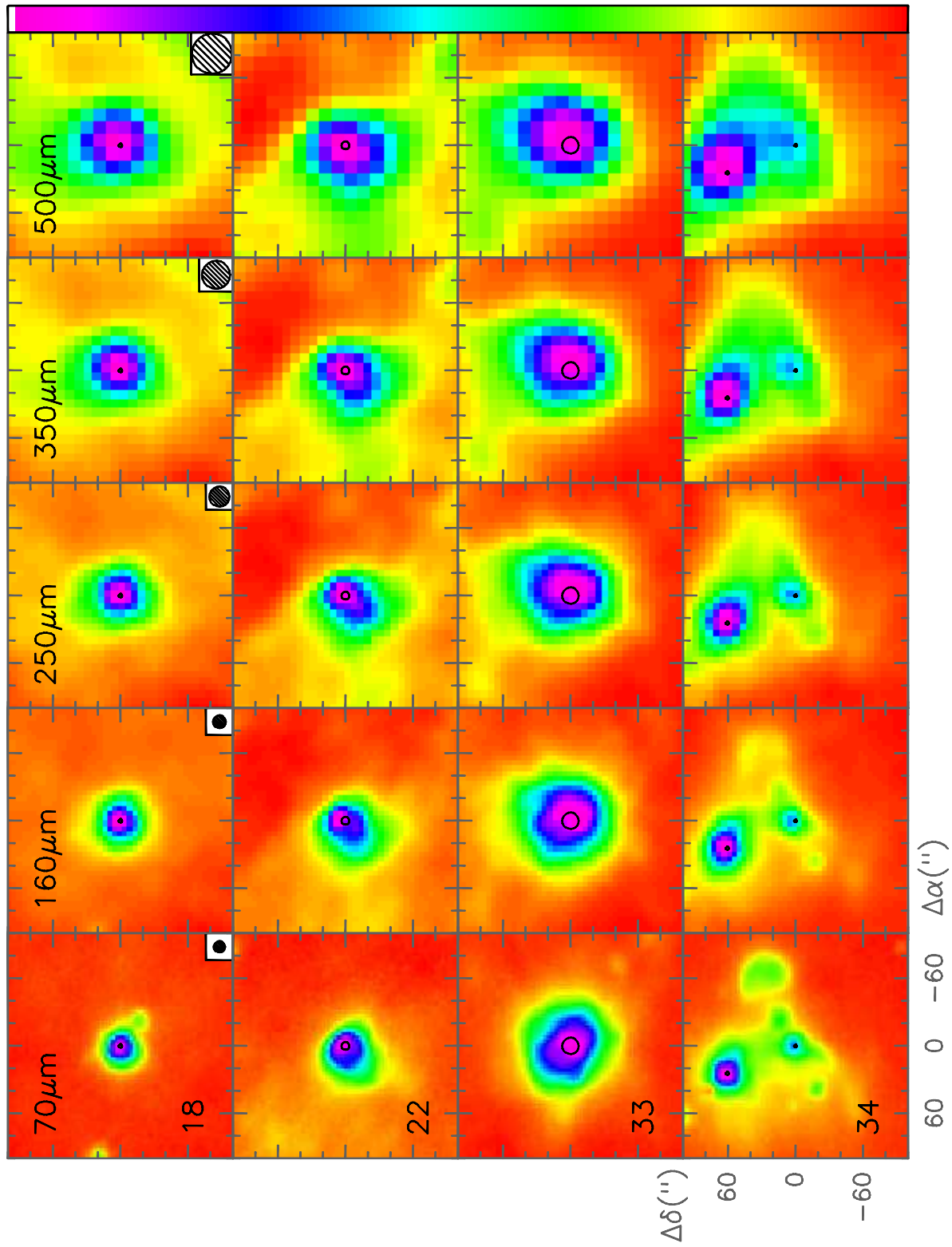


Fig. A.3. continued

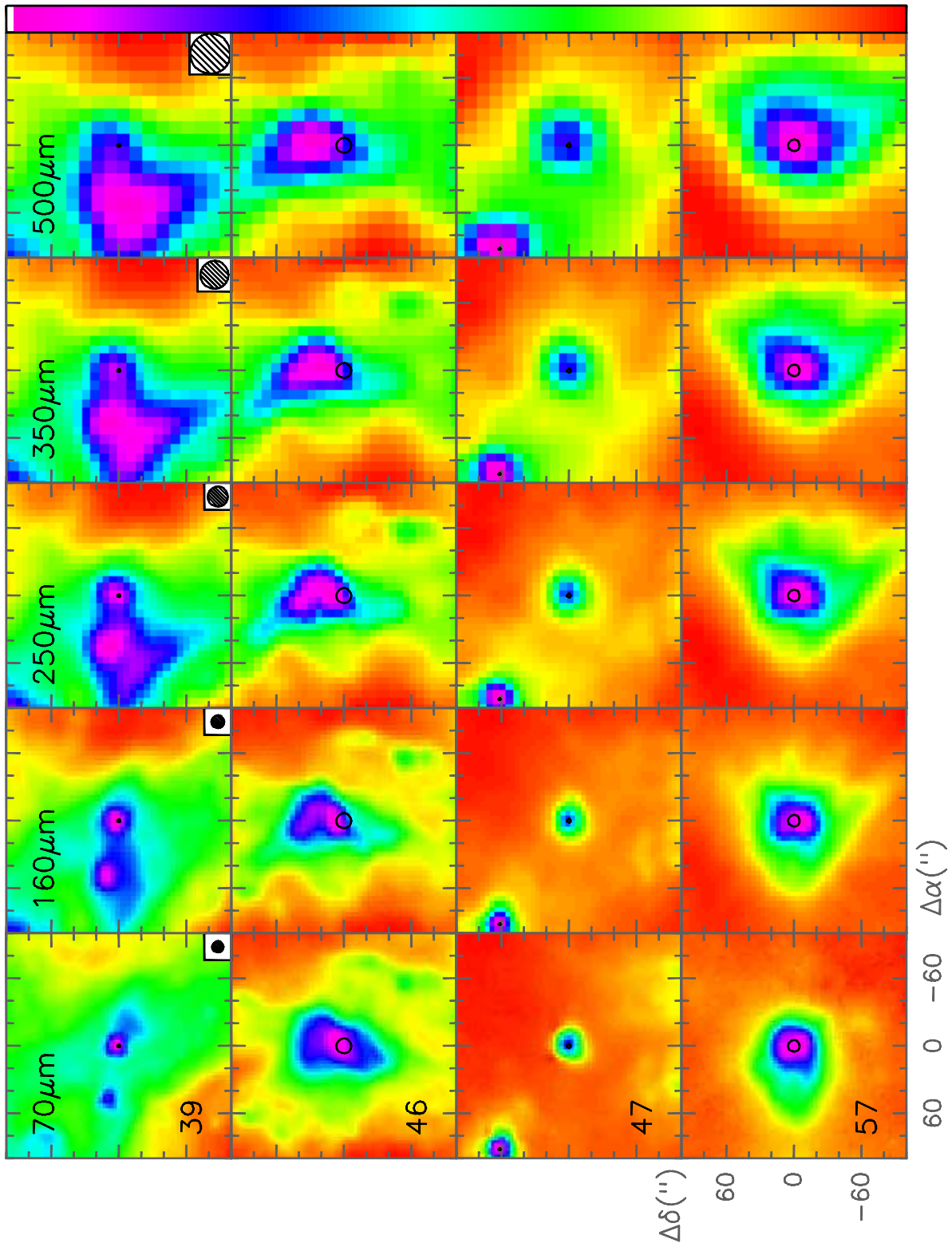


Fig. A.3. continued

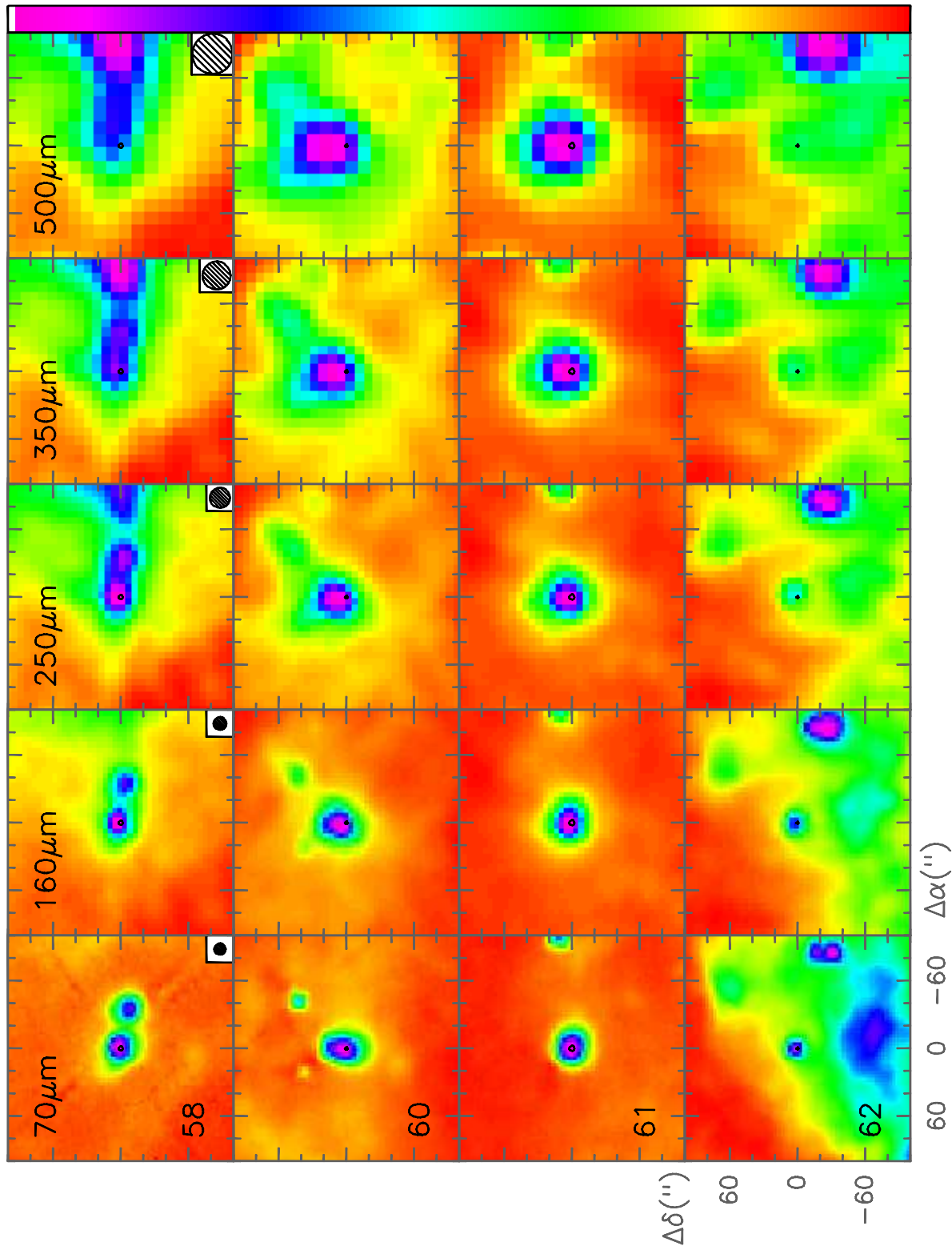


Fig. A.3. continued

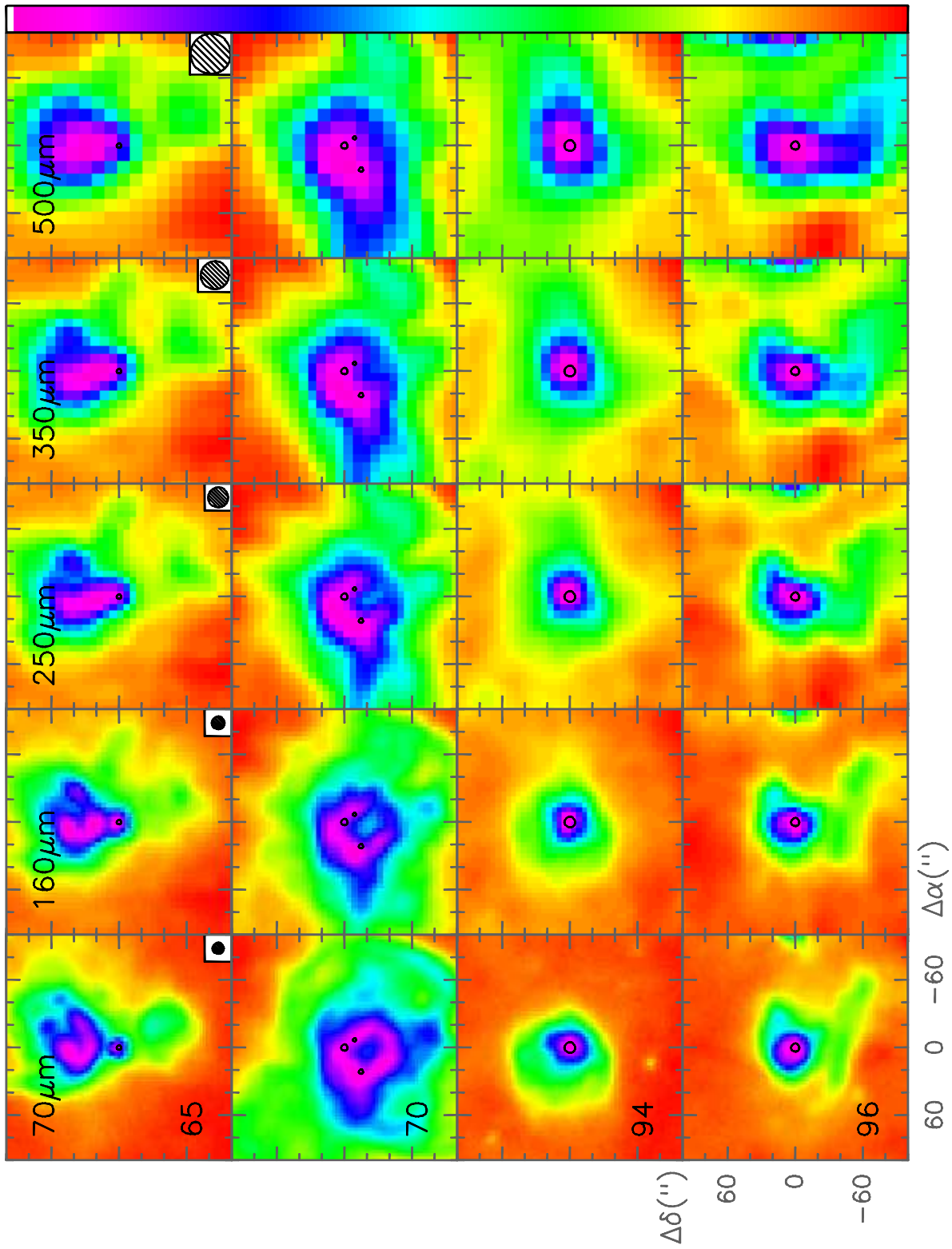


Fig. A.3. continued

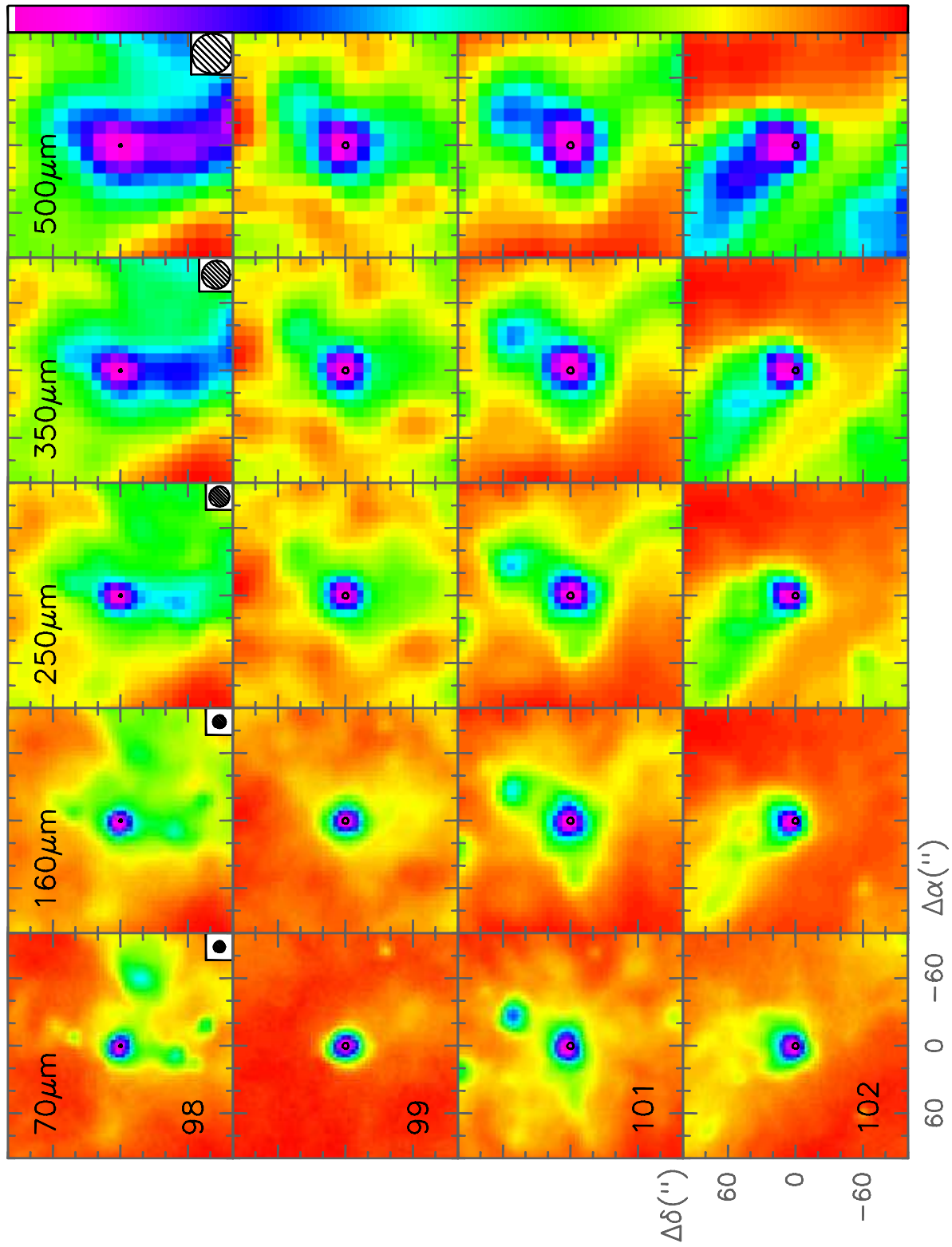


Fig. A.3. continued

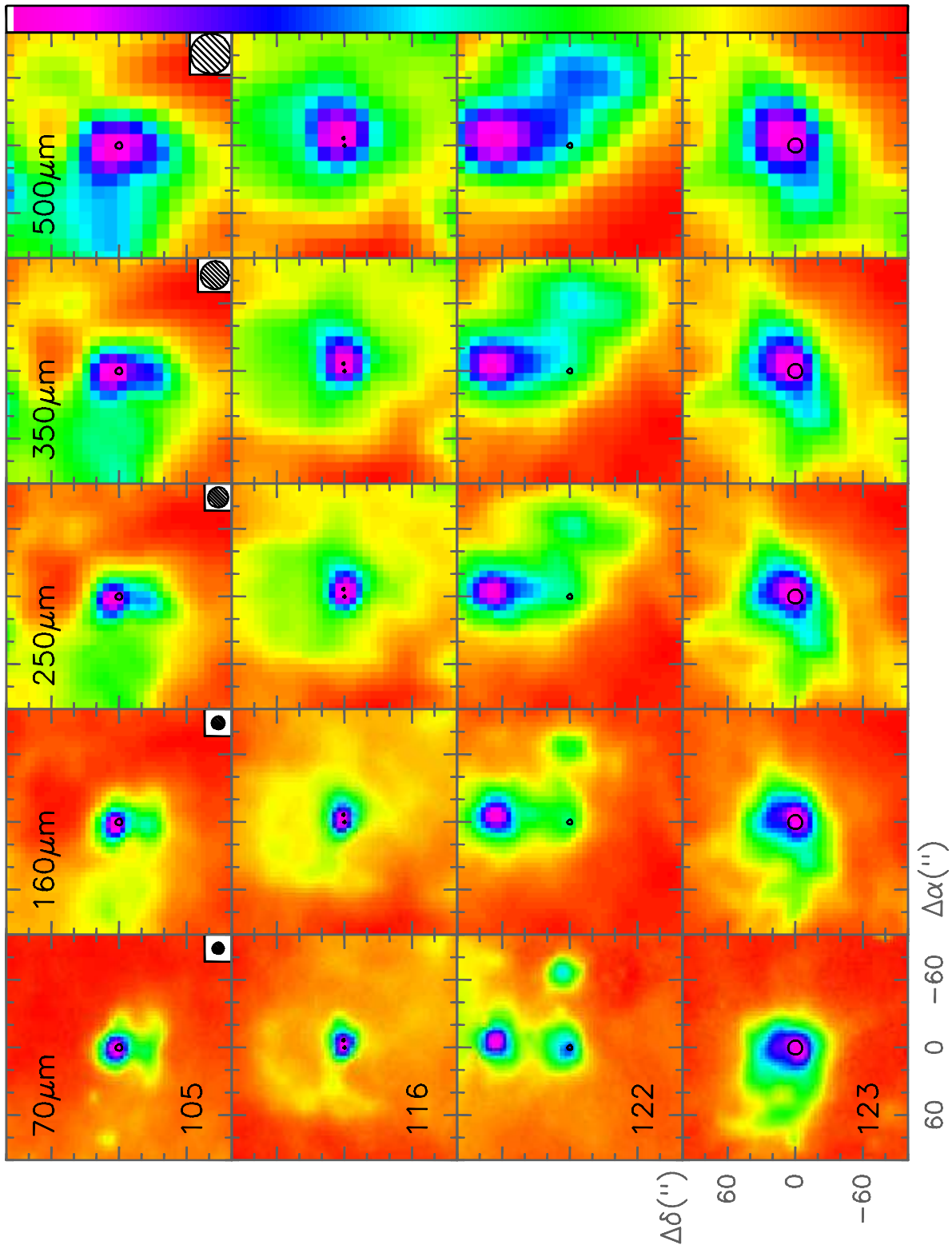


Fig. A.3. continued

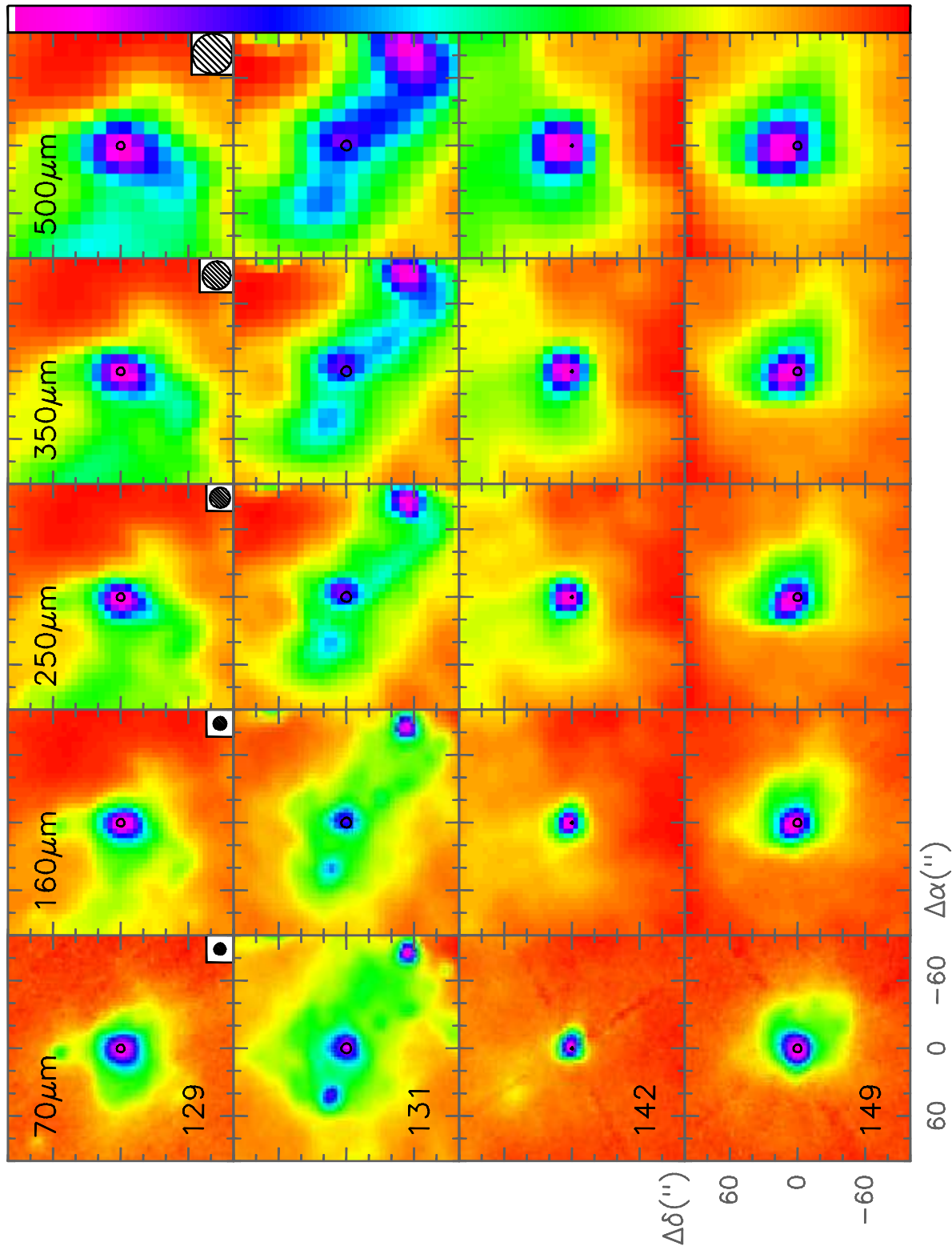


Fig. A.3. continued

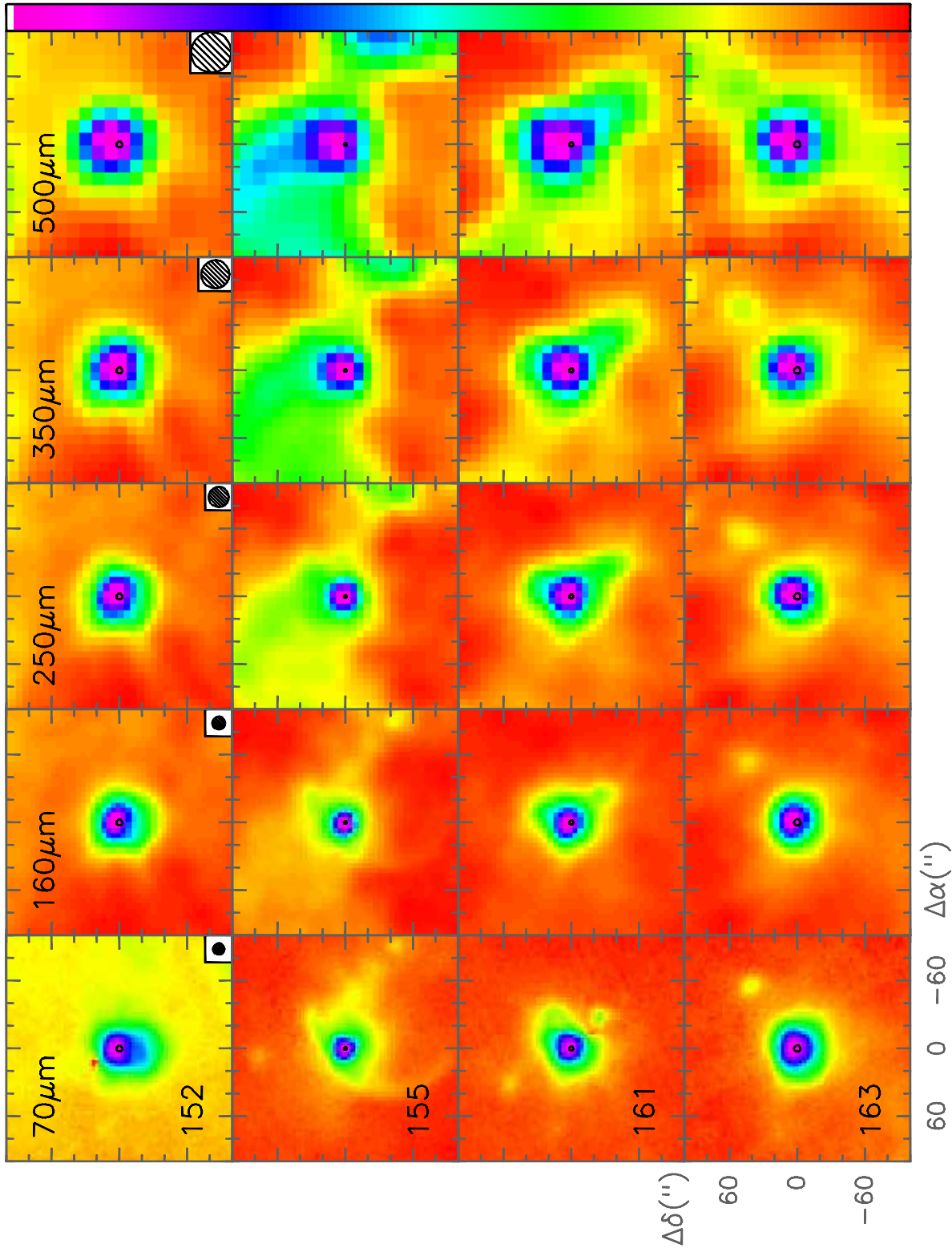


Fig. A.3. continued

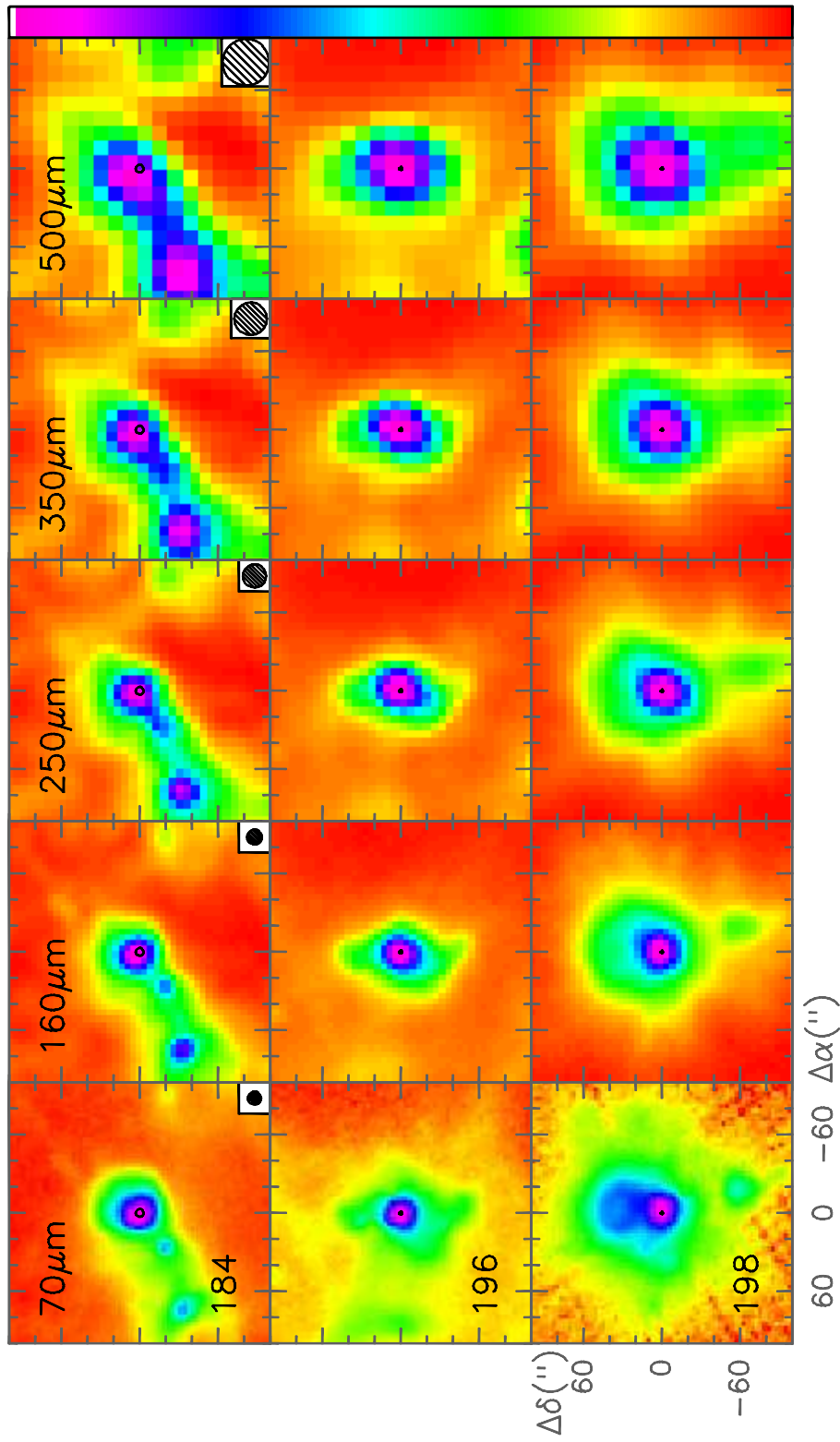


Fig.A.3. continued

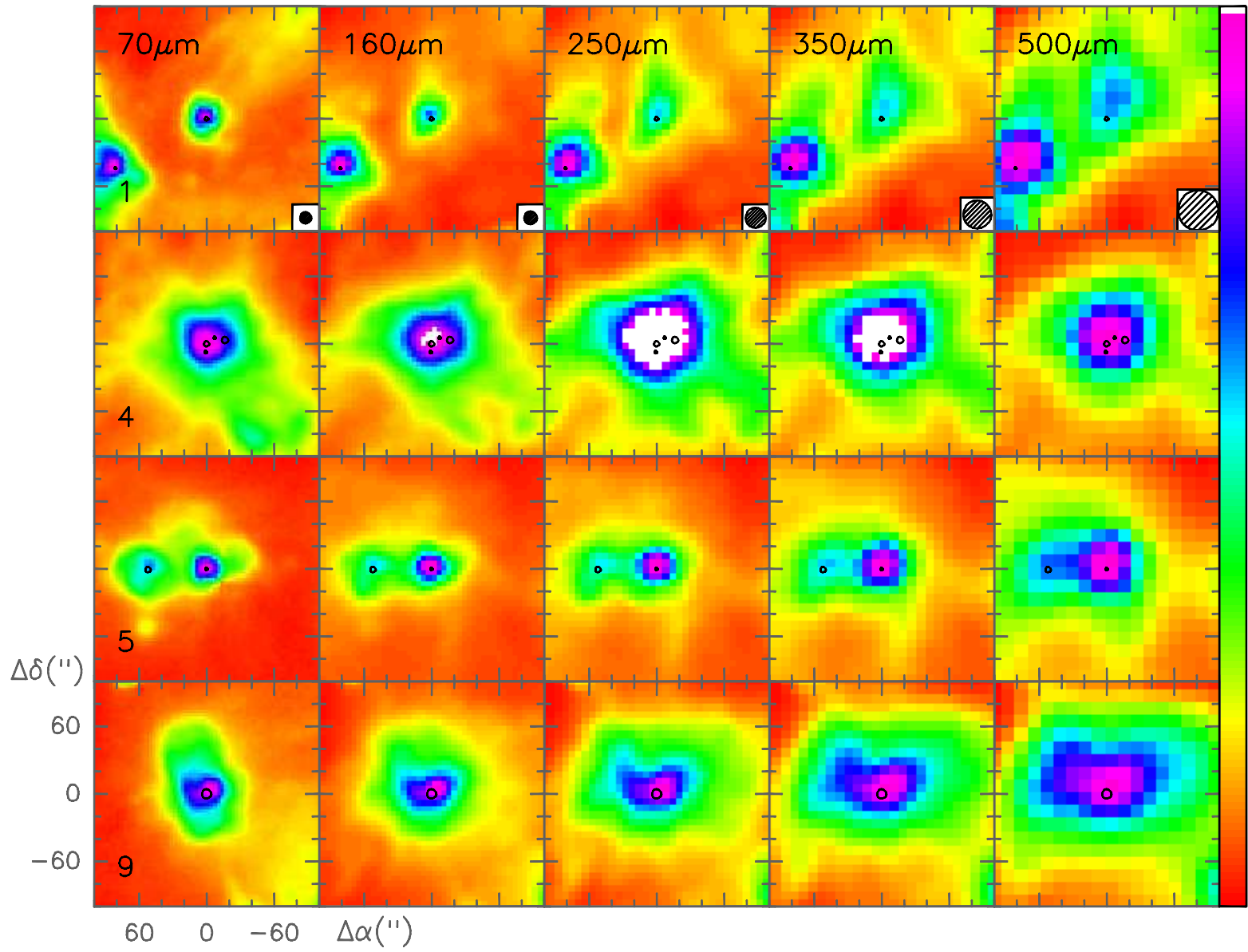


Fig. A.4. Same as Fig. A.2 for the sources lying inside the cluster region (hatched area) in Fig. 5.

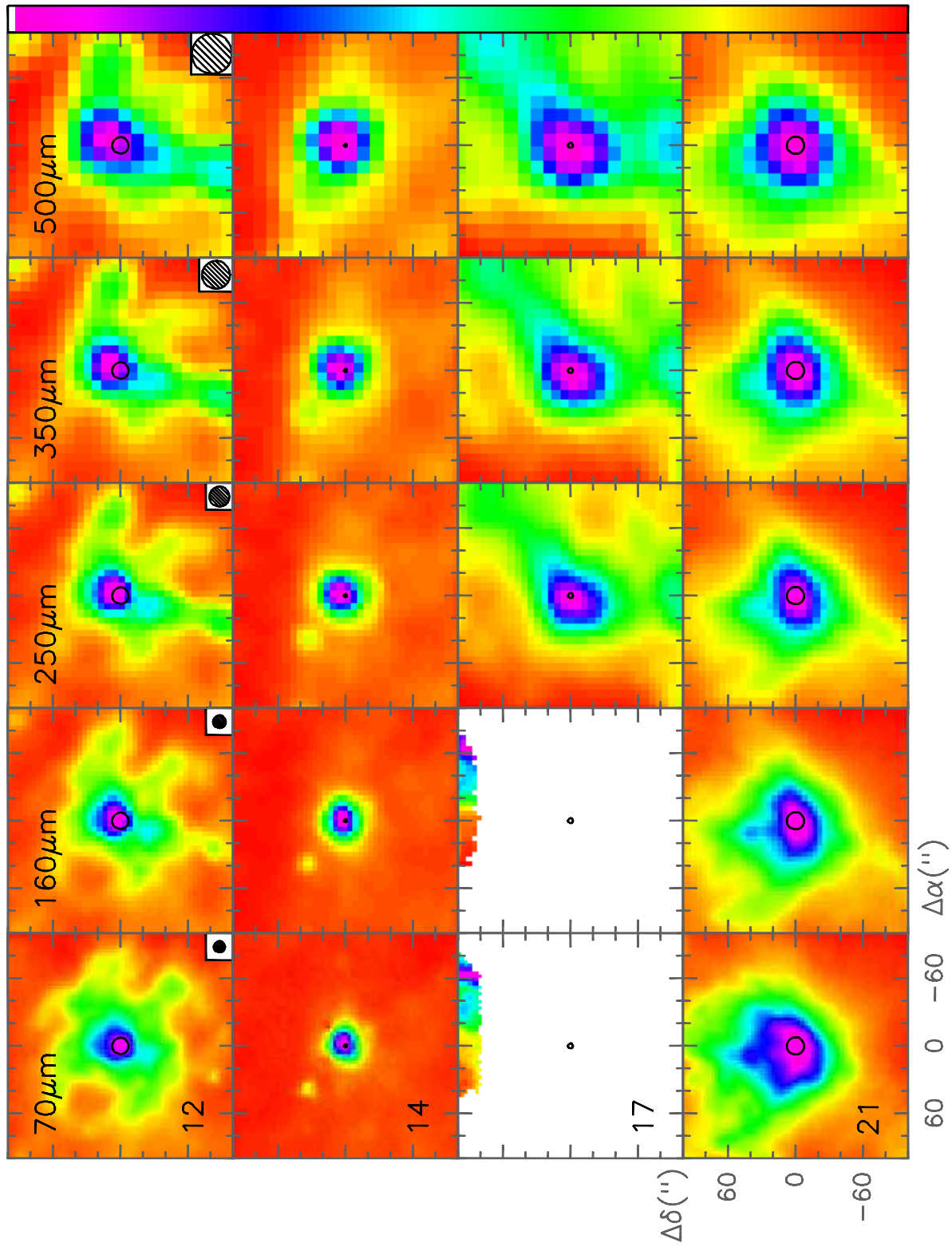


Fig. A.4. continued

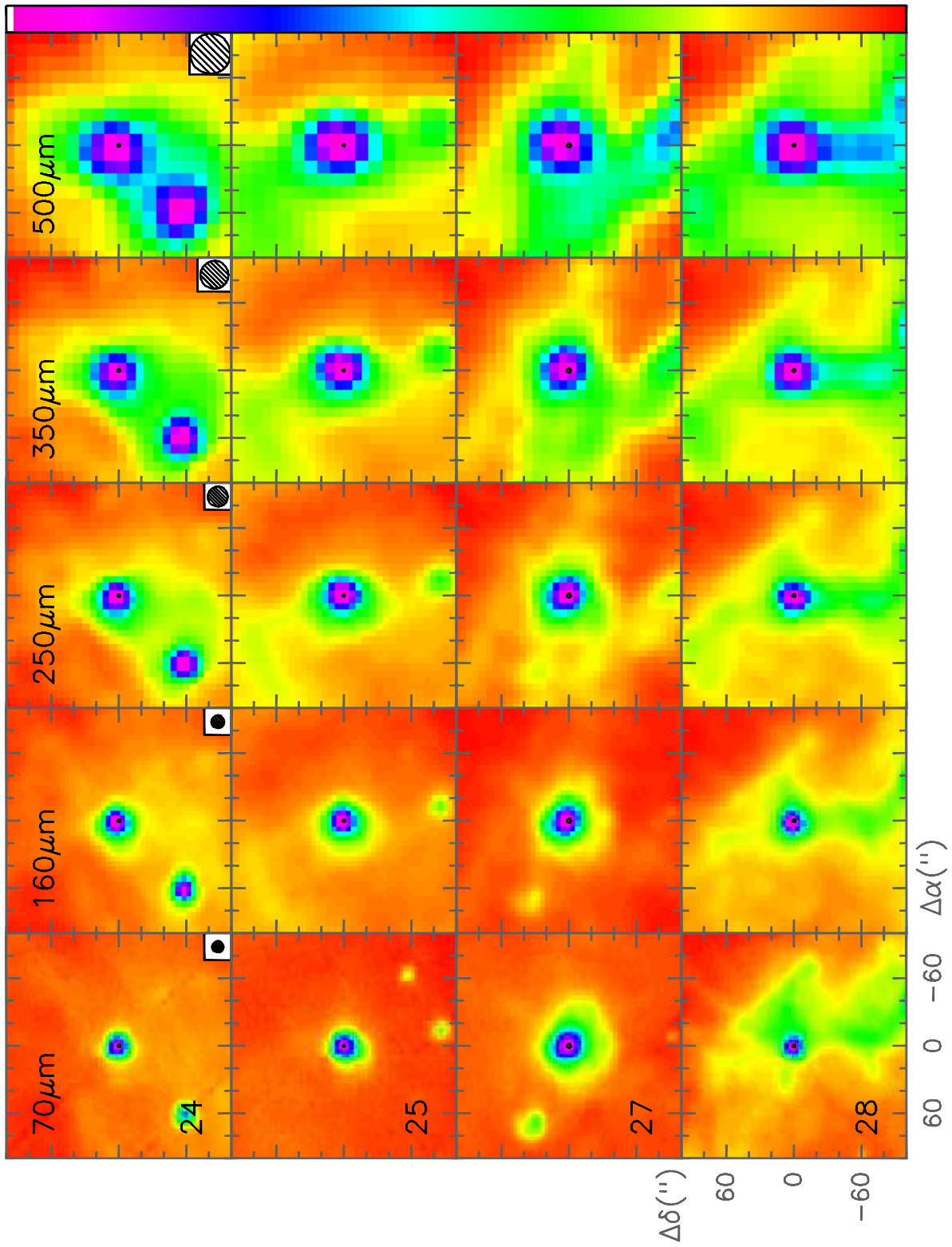


Fig. A.4. continued

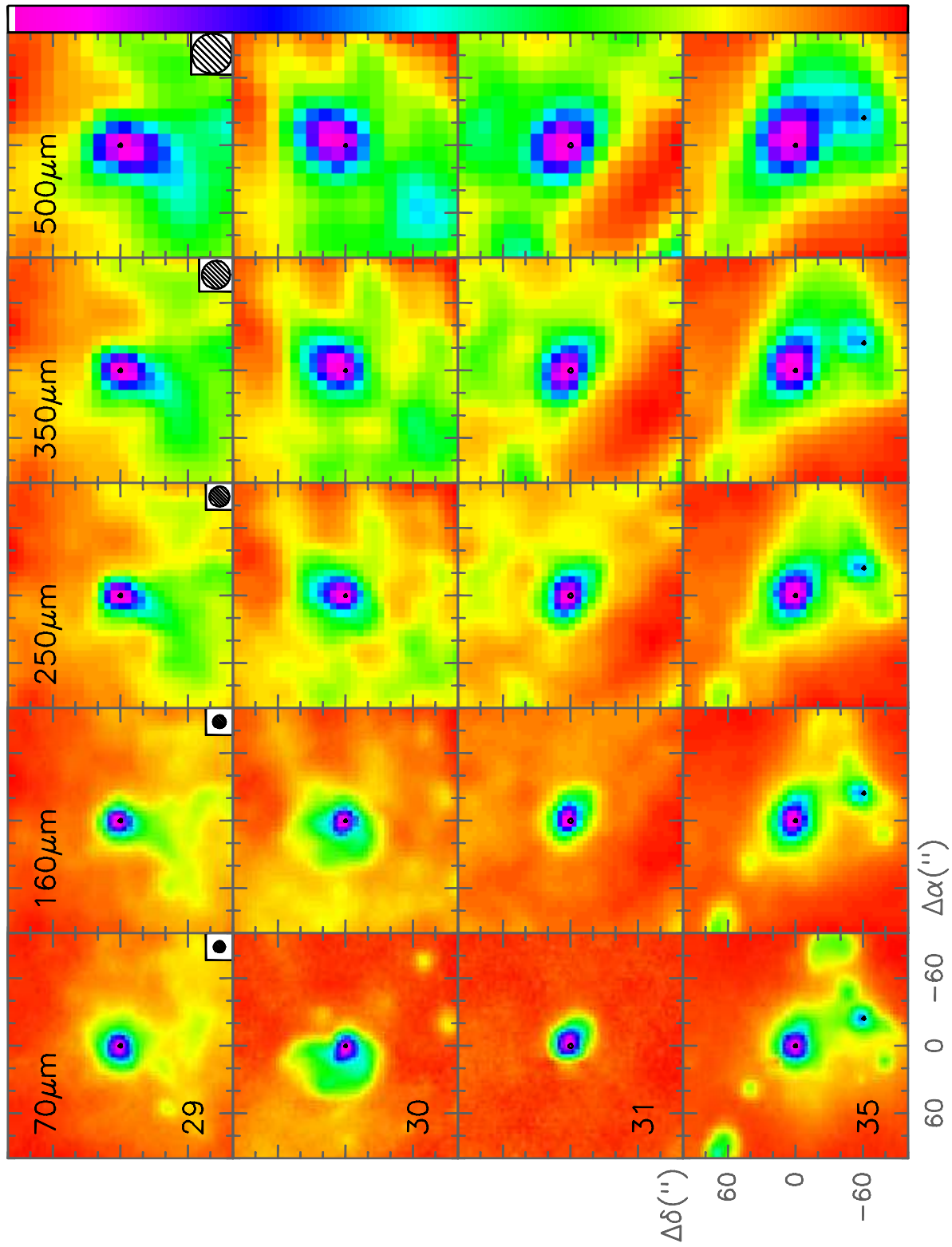


Fig. A.4. continued

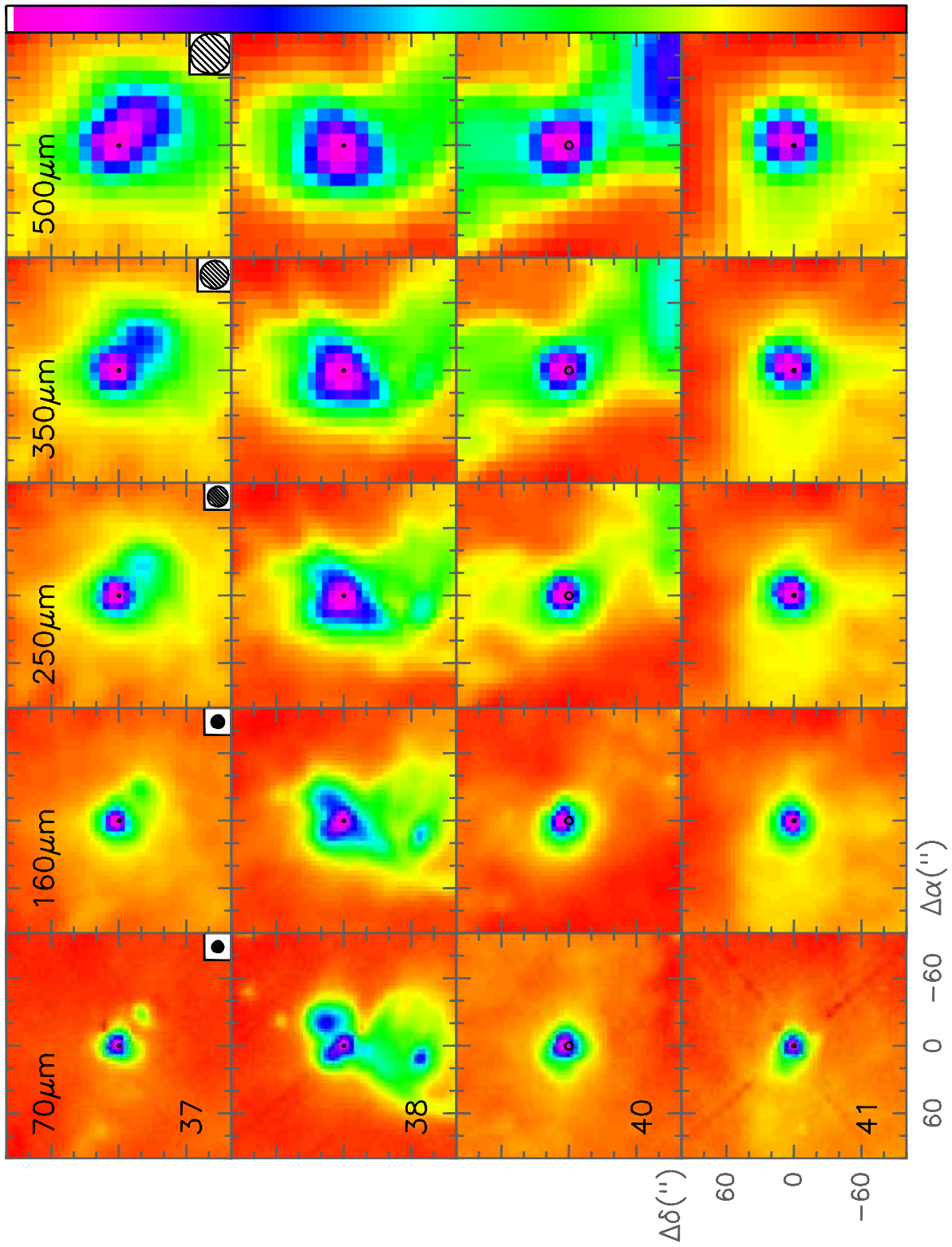


Fig. A.4. continued

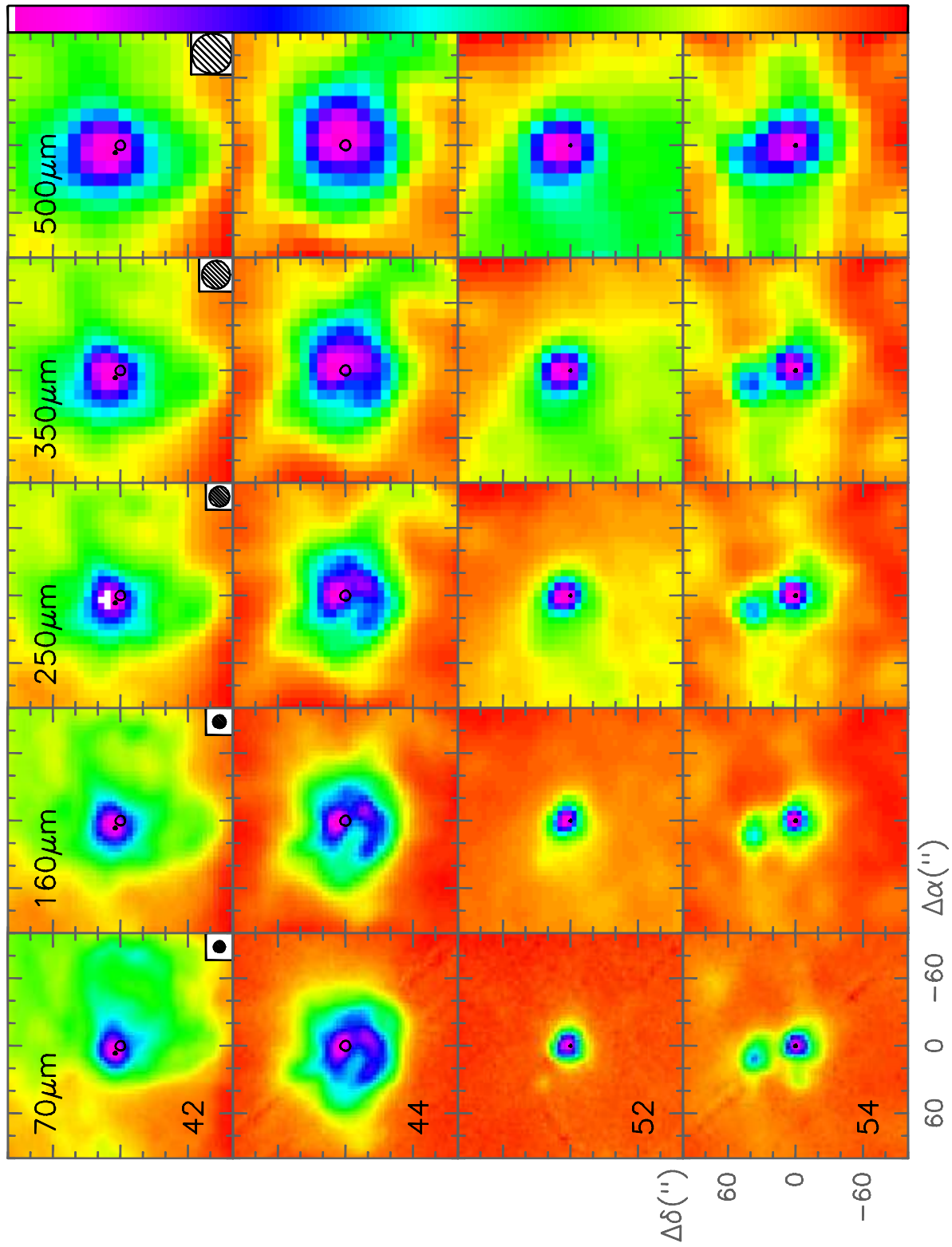


Fig. A.4. continued

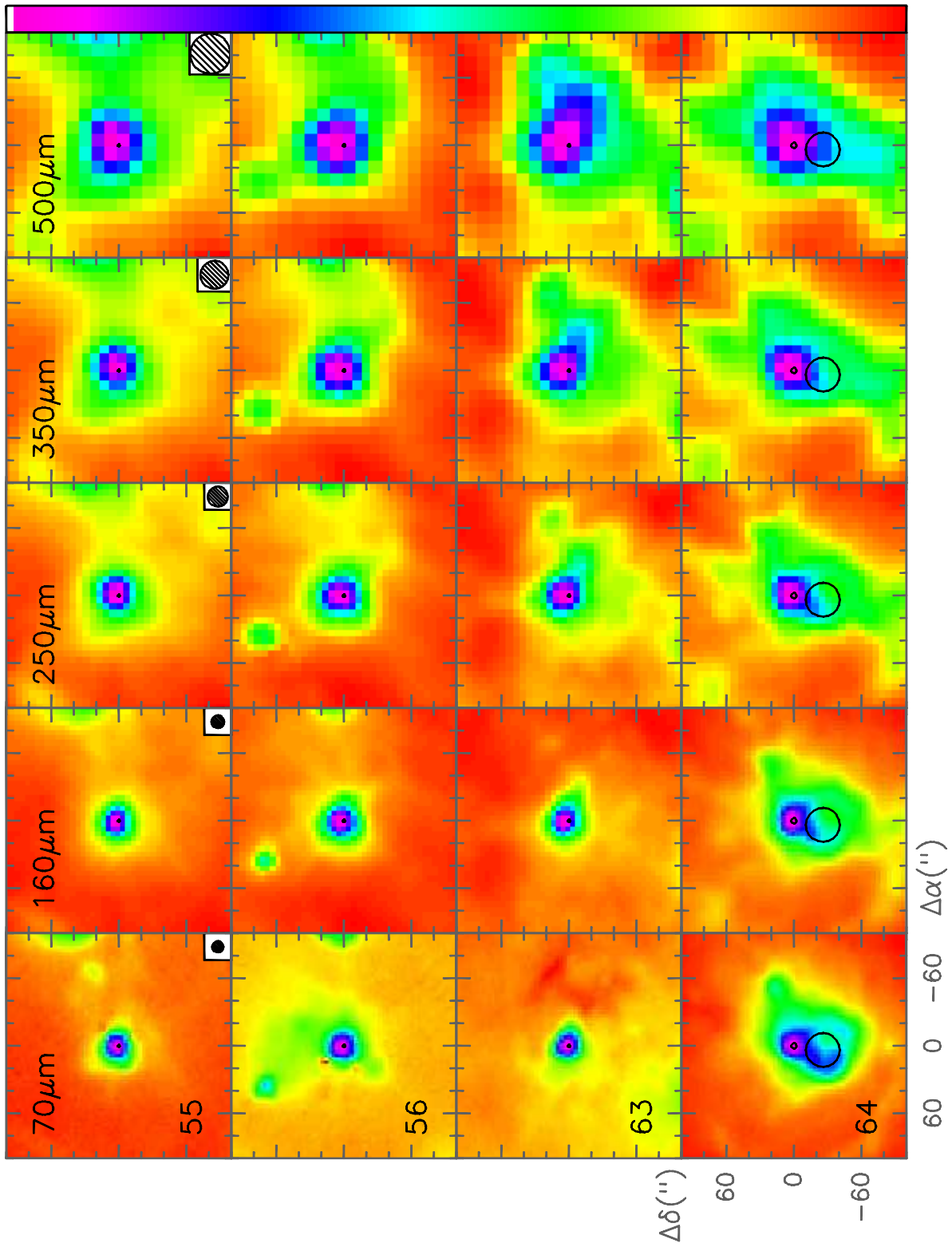


Fig. A.4. continued

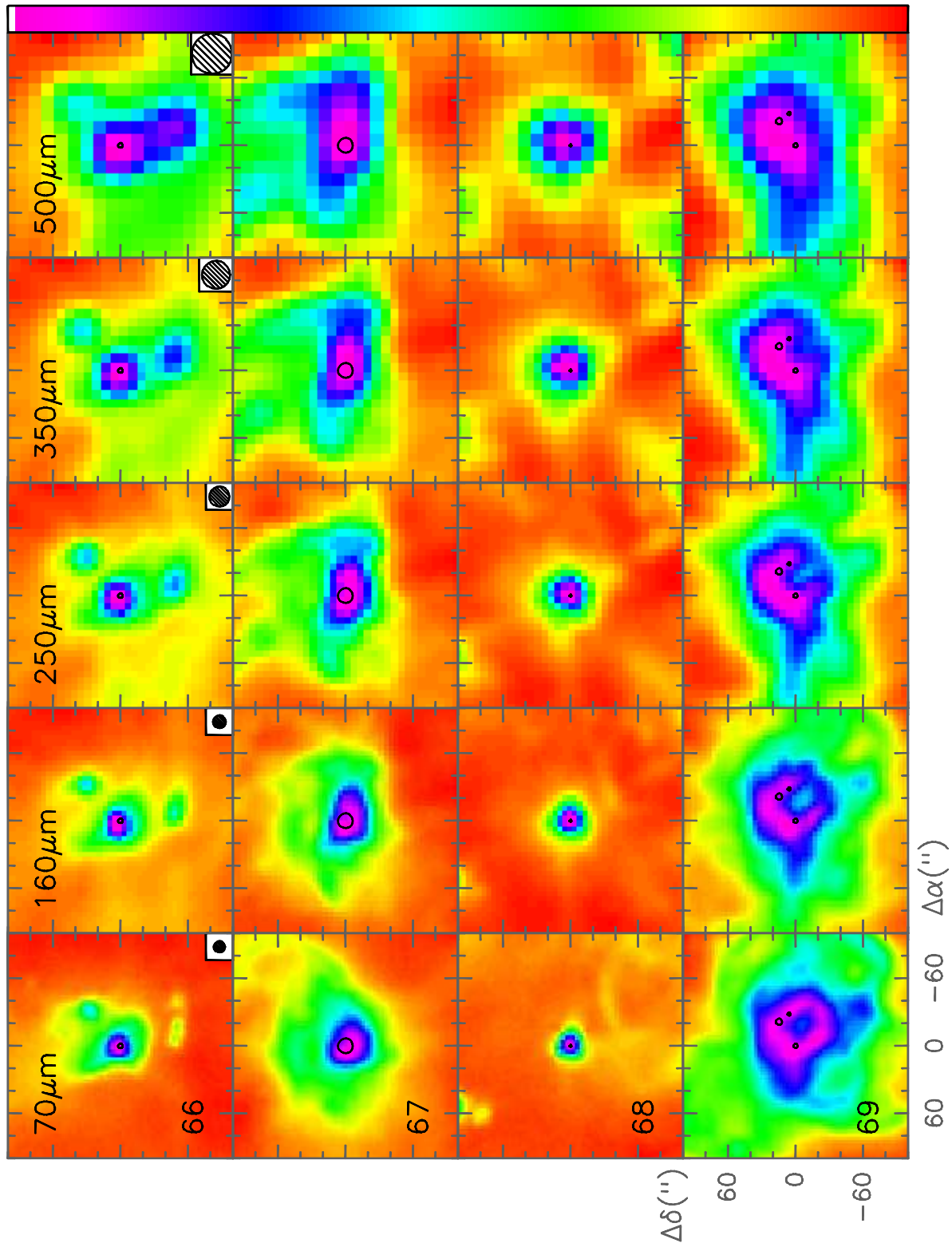


Fig. A.4. continued

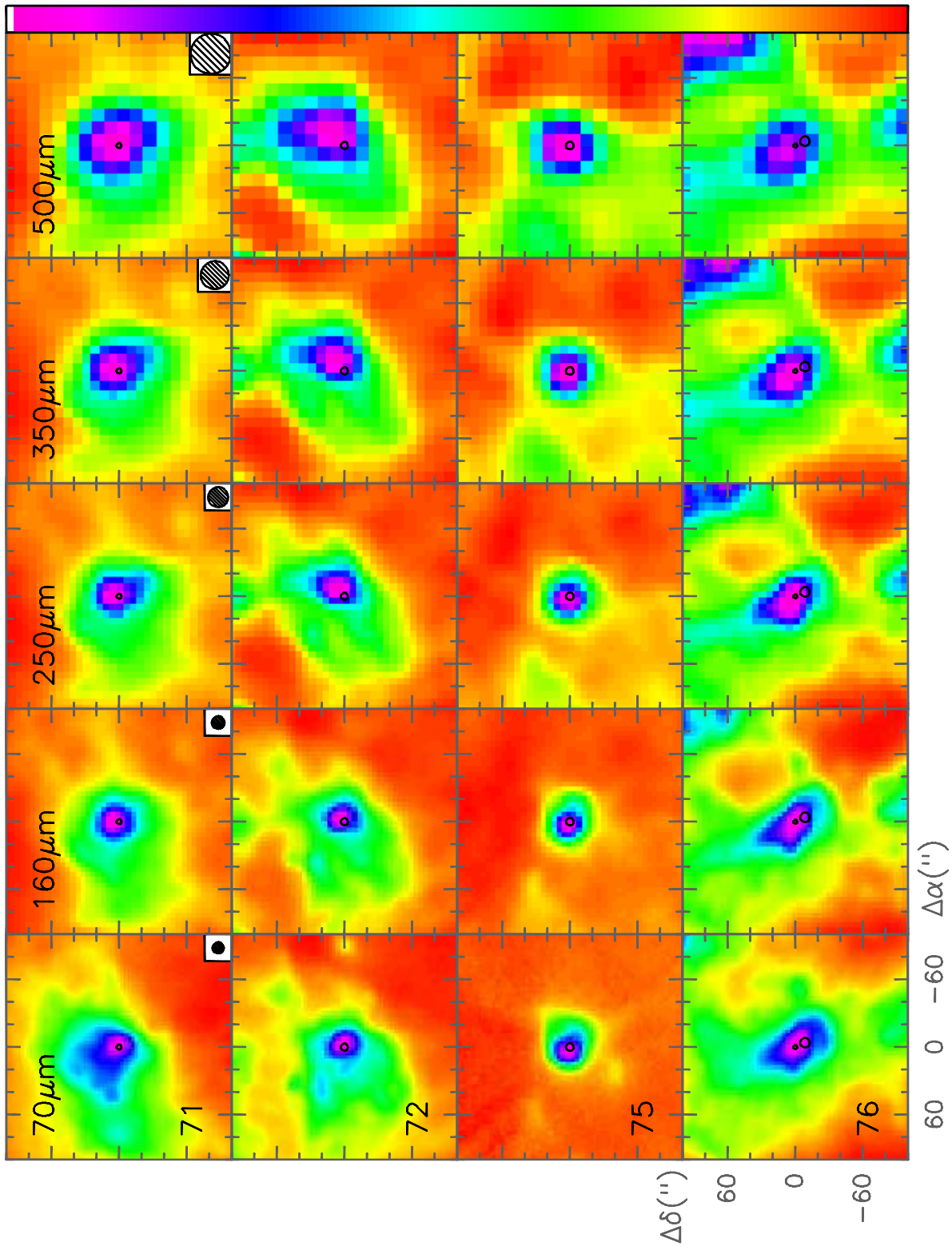


Fig. A.4. continued

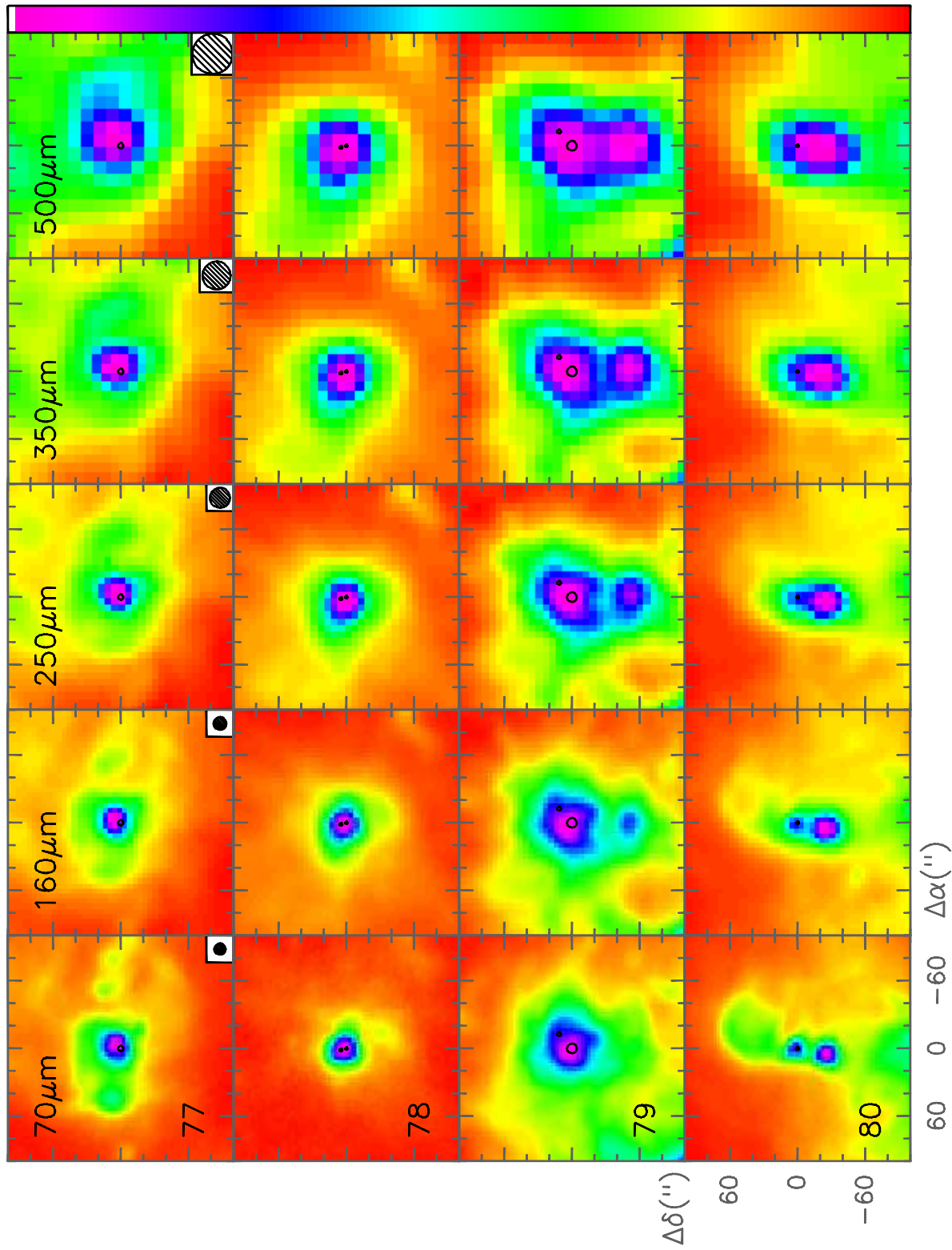


Fig. A.4. continued

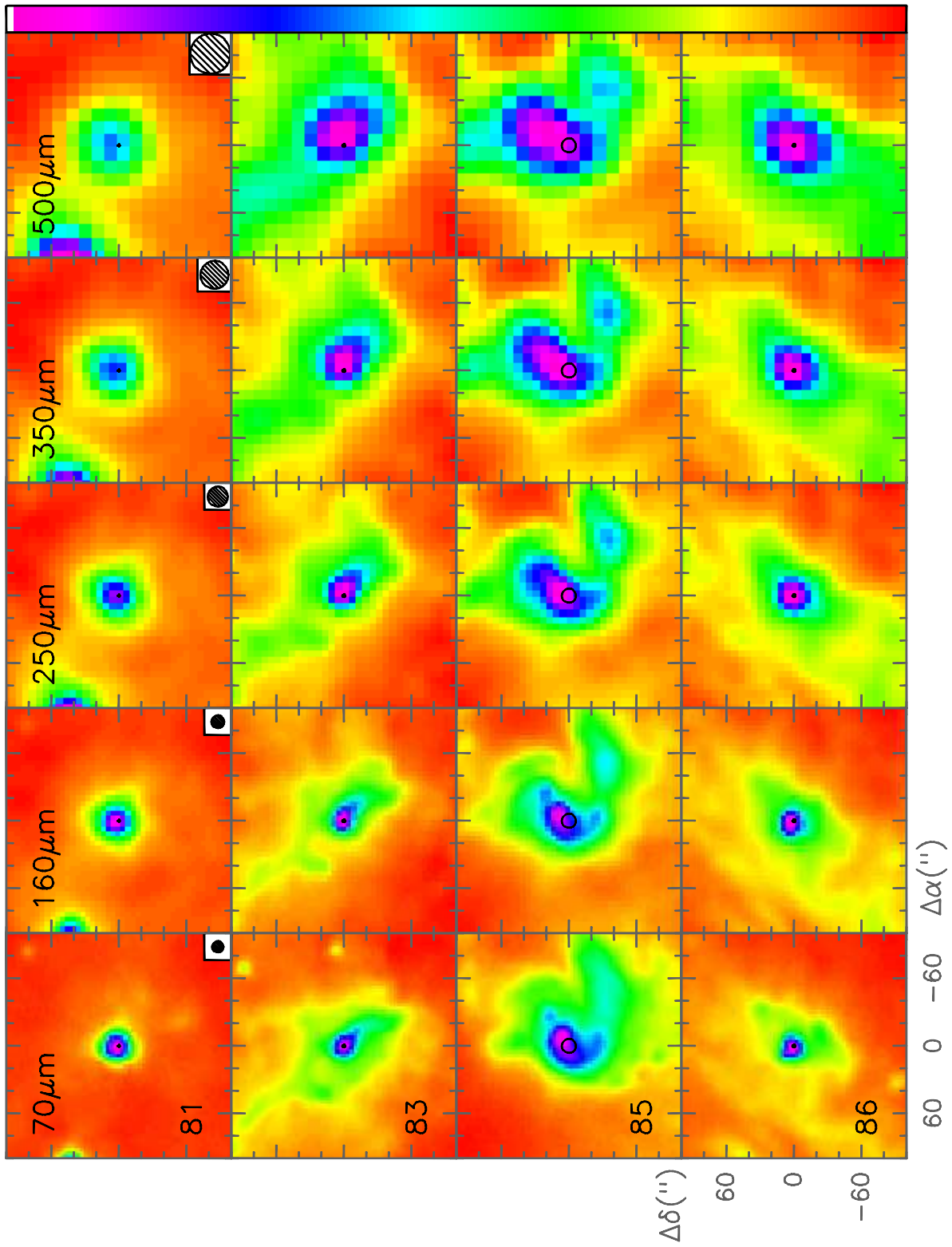


Fig. A.4. continued

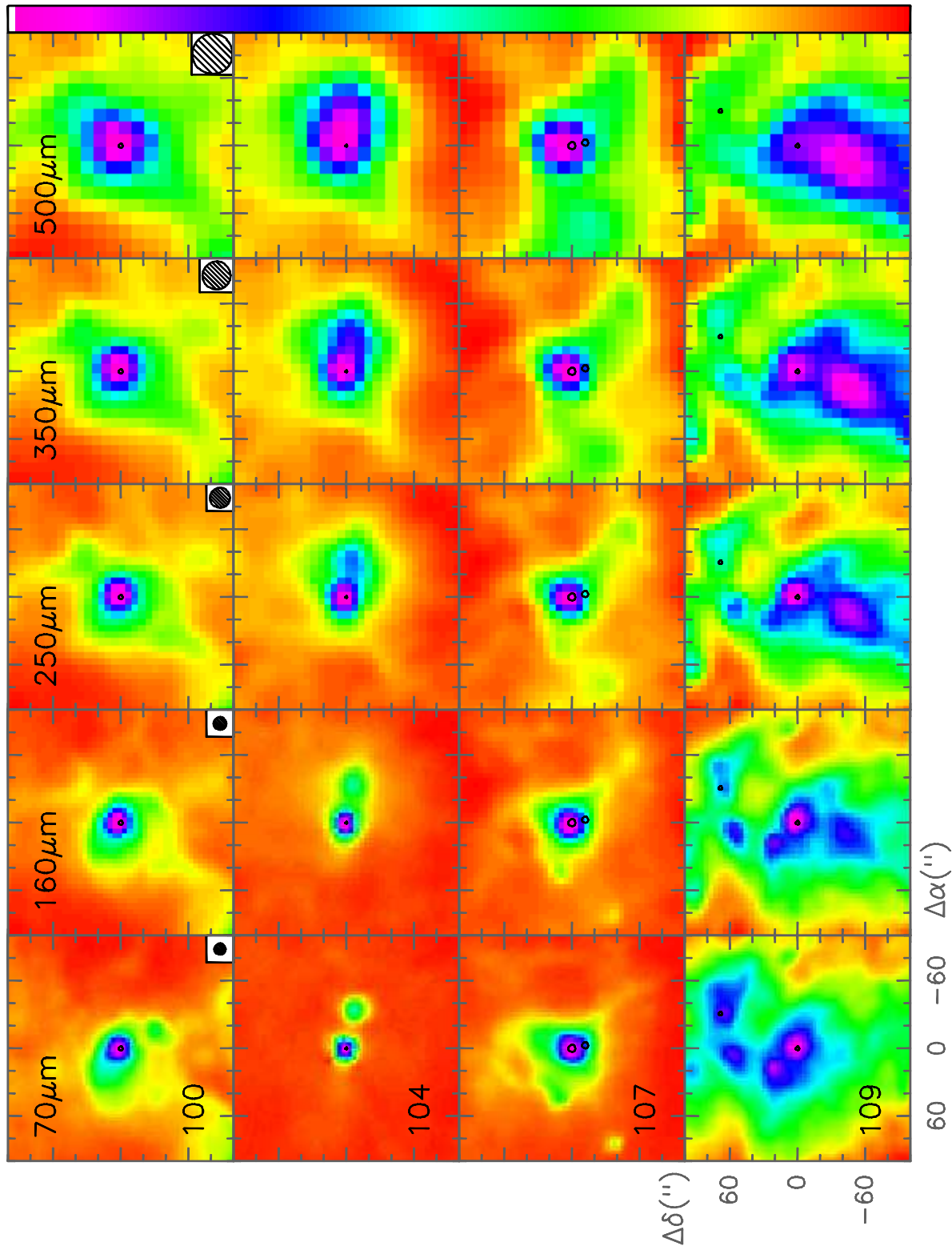


Fig. A.4. continued

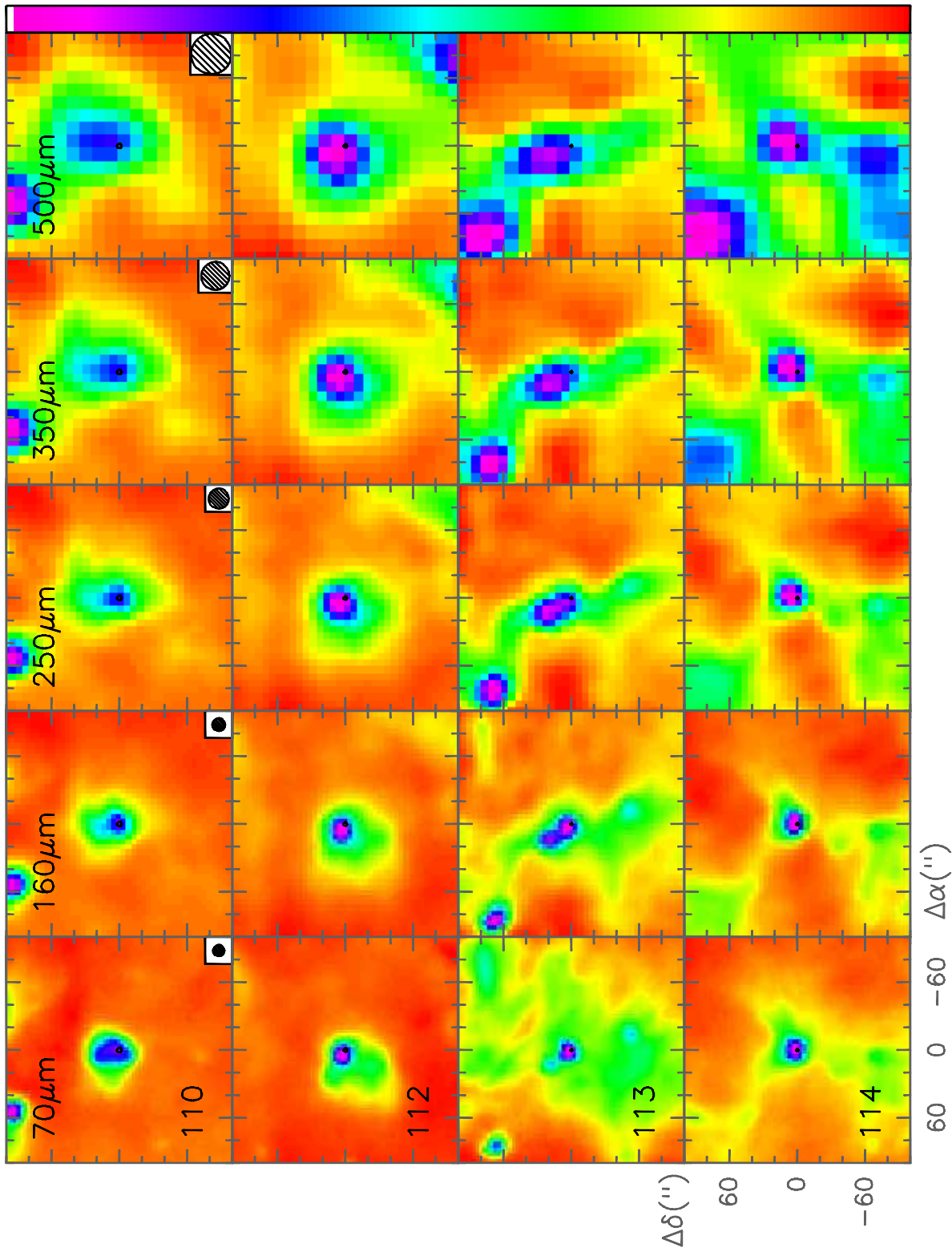


Fig. A.4. continued

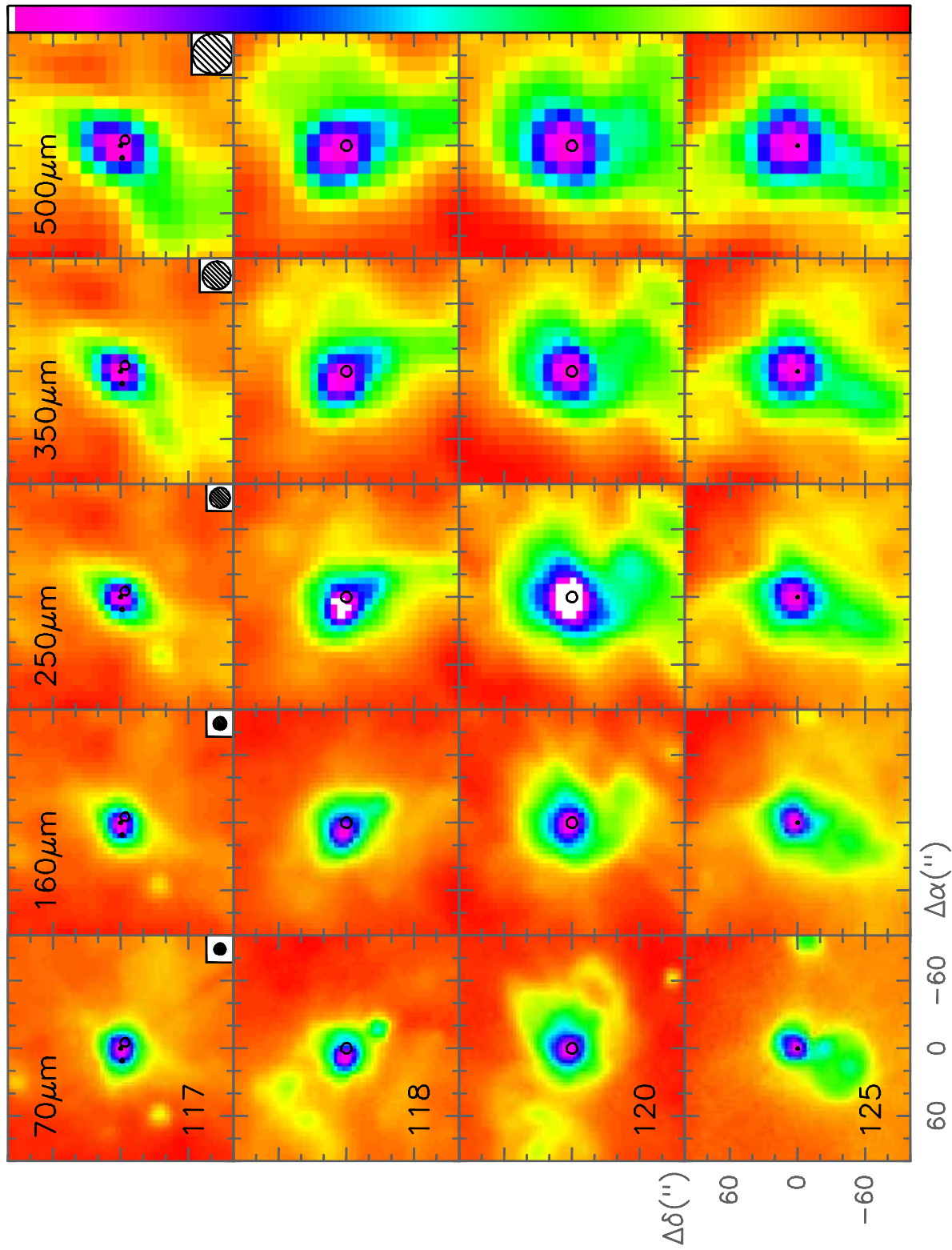


Fig. A.4. continued

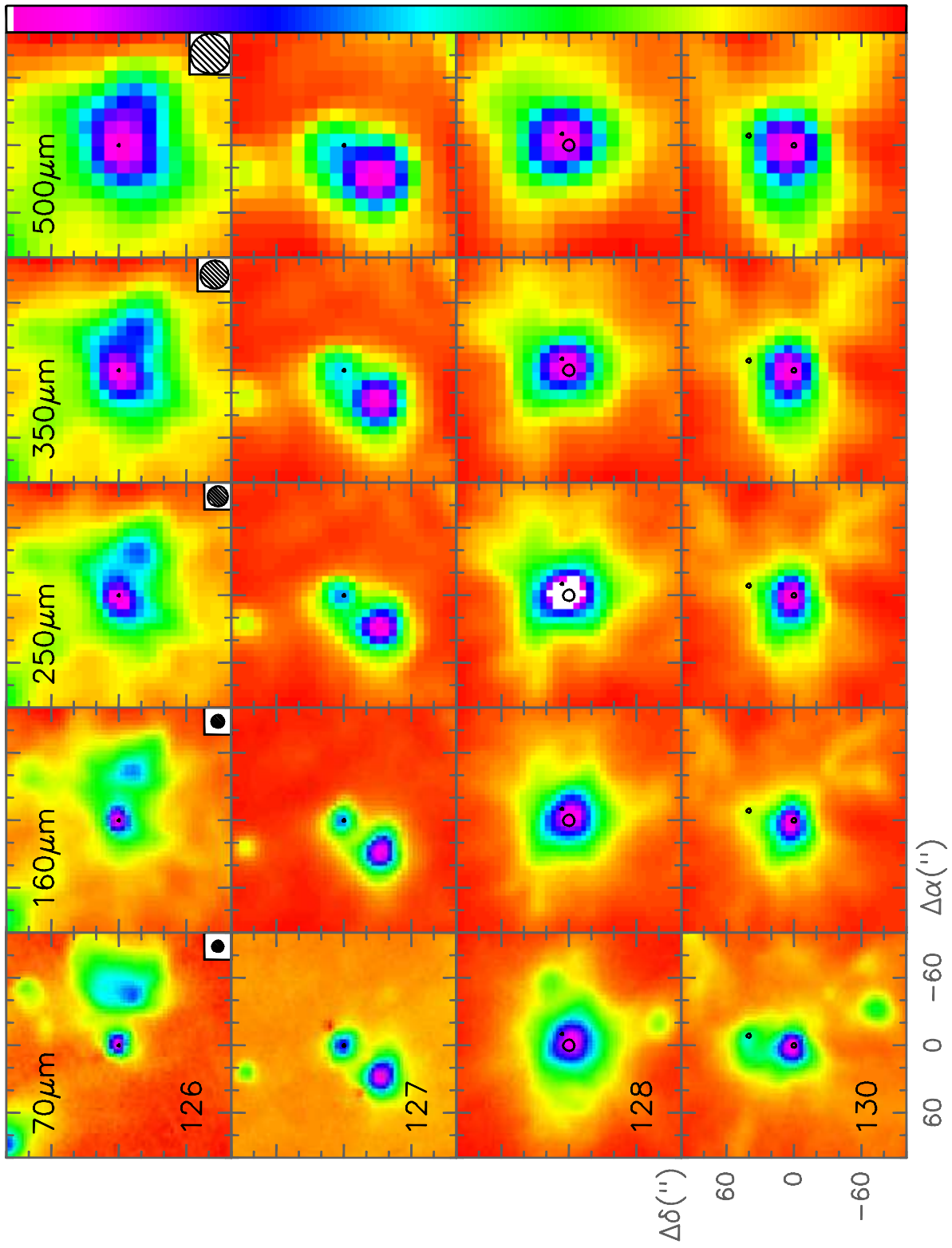


Fig. A.4. continued

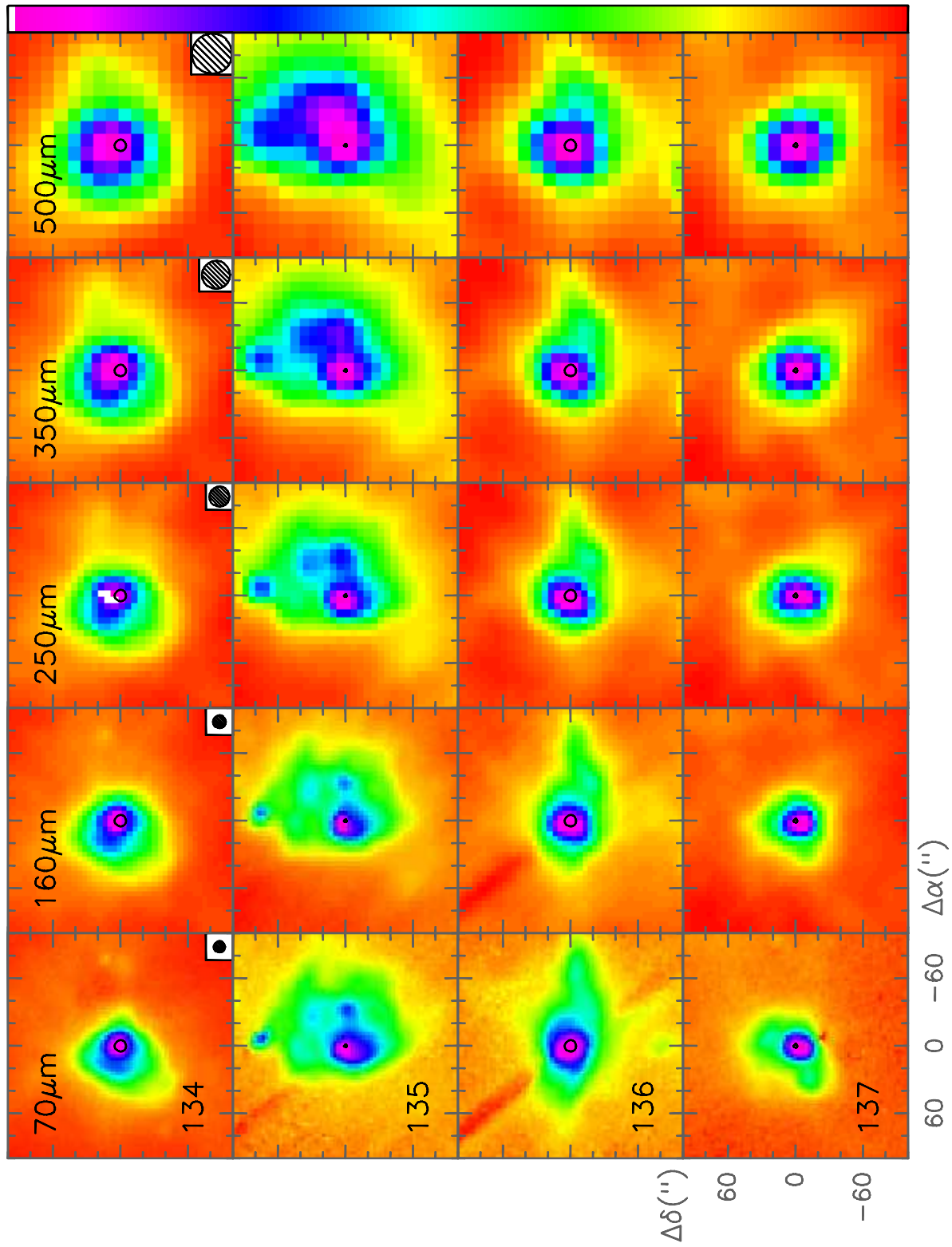


Fig. A.4. continued

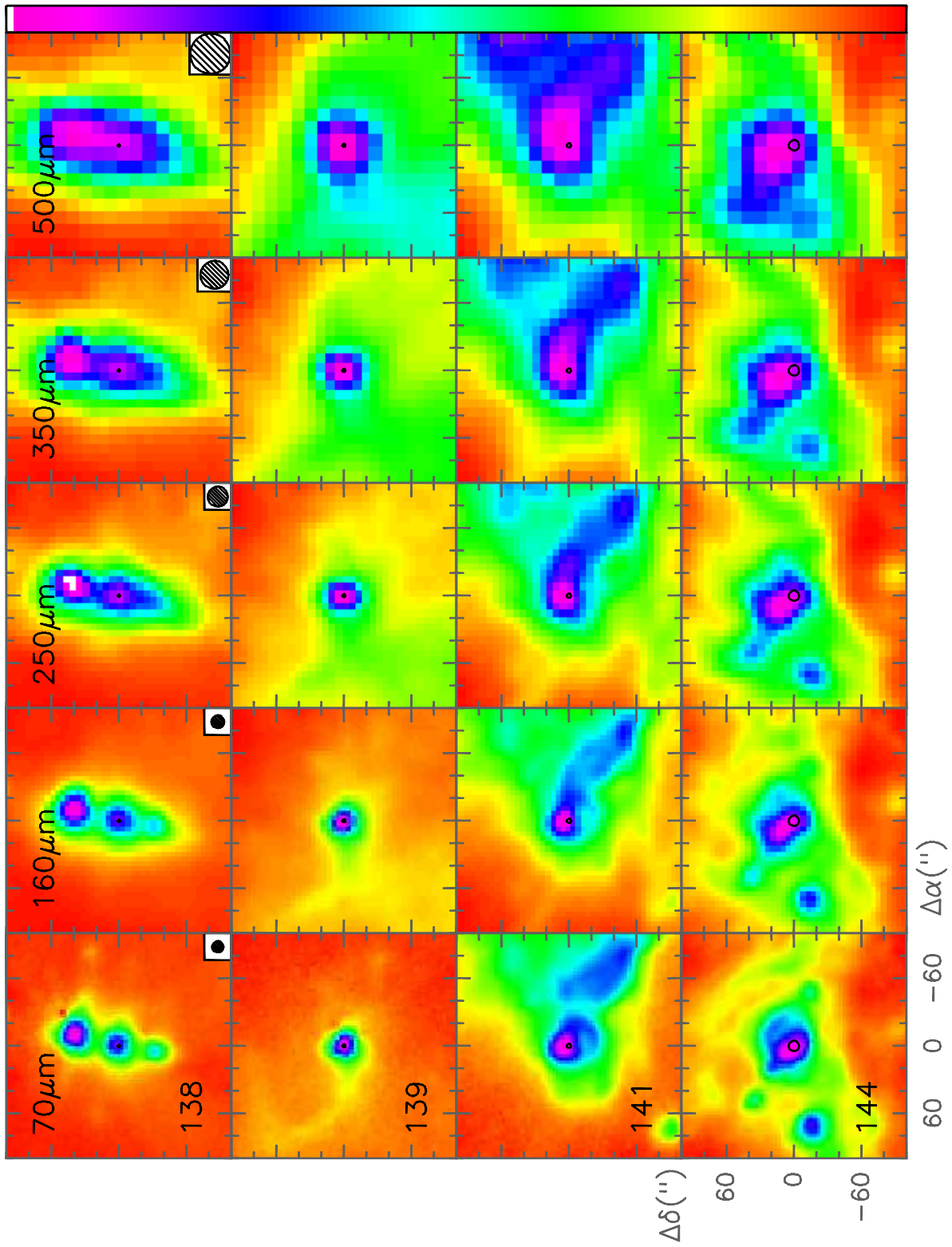


Fig. A.4. continued

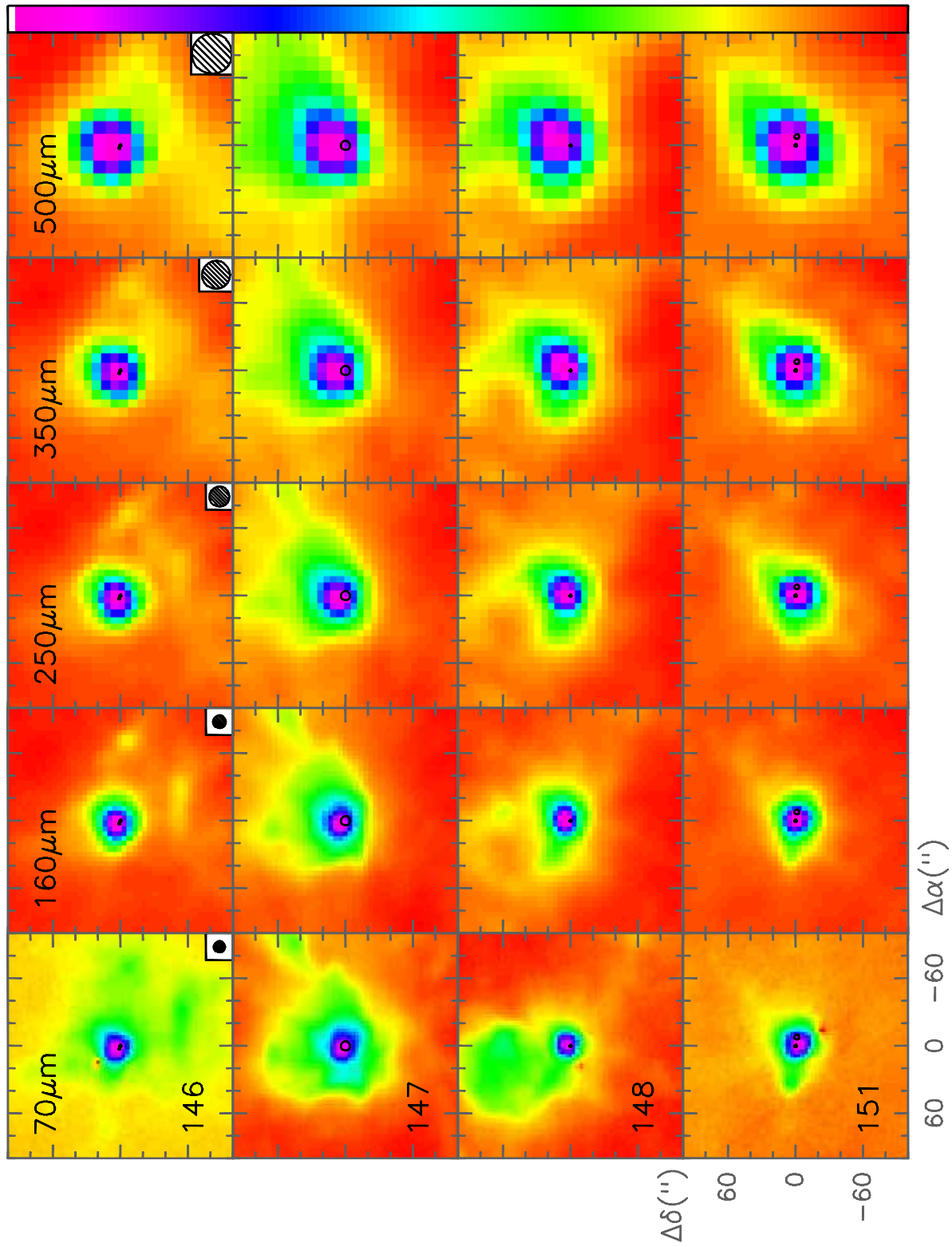


Fig. A.4. continued

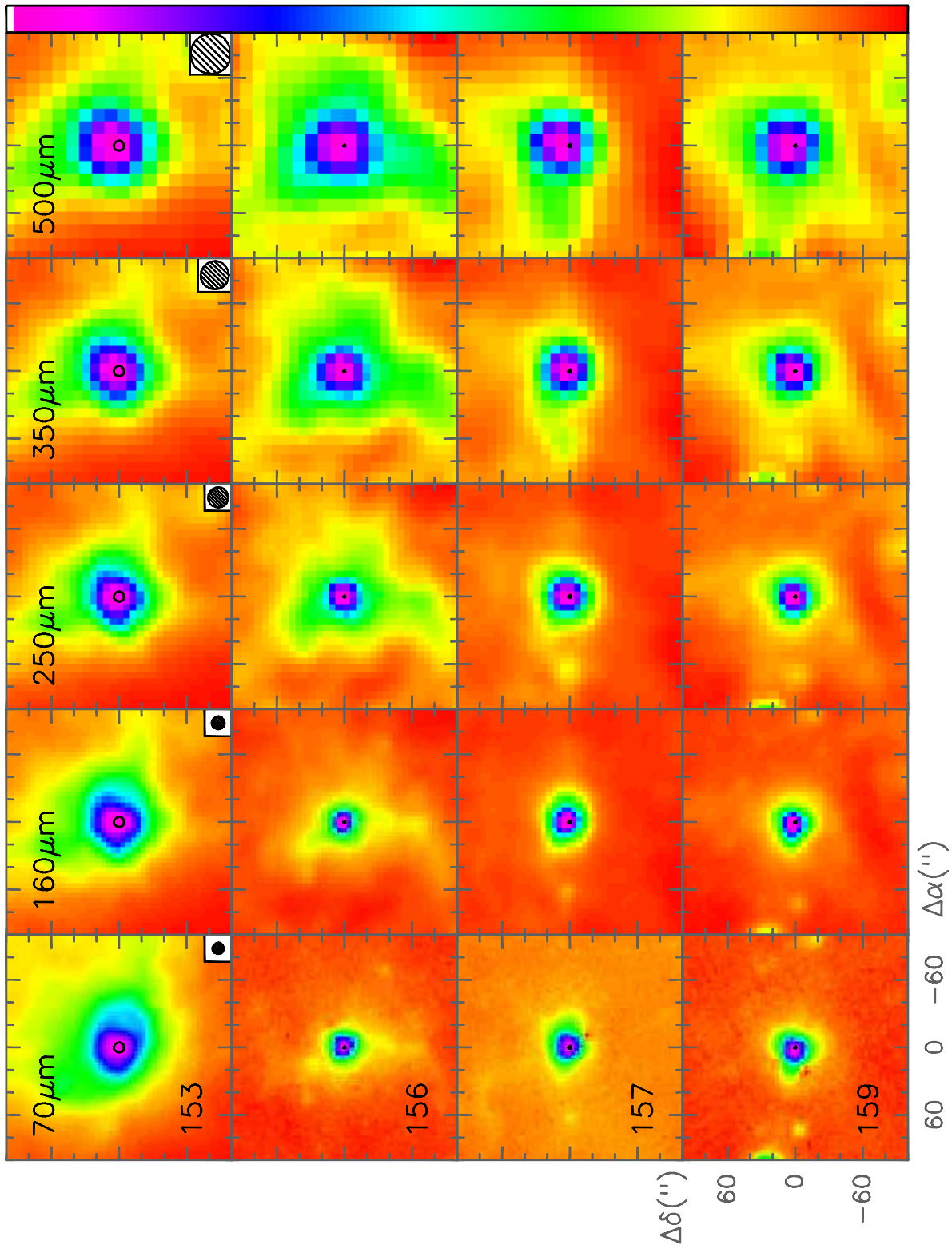


Fig. A.4. continued

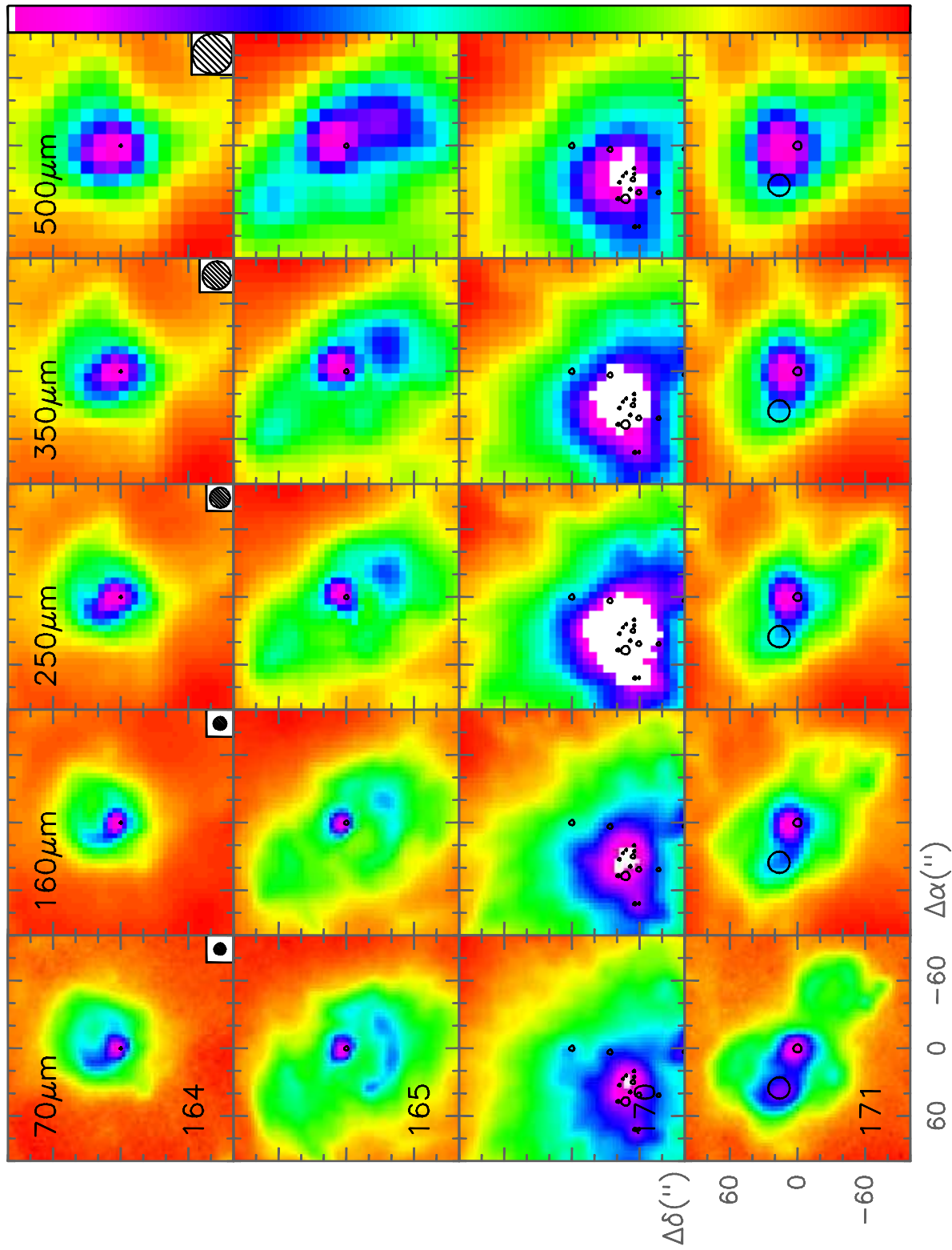


Fig. A.4. continued

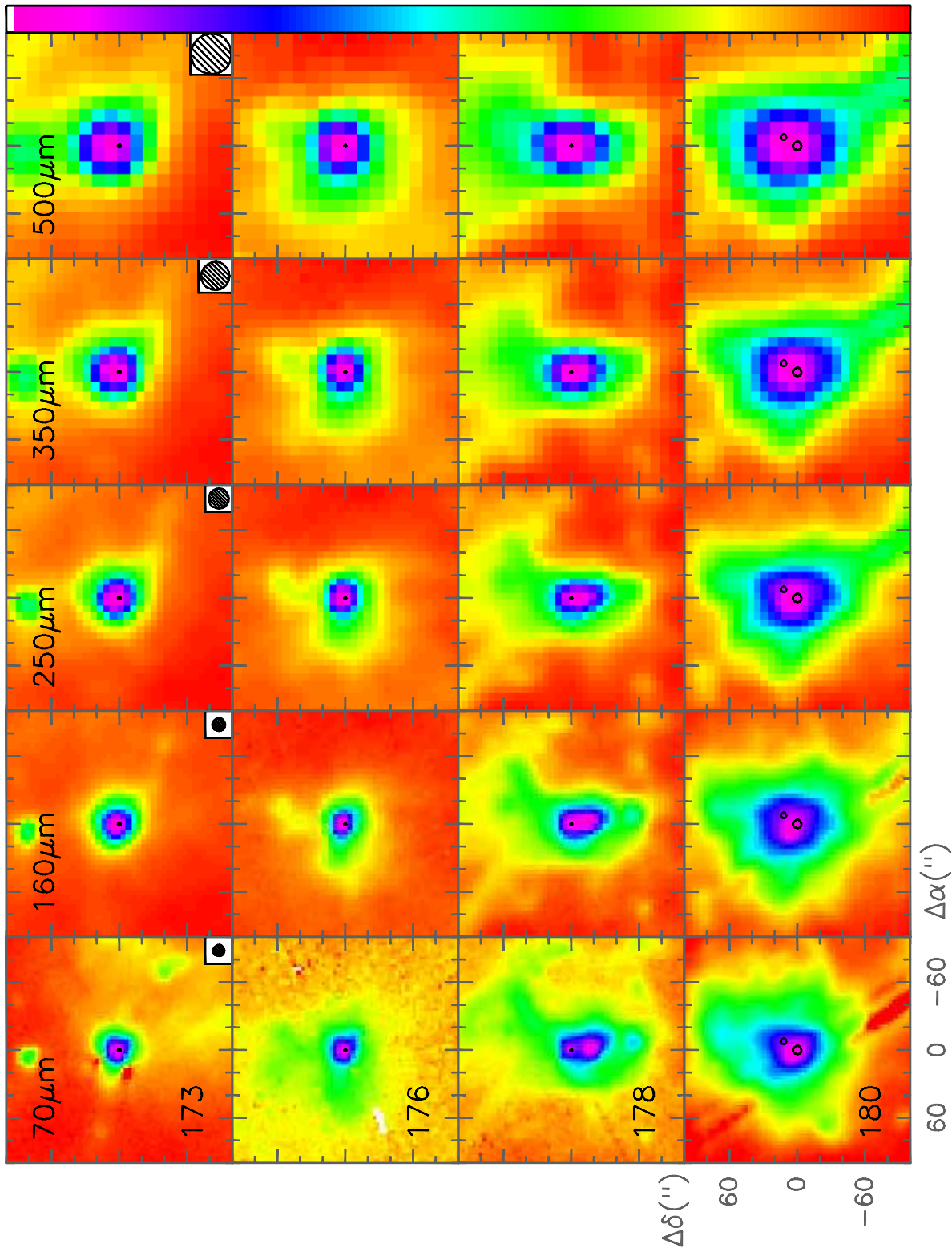


Fig. A.4. continued

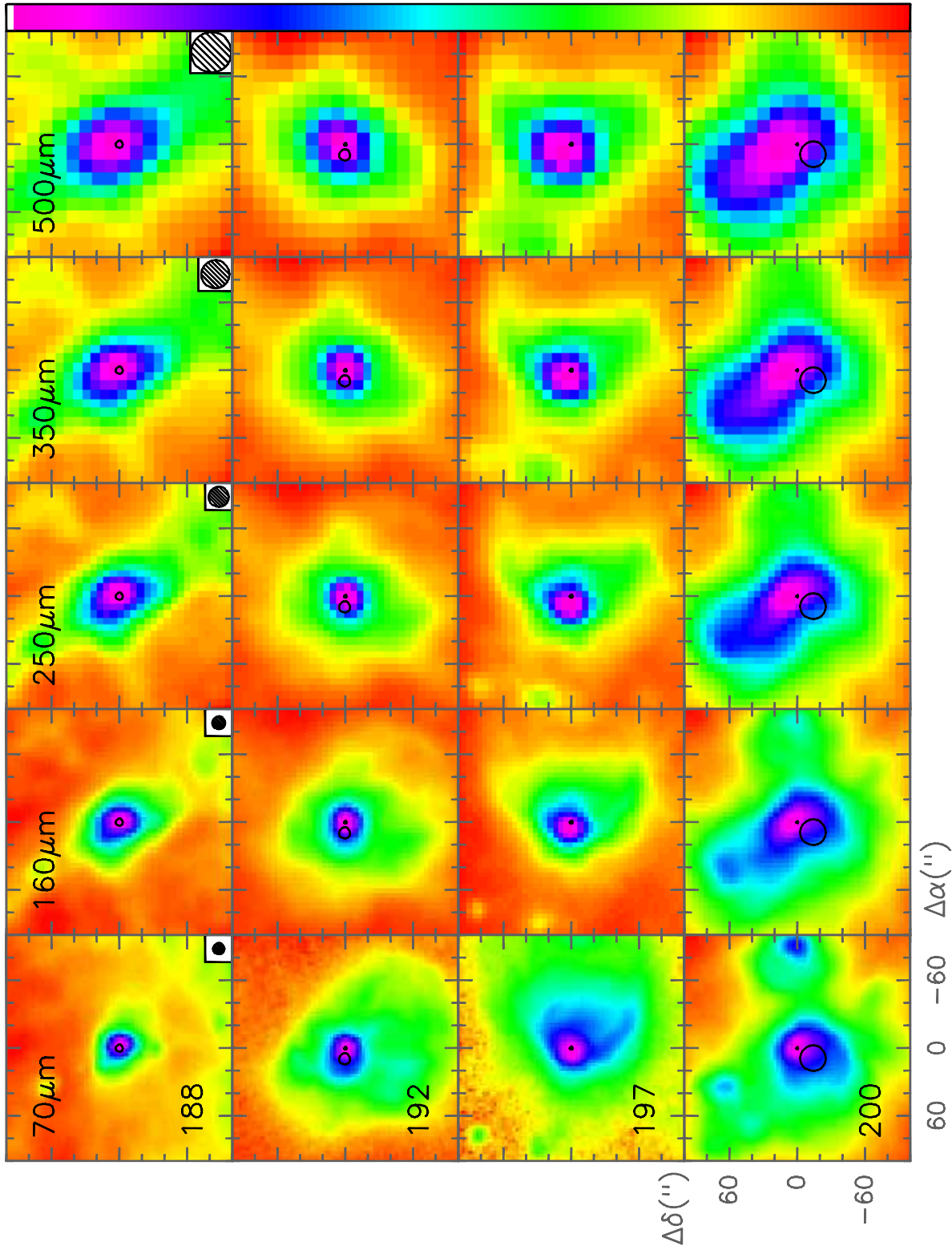


Fig. A.4. continued

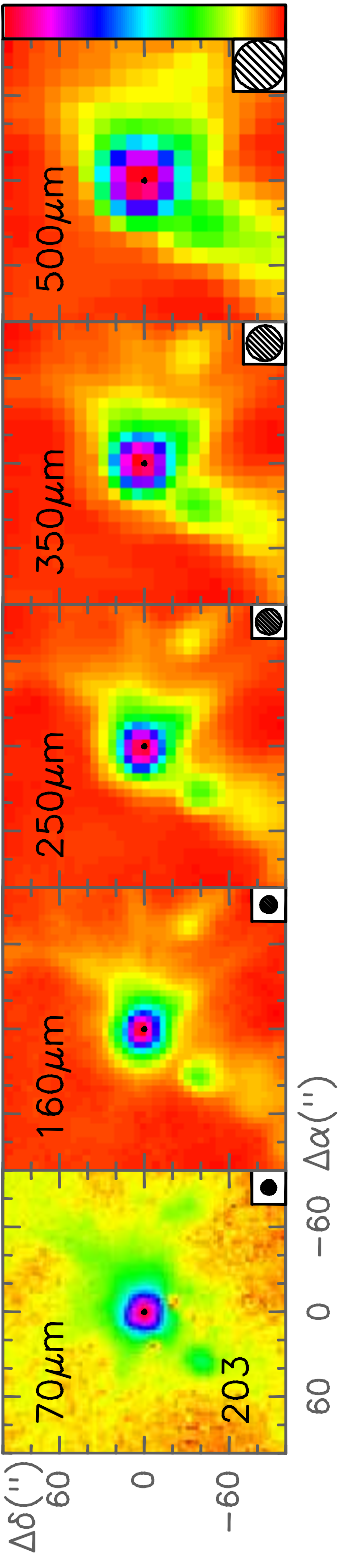


Fig. A.4. continued

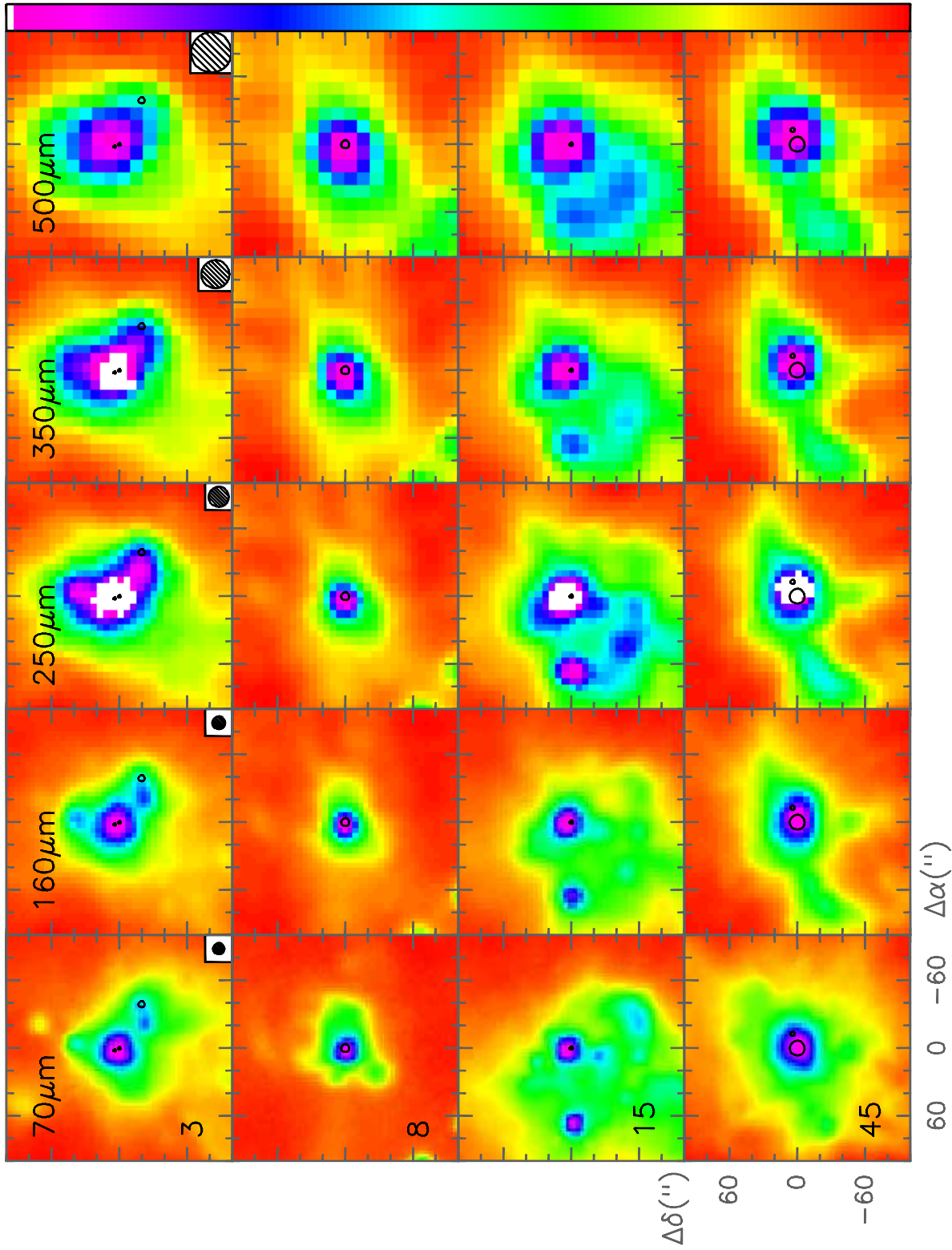


Fig. A.5. Same as Fig. A.2 for the sources lying below the cluster region in Fig. 5.

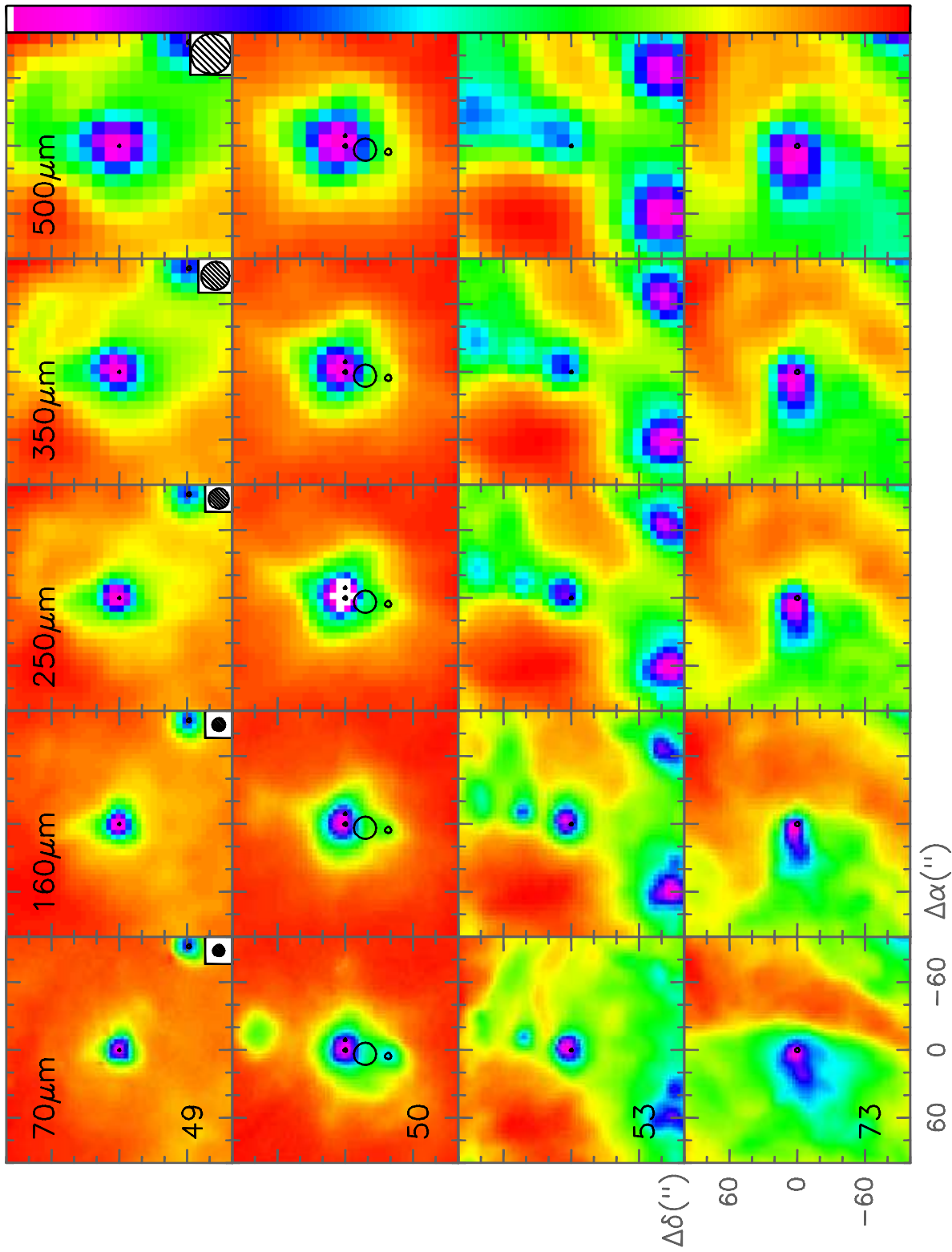


Fig. A.5. continued

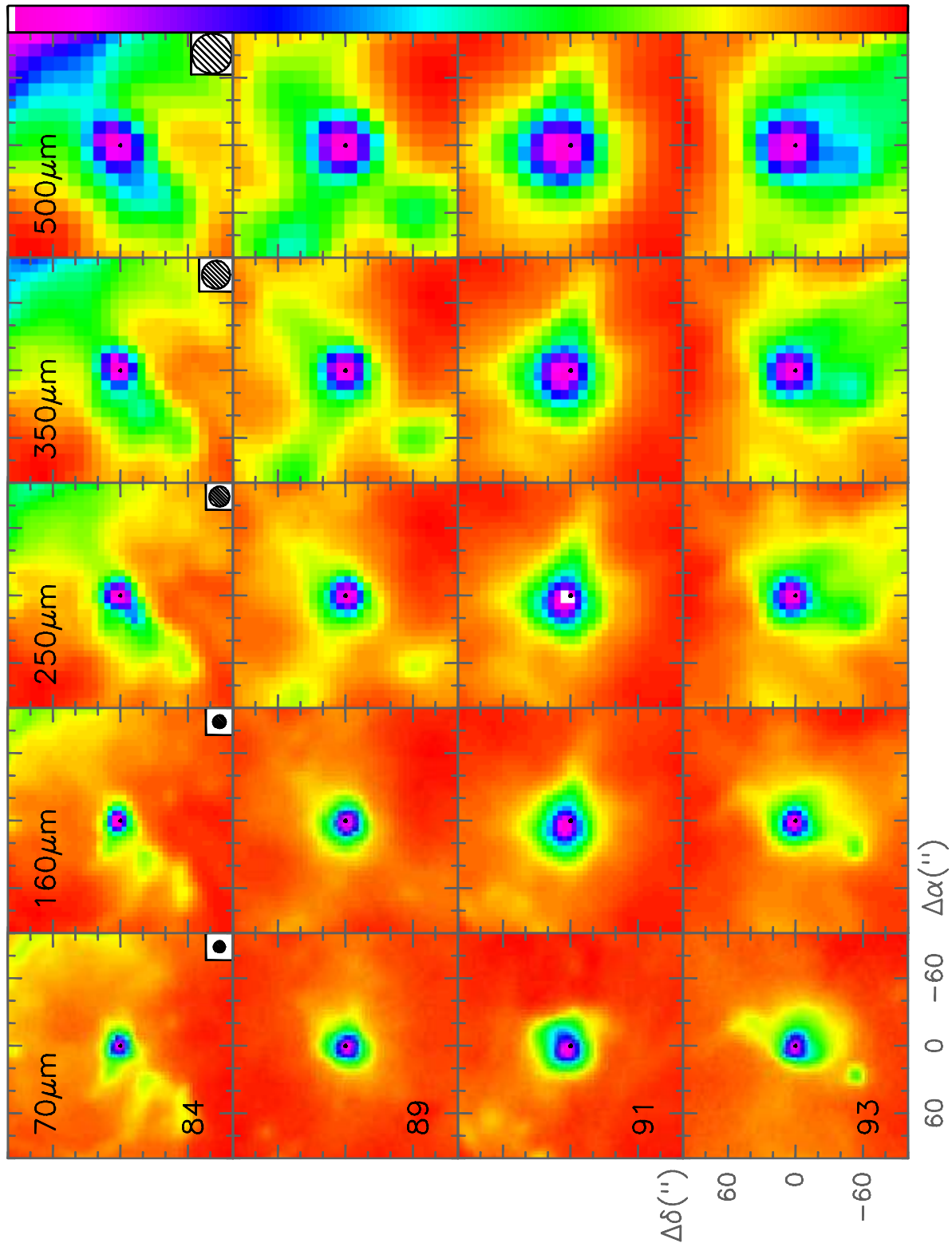


Fig. A.5. continued

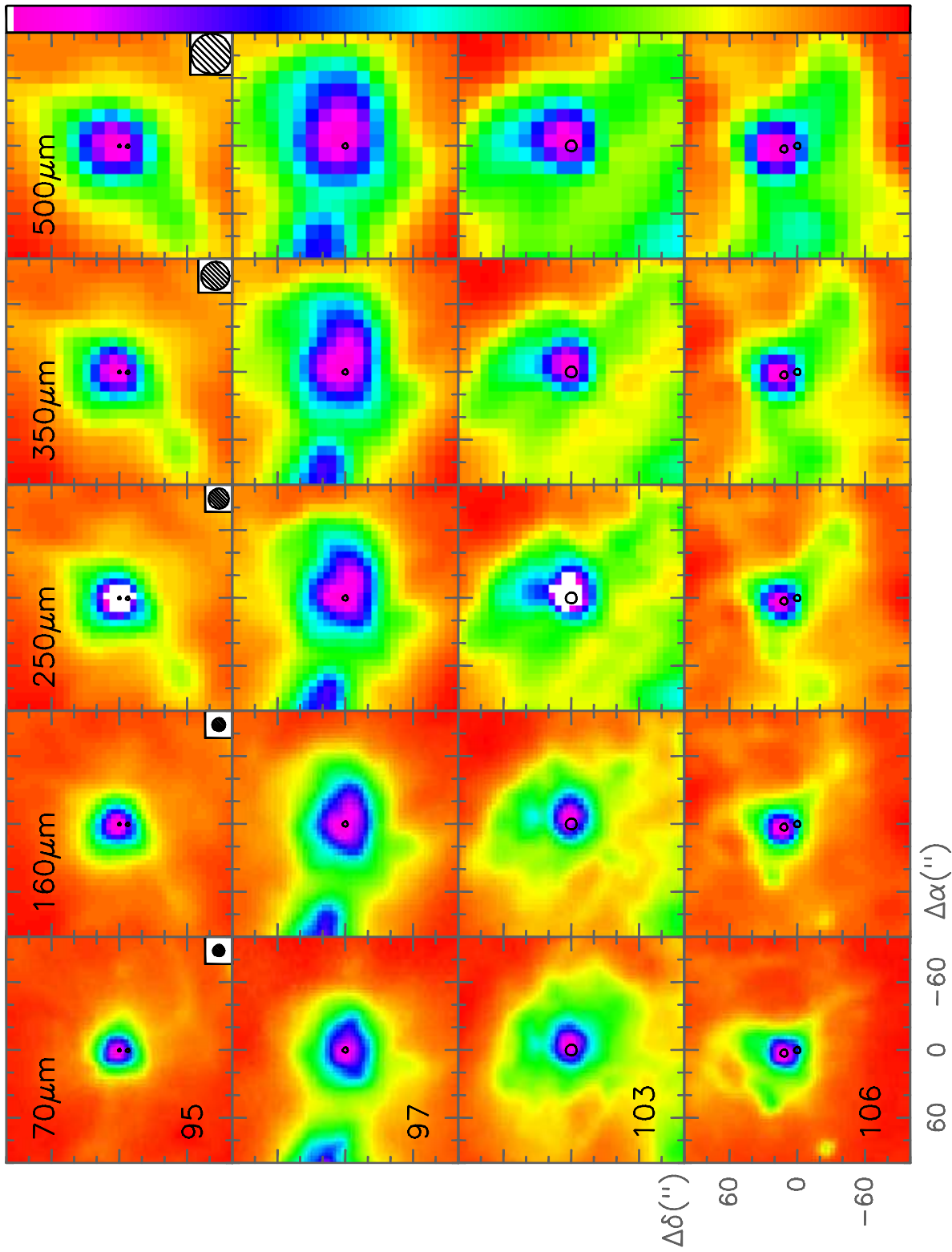


Fig. A.5. continued

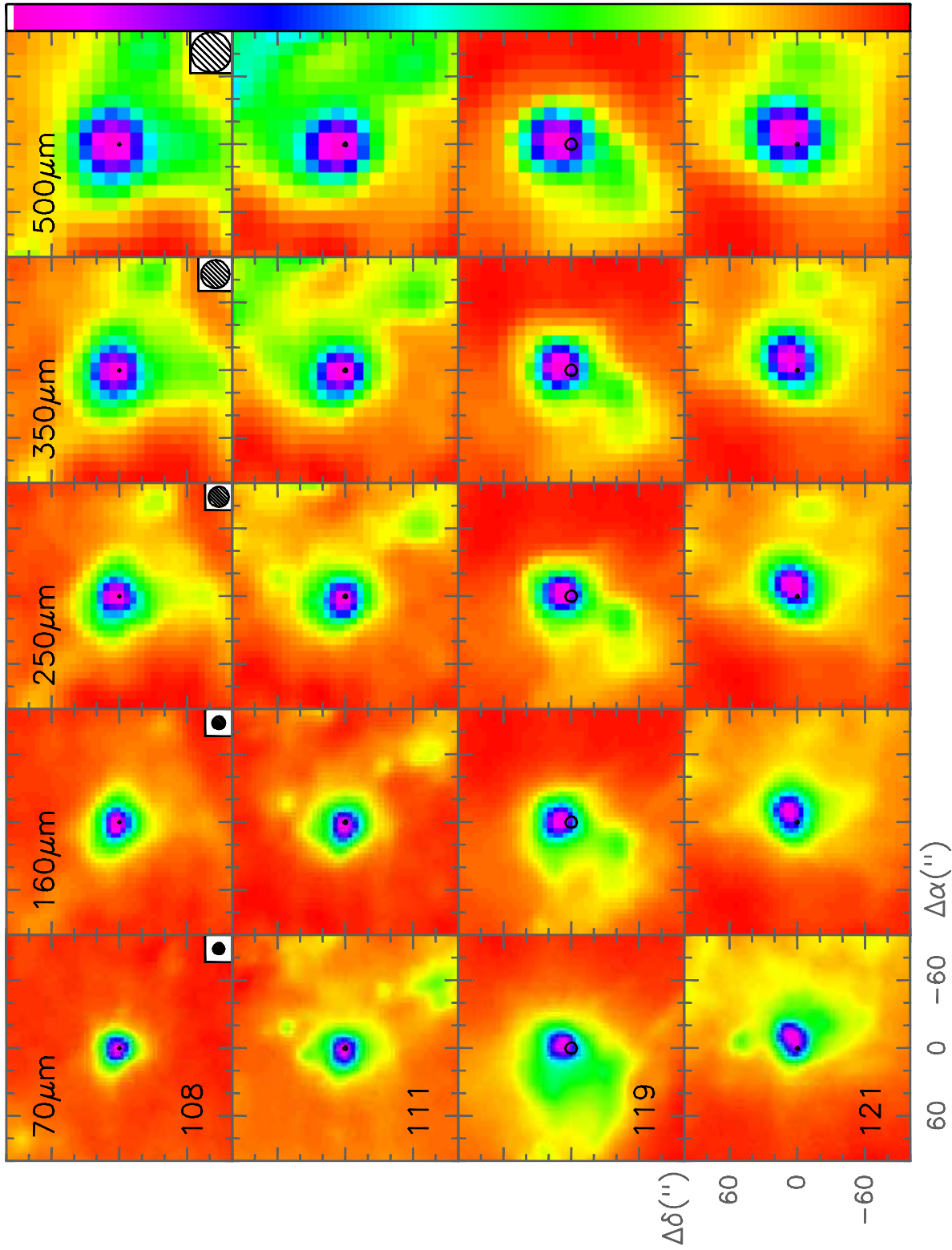


Fig. A.5. continued

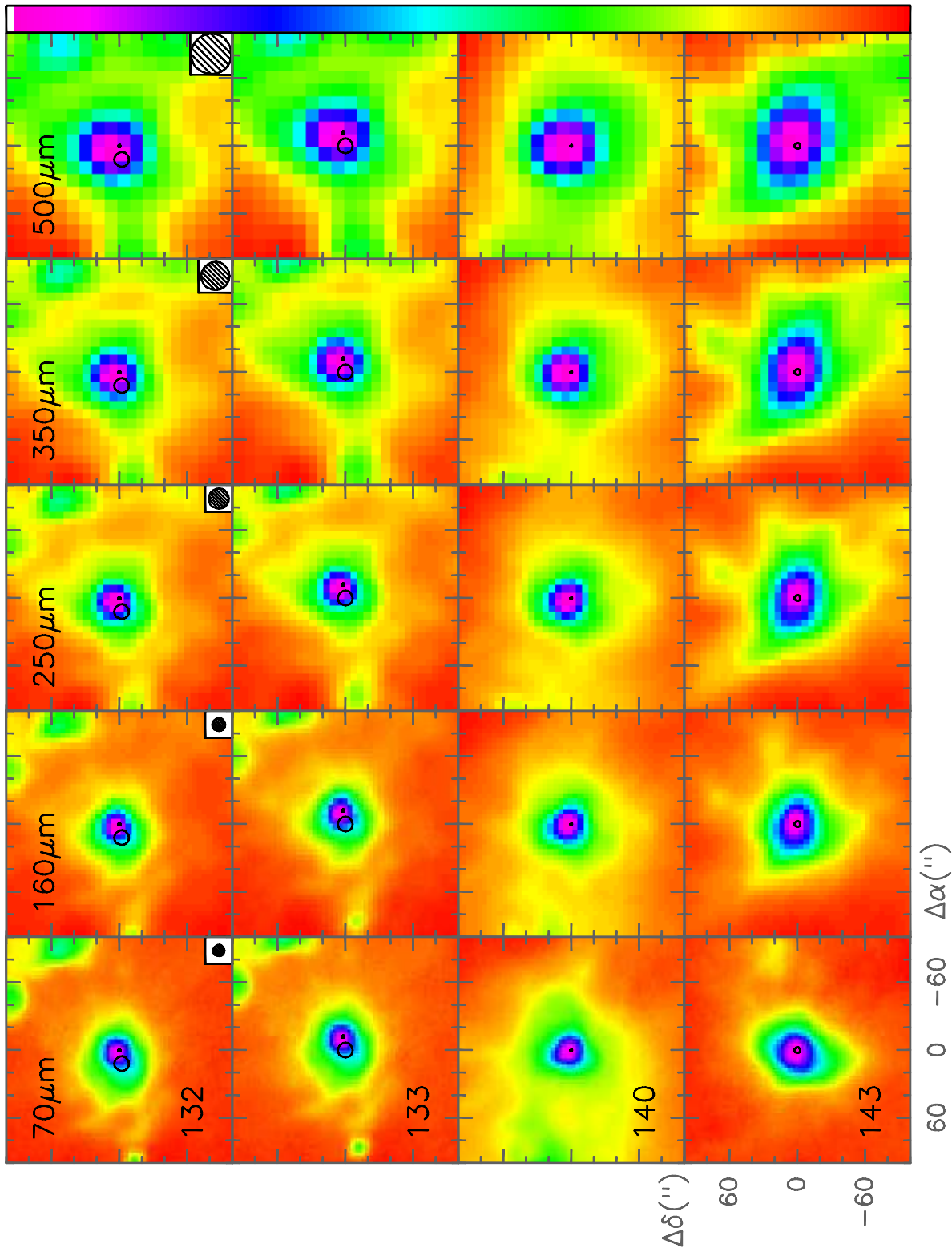


Fig. A.5. continued

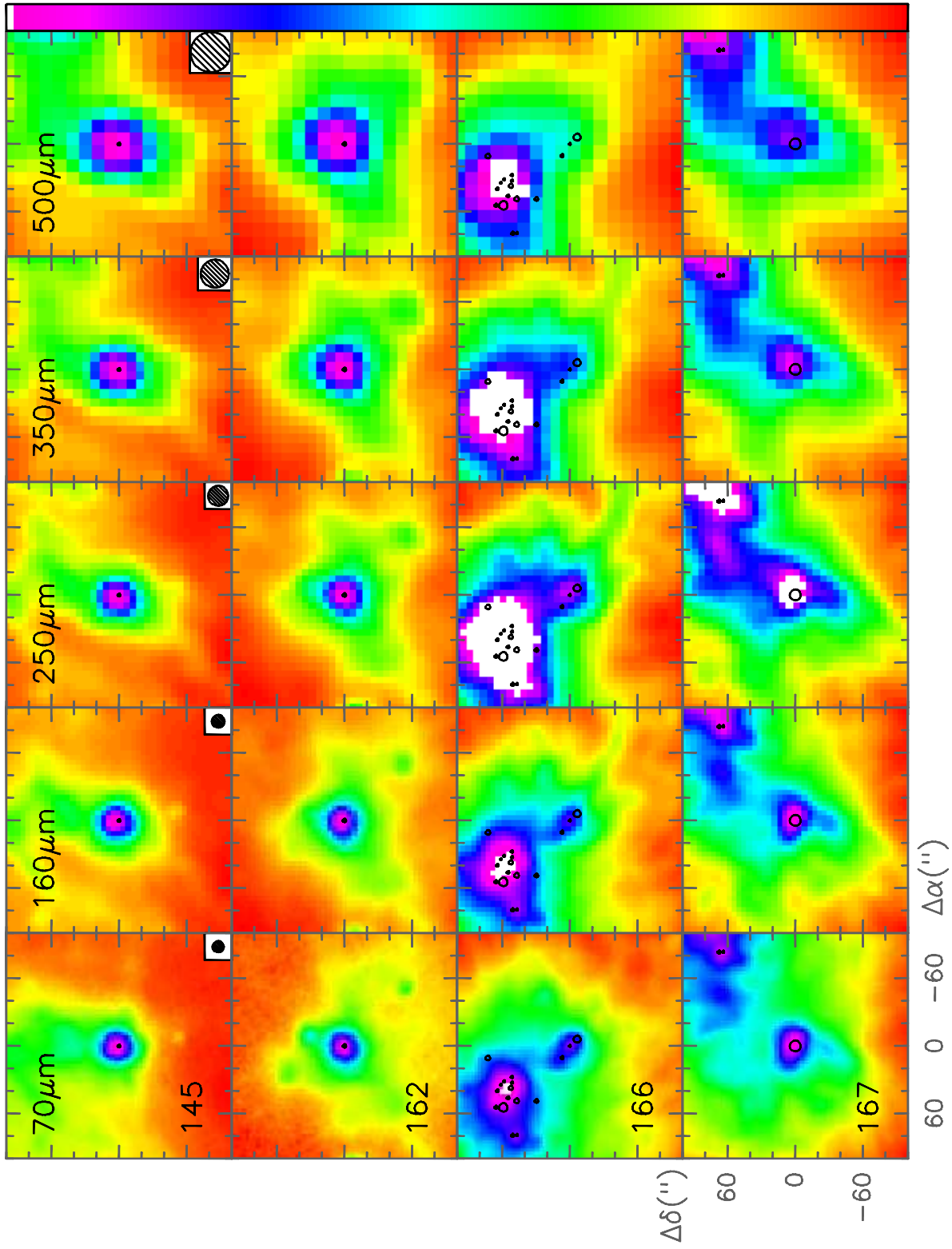


Fig. A.5. continued

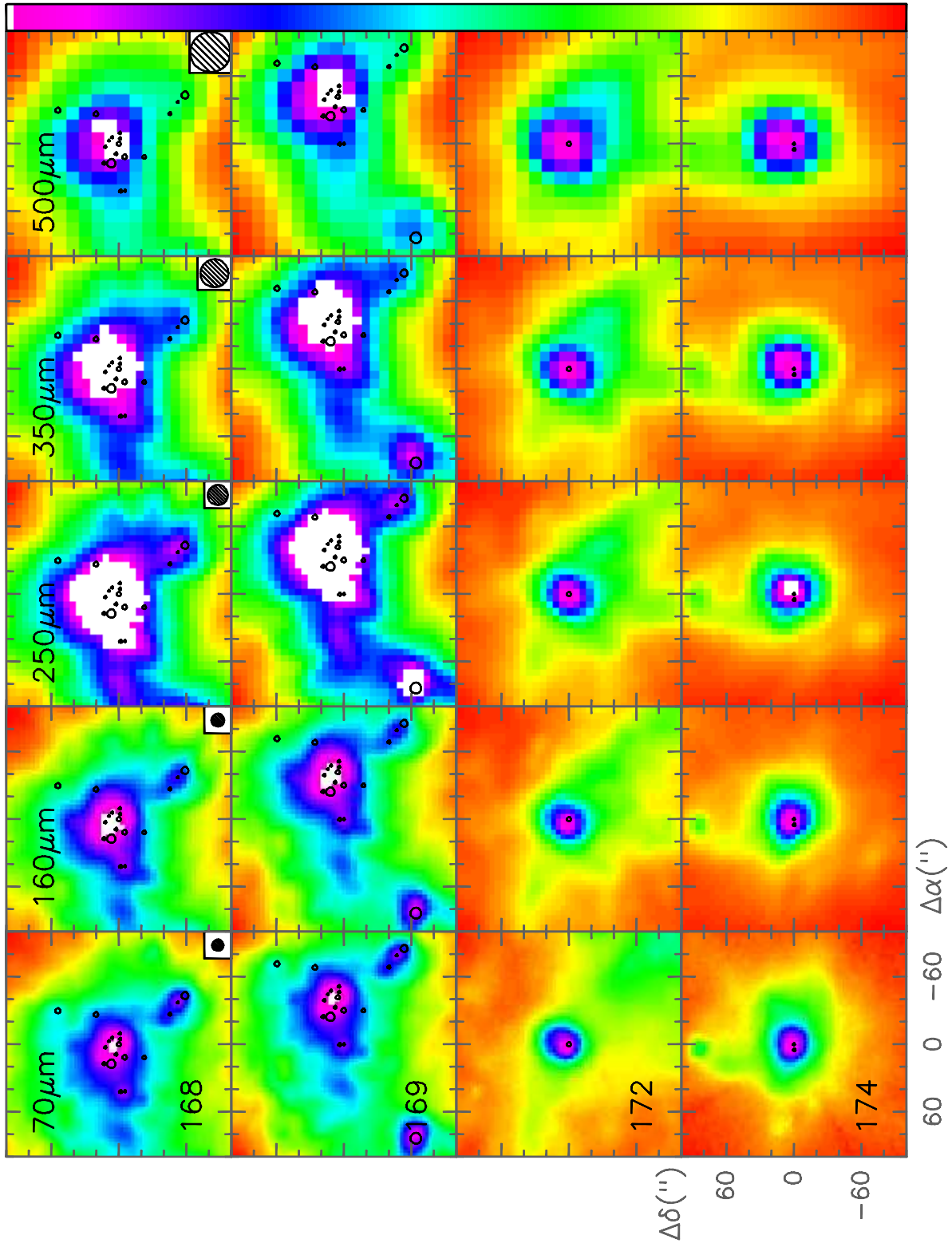


Fig. A.5. continued

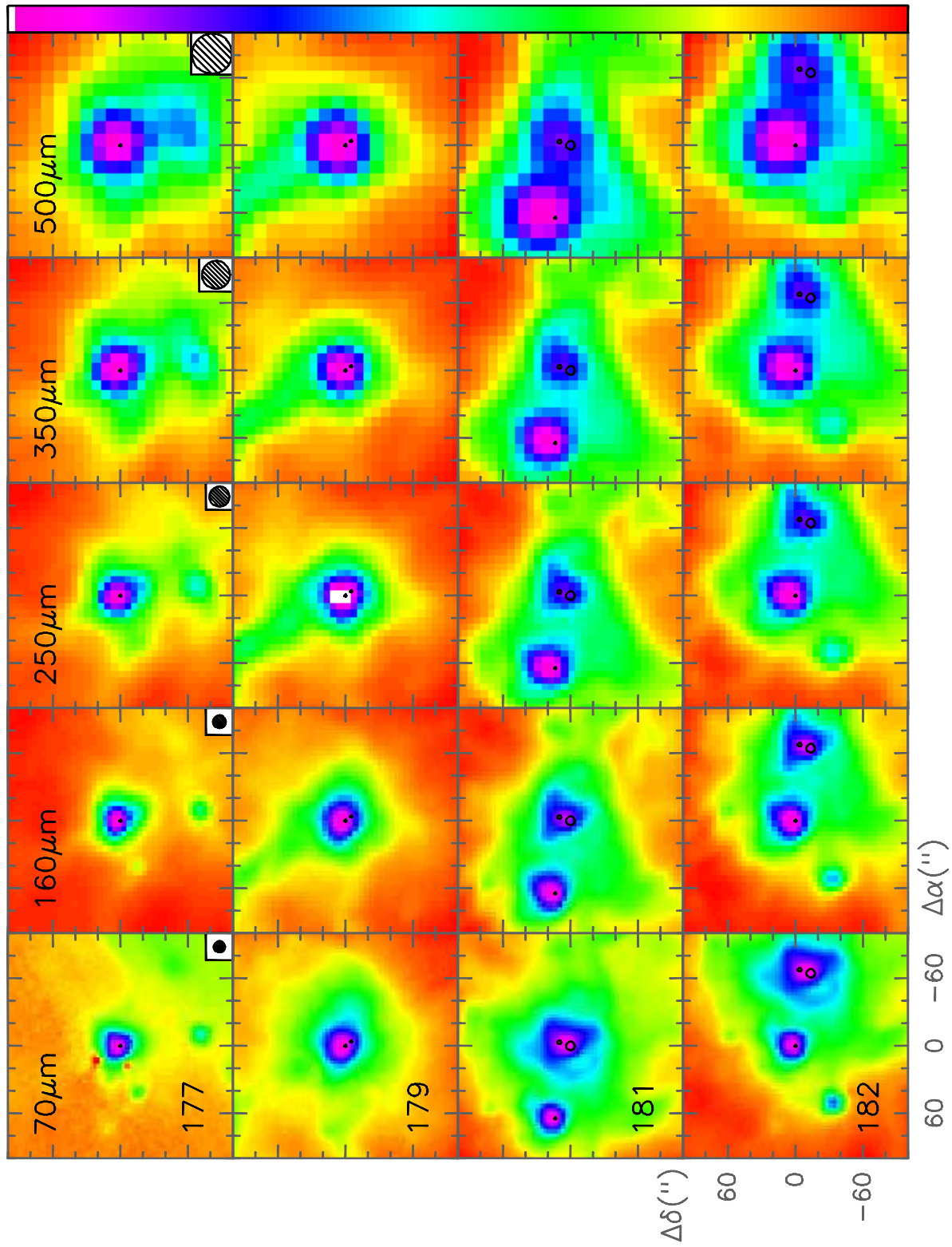


Fig. A.5. continued

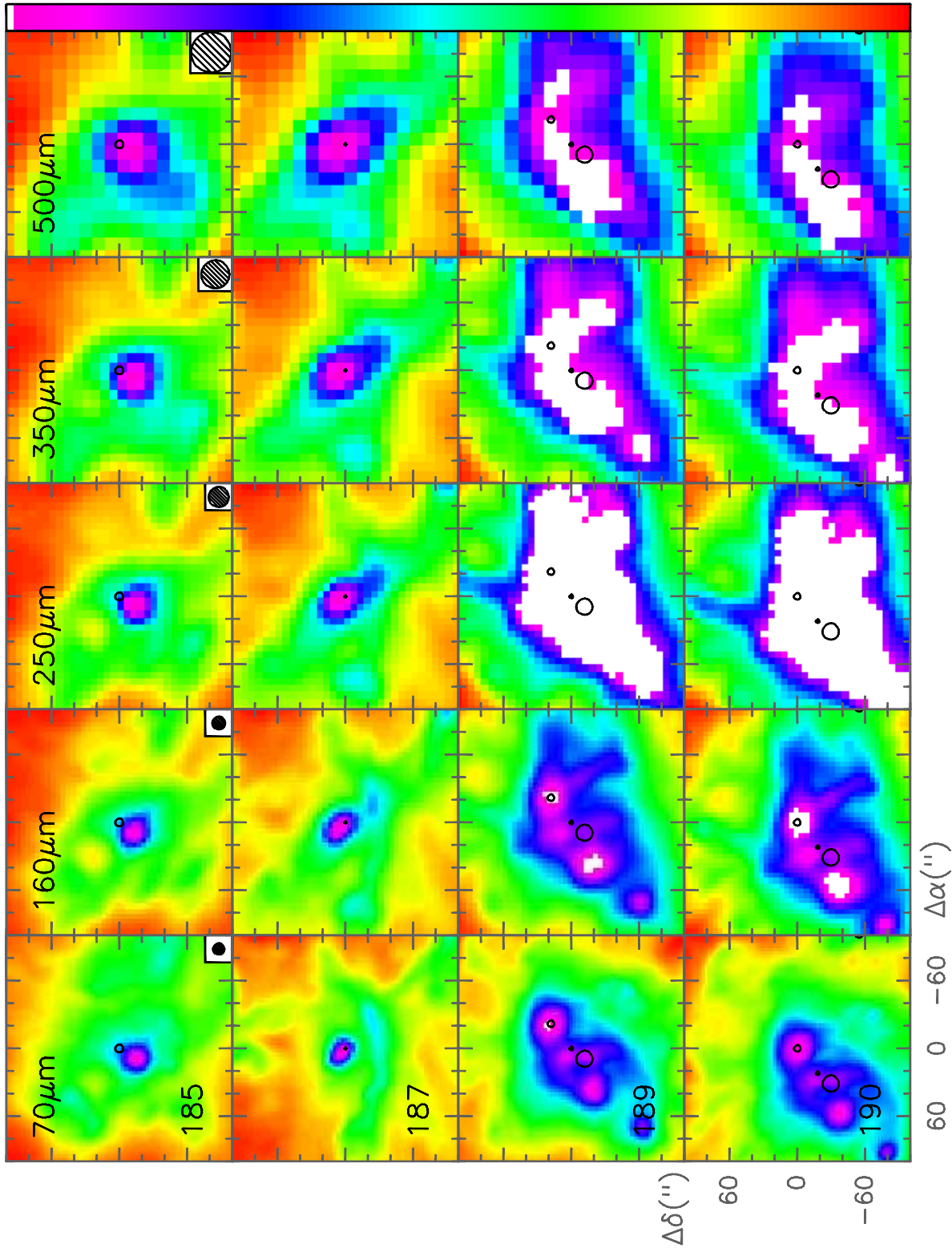


Fig. A.5. continued

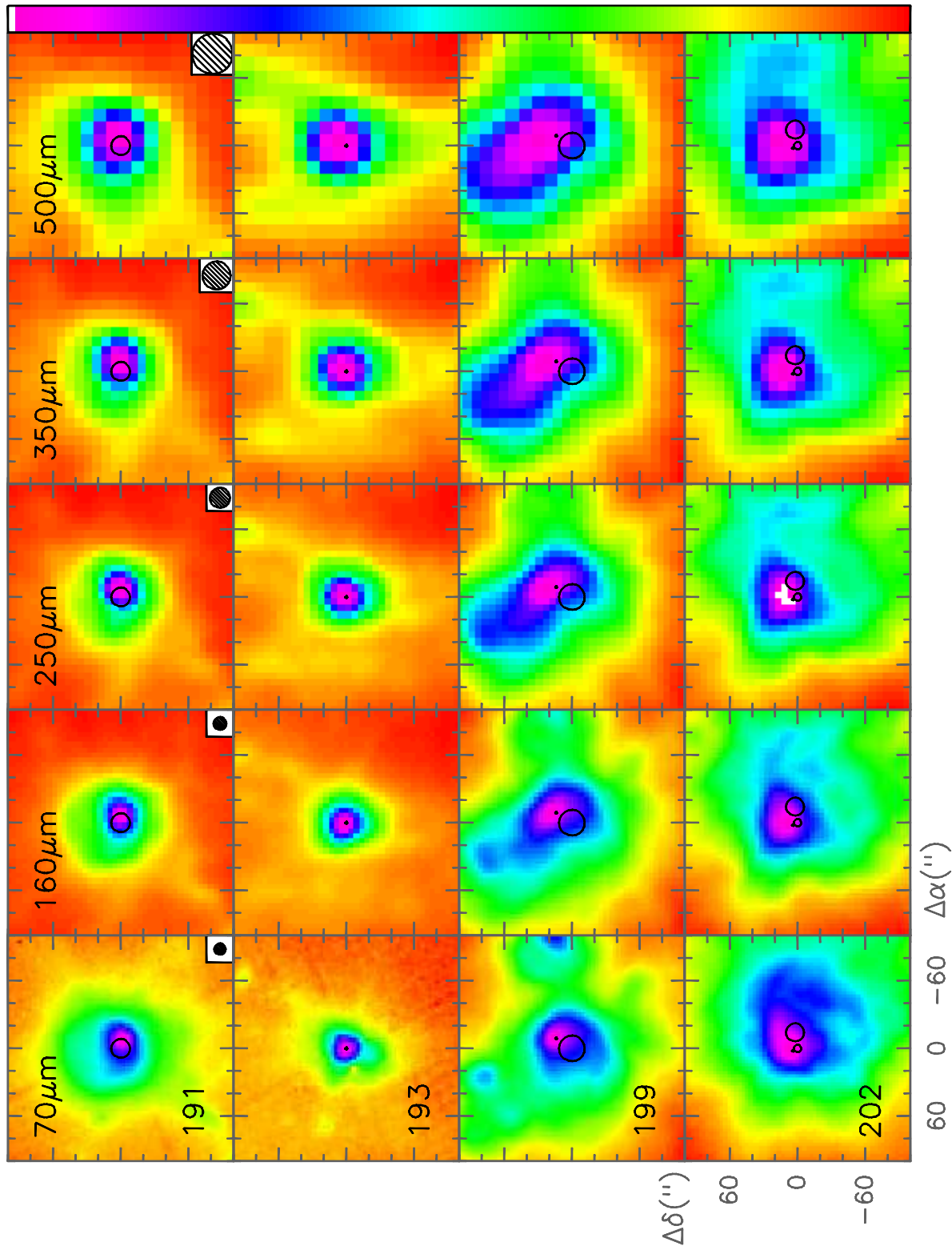


Fig. A.5. continued

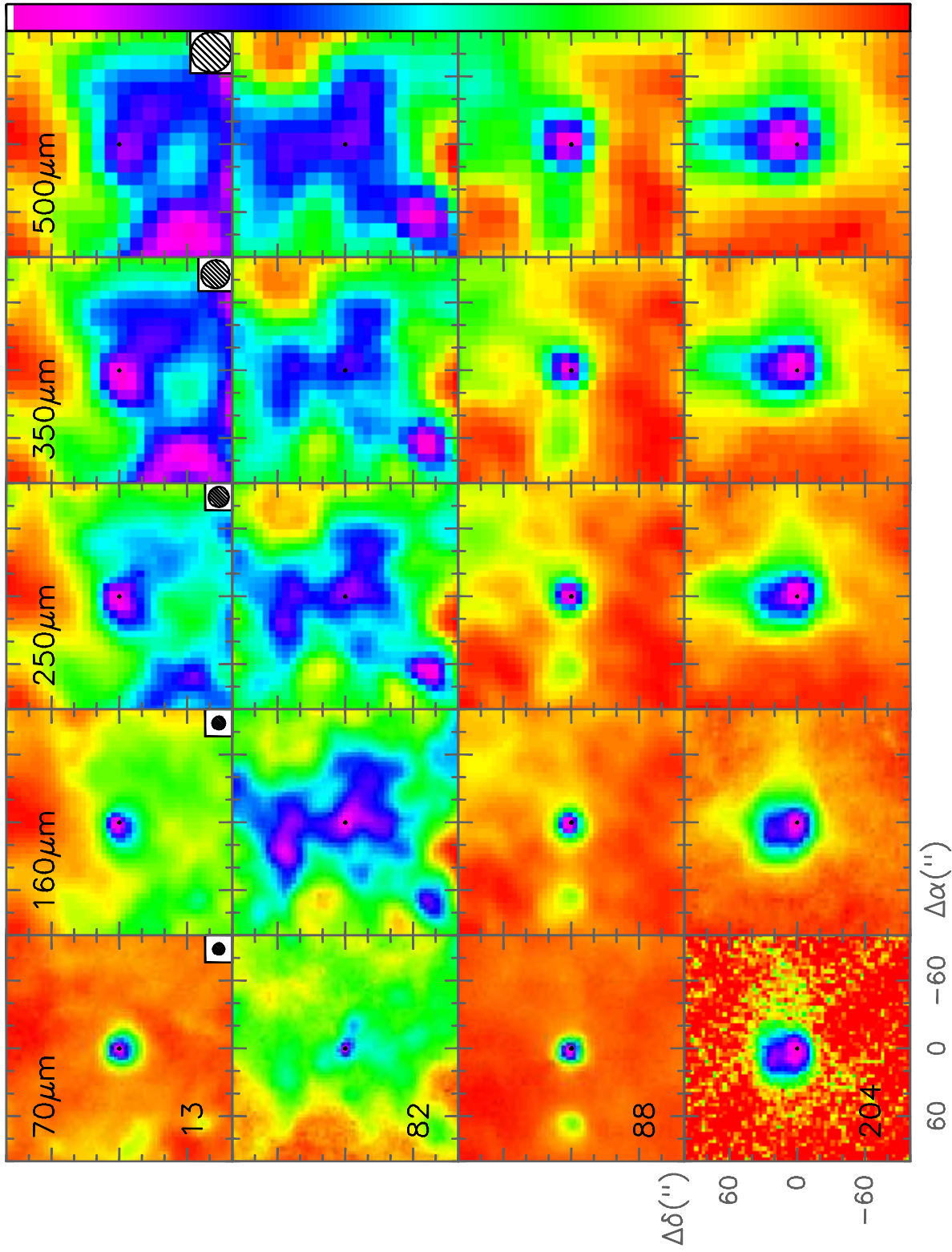


Fig. A.6. Same as Fig. A.2 for the sources without distance estimates.